



universität
wien

MASTERARBEIT

Titel der Masterarbeit

„Ab initio calculations for ice: DFT and RPA“

Verfasser

Markus Macher BSc

angestrebter akademischer Grad

Master of Science (MSc)

Wien, 2013

Studienkennzahl lt. Studienblatt:

A 066 876

Studienrichtung lt. Studienblatt:

Physik

Betreuerin / Betreuer:

Univ.-Prof. Dipl.Ing. Dr. Georg Kresse

Contents

List of Figures

List of Tables

1	Introduction	1
2	Properties of water and ice	3
2.1	The H ₂ O molecule	3
2.2	The water phase diagram	4
2.3	The ice crystal, ice rules	5
2.4	The hydrogen bond	7
2.5	The van der Waals interaction	9
3	Computational quantum mechanics	11
3.1	Introduction, approximations	11
3.1.1	The Born-Oppenheimer approximation	12
3.1.2	Independent particle approximation	12
3.2	Hartree-Fock theory	13
3.3	Density functional theory	14
3.3.1	Hohenberg-Kohn theorems	15
3.3.2	Kohn-Sham <i>ansatz</i>	15
3.3.3	Kohn-Sham equations	16
3.4	ACFDT in the random phase approximation	18
3.4.1	Adiabatic connection dissipation-fluctuation theorem . . .	18
3.4.2	Random phase approximation	20
4	Vibrational and dynamical properties	21
4.1	Phonons in molecules and solids	21
4.1.1	Dynamic lattice model	21
4.1.2	Normal modes	22
4.1.3	Normal modes of an one-dimensional lattice	22
4.1.4	Normal modes of a three-dimensional lattice	23
4.1.5	Energies and phonons	24
4.2	Lattice dynamics and forces	25
4.3	Density functional perturbation theory	26
4.3.1	Perturbation theory	26
4.3.2	Perturbation of the Kohn-Sham potentials	27
4.4	Dynamical charges (Born effective charges)	27

4.5	Infrared spectra	28
5	Computational setup	29
5.1	Relaxation and volume scan	29
5.2	RPA setup	30
5.3	Infrared spectra	31
6	PBE and RPA results	33
6.1	Phases investigated	33
6.2	Ice crystal energy convergence	36
6.3	H ₂ O molecule energy convergence	36
6.4	Ice I _h	38
6.5	Ice XI Cmc2 ₁	41
6.6	Ice XI Pna2 ₁	44
6.7	Ice I _c	46
6.8	Ice IX	53
6.9	Ice II	56
6.10	Ice XIII	59
6.11	Ice XV	61
6.12	Ice VIII	63
6.13	Ice X	66
6.14	Total energy and equilibrium volume	70
7	Infrared intensities	75
8	Summary and conclusions	83
	Bibliography	85
	Abstract	97
	Zusammenfassung	99
	Acknowledgements	101
	Curriculum vitae	103

List of Figures

2.1	The tetrahedral structure of the H ₂ O molecule.	4
2.2	The electron density contour map in the molecular y-z plane with densities in atomic units.	5
2.3	Phase diagram of water.	6
2.4	Tetrahedral arrangement of oxygen atoms.	7
2.5	Hydrogen bonding.	8
2.6	Average hydrogen bond in liquid water, H-O-H angle and distance.	8
2.7	Average hydrogen bond in liquid water, O-H-O angles and distances.	9
3.1	Schematic representation of the Kohn-Sham <i>ansatz</i>	17
4.1	Acoustic and optical branch in an one-dimensional lattice.	23
4.2	Acoustic and optical vibrations in a linear diatomic chain.	23
4.3	Acoustic and optical branches in β -SiC.	25
6.1	Structures investigated.	35
6.2	Example of a k-points extrapolation.	36
6.3	Energy convergence of the H ₂ O molecule.	37
6.4	Ice I _h structure.	38
6.5	Ice I _h - PBE, RPA+EXX and RPA+SCHF energy-volume curves.	39
6.6	Ice XI Cmc2 ₁ structure.	41
6.7	Ice XI Cmc2 ₁ - PBE, RPA+EXX and RPA+SCHF energy-volume curves.	42
6.8	Ice XI Pna2 ₁ structure.	44
6.9	Ice XI Pna2 ₁ - PBE, RPA+EXX and RPA+SCHF energy-volume curves.	45
6.10	Ice I _c (ord. a) structure.	46
6.11	Ice I _c (ord. b) structure.	46
6.12	Ice I _c (ord. c) structure.	47
6.13	Ice I _c (ord. d) structure.	47
6.14	Ice I _c (ord. a) - PBE, RPA+EXX and RPA+SCHF energy-volume curves.	48
6.15	Ice I _c (ord. b) - PBE, RPA+EXX and RPA+SCHF energy-volume curves.	49
6.16	Ice I _c (ord. c) - PBE, RPA+EXX and RPA+SCHF energy-volume curves.	50
6.17	Ice I _c (ord. d) - PBE, RPA+EXX and RPA+SCHF energy-volume curves.	51

6.18	Ice IX structure.	53
6.19	Ice IX - PBE, RPA+EXX and RPA+SCHF energy-volume curves.	54
6.20	Ice II structure.	56
6.21	Alternative ice II unit cell, top view.	56
6.22	Alternative ice II unit cell, side view.	57
6.23	Ice II - PBE, RPA+EXX and RPA+SCHF energy-volume curves.	58
6.24	Ice XIII structure.	60
6.25	Ice XIII - PBE energy-volume curves.	60
6.26	Ice XV structure.	61
6.27	Ice XV - PBE, RPA+EXX and RPA+SCHF energy-volume curves.	62
6.28	Ice VIII structure.	64
6.29	Ice VIII - PBE, RPA+EXX and RPA+SCHF energy-volume curves.	65
6.30	Ice X structure.	66
6.31	Ice X - PBE, RPA+EXX and RPA+SCHF energy-volume curves.	67
6.32	Pressure over cell parameter diagram of ice X.	68
6.33	Total energies relative to ice I_h	71
6.34	Equilibrium volumes.	72
7.1	Ice I_c (ord. a) structure.	76
7.2	Ice I_c (ord. b) structure.	76
7.3	Ice I_c (ord. c) structure.	76
7.4	Ice I_c (ord. d) structure.	77
7.5	Far-IR intensities from [Bertie and Jacobs, 1977].	77
7.6	Far-IR intensities from [Profeta and Scandolo, 2011].	78
7.7	Ice I_c (ord. a) IR spectrum.	78
7.8	Ice I_c (ord. b) IR spectrum.	79
7.9	Ice I_c (ord. c) IR spectrum.	79
7.10	Ice I_c (ord. d) IR spectrum.	80
7.11	Ice I_h IR spectrum.	80
7.12	Ice XI Cmc ₂₁ IR spectrum.	81
7.13	Ice XI Pna ₂₁ IR spectrum.	81

List of Tables

6.1	Phases investigated.	34
6.2	Structural results for ice I_h	38
6.3	Results for ice I_h	40
6.4	Structural results for ice XI Cmc2 ₁	43
6.5	Results for ice XI Cmc2 ₁	43
6.6	Structural results for ice XI Pna2 ₁	44
6.7	Results for ice XI Pna2 ₁	46
6.8	Structural results for ice I_c	47
6.9	Results for ice I_c	52
6.10	Structural results for ice IX.	55
6.11	Results for ice IX.	55
6.12	Structural results for ice II.	57
6.13	Results for ice II.	59
6.14	Structural results for ice XIII.	60
6.15	Results for ice XIII.	61
6.16	Structural results for ice XV.	63
6.17	Results for ice XV.	63
6.18	Structural results for ice VIII.	64
6.19	Results for ice VIII.	66
6.20	Structural results for ice X.	69
6.21	Results for ice X.	69
6.22	Energy contribution to the total energy from PBE, RPA+EXX and RPA+SCHF calculations	73

Chapter 1

Introduction

The study of the water structure is an ongoing issue and dates back many years. Computers constantly open up new possibilities and over the years many models for the description of water have been invented. Different levels of theory provide more or less accurate results when it comes to calculating the properties of water in its different phases. Although the water phase diagram is mostly known, new experiments permanently shift the phase boundaries in particular in the high pressure range.

The quality of a simulation of condensed water depends largely on the accuracy of the description of long-range electronic correlation effects. It has been found, that the van der Waals interaction plays an important role in the description of water, especially in high pressure ice phases ([Santra et al., 2011]) but also increases the accuracy in general ([Santra et al., 2013]). Nevertheless, none of the methods was able to give energetically and structurally (lattice parameters, volume) accurate results at the same time.

The vdW interaction is a non-local electronic correlation effect and a local (LDA) and even gradient corrected approximations (GGA) in density functional theory (DFT) cannot reproduce it. Efforts to include vdW in DFT functionals have led to some improvements but the required parameters in all those vdW methods, mostly optimized for small systems, may not perform well on condensed phases ([Santra et al., 2013]).

ACFDT in the RPA (see Chap. 3.4) has been shown to be able to reproduce dispersion forces both from a theoretical view and in practical applications ([Björkman et al., 2012, p. 15] [Dobson, 2010]). Our main goal is to proof the reasonableness of RPA for water ice.

Several ice phase have been investigated. They are, in increasing order of pressure:

- the low pressure proton disordered hexagonal ice I_h
- the most stable proton ordered form of ice I_h , ice XI Cmc2_1
- the second most stable proton ordered form of ice I_h , ice XI Pna2_1
- four low pressure proton ordered cubic ice phases I_c orders a-d
- the proton ordered form of ice III, ice IX

- the proton ordered ice II without a direct disordered counterpart
- the proton ordered form of ice V, ice XIII
- the proton ordered form of ice VI, ice XV
- the proton ordered form of ice VII, high pressure ice VIII
- the symmetric high pressure ice X, formed from ice VII under increasing pressure

In chapter 2, the most significant properties of the water molecule and an overview of the various ice phases are presented. Chapters 3 and 4 introduce the theoretical framework this work is based on. While the focus of chapter 3 is on the advanced methods of computing the ground state, chapter 4 deals with excited states and linear response as well as one of its application, the infrared spectroscopy. The computational setup is presented in chapter 5. The results from DFT and RPA calculation are shown in chapter 6, infrared intensities from linear response theory are presented in chapter 7. This work closes with chapter 8 summing up the main goals and findings of this thesis.

Chapter 2

Properties of water and ice

On earth's surface, water is the most occurring compound and the importance of understanding its physical and chemical nature is obvious:

- All known life forms depend on water
- A lot of chemical reactions include water molecules
- Many geological processes depend on water
- The weather and many more processes include water

Despite the huge amount of research, the ultimate phase diagram of water does not yet exist. Considering the experimental difficulties encountered in the study of water, *ab initio* calculations are of great importance to predict new phases or to interpret those observed experimentally.

On earth, water naturally exists in 3 states: fluid, solid and gaseous. Already in the 1780s it has been discovered, that its components are oxygen and hydrogen. Besides the common H_2O , about 0.2 per cent of the water are stable isotopes. In this chapter the main physical characteristics of water will be summarized, with a special emphasis on the structural and bonding properties.

2.1 The H_2O molecule

The H_2O consists of an oxygen atom covalently bonded to two hydrogen atoms. The H-O-H structure is not straight. In equilibrium, the free molecule has a O-H-distance of 95.72 ± 0.03 pm and a H-O-H angle of 104.52° . The molecule has point group C_{2v} with 2 mirror planes and a 2-fold rotation axis. The angle and bond length can be measured very accurately by determining the moments of inertia in a vibrational spectrum analysis ([Eisenberg, 2005, Chap. 1, p4]). The special H_2O structure is strongly connected to various anomalies of water and also enables the different unique crystal structures of ice.

The atoms of the water molecule undergo permanent vibrations even at 0 K, which are the zero-point motions caused by the uncertainty principle. A free molecule has three normal modes of vibration, which are a symmetric stretching at 3657 cm^{-1} , a bending at 1595 cm^{-1} and an asymmetric stretching at 3756 cm^{-1} .

The electronic charge distribution of the molecule gives rise to an electrical polarization. The permanent dipole moment of about 1.84 D is another indication for a bent structure, as it forbids a molecular center of symmetry. The polarization is the reason for the wide H-O-H angle, because the larger H-H distance is energetically favorable ([Maskos, 2009]).

Another electrical property of water is its polarizability α , defined as the ratio with which an electric field \mathbf{E} is able to induce a dipole moment $\mathbf{p} = \alpha \mathbf{E}$.

While infrared spectroscopy depends on the change of the dipole moment, in Raman spectroscopy the change of the molecules polarizability is the factor determining the intensity.

When the distinct $1s^1$ orbitals of hydrogen and the $1s^2 2s^2 2p^4$ orbitals of the oxygen atom are brought together, O-H bonds are formed by the interaction of the hydrogen's $1s$ orbital with the $2s$ and $2p$ orbitals of the oxygen. In fact, the $1s$ orbital of the oxygen stays tightly bound to the nuclei, while the $2s$ and $2p$ orbitals form 4 sp^3 hybrid orbitals. Two of them form σ -bonds with the hydrogen atoms and the remaining two are occupied by lone pair electrons.

The molecule orbitals form in a way, so that a tetrahedral structure with 2 hydrogen atoms and 2 lone pairs is developed (Fig. 2.1). The initially proposed sp^3 hybrid bonding scheme has been recently doubted by an *ab initio* study which indicates that the formation of the tetrahedron originates from a sp^2 hybrid plus a p_z orbital ([Ning et al., 2008]). It is likely, that the hybridisation is somewhere between that of sp^2 and sp^3 .

The negative charge is not concentrated at the 2 edges of the tetrahedron, but more evenly smeared out between them. An electron density contour map in the molecular y-z plane is shown in Fig. 2.2.

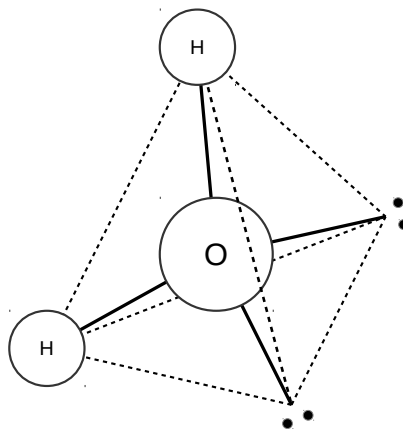


Figure 2.1: The tetrahedral structure of the H_2O molecule.

2.2 The water phase diagram

In its crystal form the well known hexagonal ice I_h is just one out of various other phases. Especially in the recent years, several new phases have been predicted

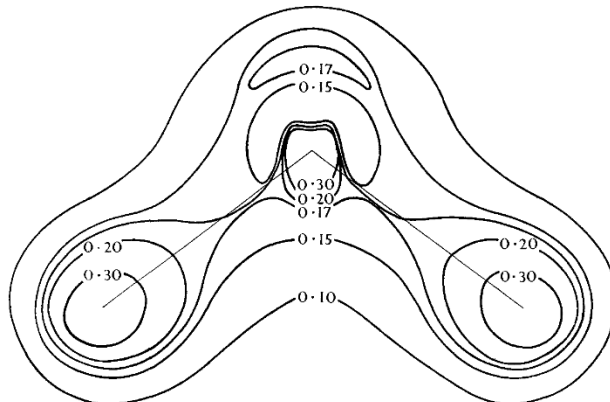


Figure 2.2: The electron density contour map in the molecular y-z plane with densities in atomic units ([Eisenberg, 2005, Chap. 1, p26]).

by theory or experimentally discovered. Because of slow transformations or metastabilities, not every phase has been examined by experiment yet and some of them probably never will. Fig. 2.3 shows all currently known phases in a pressure-temperature phase diagram.

The pressure range, in which ice phases can be found, is quite large. Starting at and below ambient pressure, the low-pressure ices hexagonal ice I_h and cubic ice I_c , as well as ice XI exist up to about 200 MPa. Phases of moderate pressure are found between about 200 and 2000 MPa. High-pressure ice phases VII, VIII and X can be found above that range. In addition, low-density amorphous ice (LDA), high-density amorphous ice (HDA) and very-high-density amorphous ice exist, but are not covered by this work.

A couple of phase designations are subject to some confusion ([Chaplin, 2012]): Two groups have reported about different 'ice XI', whereas Pbcm XI is also known as XIII in some literature. However, the ice XIII treated in this work has nothing to do with ice Pbcm XI, instead it is the proton ordered ice V (see phase diagram, Fig. 2.3). The two versions of ice XI in this work are a proton order form of ice I_h and should not be confused with Pbcm XI. In literature, versions of 'ice X' may be found, which are now known as and treated in this work as ice XV.

Various transitions in the phase diagram have to be verified experimentally and so the phase diagram is under permanent change.

2.3 The ice crystal, ice rules

In crystal form (and in liquid form too), the H_2O molecule differs somewhat from its free (gaseous) form: the bond lengths and H-O-H angle are slightly disturbed, depending on the particular ice phase. The H-O-H angle is expected to be a little less than the tetrahedral angle of 109.47° .

In ice, in addition to the two covalently bonded hydrogen atoms, each oxygen atom is connected to two hydrogen atoms belonging to other water molecules. This is the so called hydrogen bond which will be described in more detail in

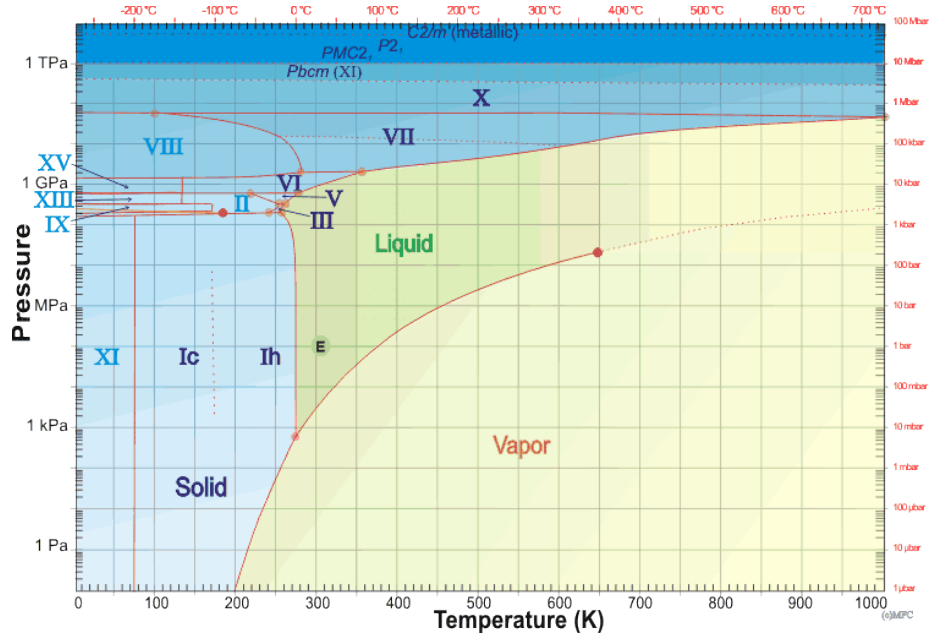


Figure 2.3: Phase diagram of water (source: [Chaplin, 2012]).

the next section. The O-H...O bond forms an almost straight line. Due to these overall 4 bonds (2 covalently and 2 hydrogen bonds) per oxygen, an almost tetrahedral arrangement of oxygen atoms is reached (Fig. 2.4).

For a single oxygen in the tetrahedron, there are $\binom{4}{2} = 6$ ways to place the hydrogen along the four tetrahedral bond directions. The infinite amount of possible configurations in the infinite solid can now be grouped into two categories:

- Structures with the same hydrogen configuration in every unit cell are called proton (hydrogen) ordered.
- All others are proton disordered and share the same oxygen network in every unit cell.

The only properties, which are common to hexagonal ice and other proton disordered water ices, are the *Bernal-Fowler rules*, also known as *ice rules*: There is exactly one hydrogen between two oxygen atoms and every oxygen must have exactly two hydrogen atoms covalently bonded.

Most ice phases appear in ordered-disordered pairs in which a phase transition does not change the oxygen structure, but the hydrogen atoms may relax to ordered positions often by making use of defects. The hydrogen atoms are permanently jumping between the possible sites, and any of the six possible configurations allowed by the ice rules occurs equally likely. The disorder of hexagonal ice remains even when lowering the temperature towards zero due to the now slower moving defects. It was found, that this disorder leads to a residual zero-point entropy of about $R \cdot \ln(3/2) \approx 3.41 \text{ J/molK}$ ([Pauling, 1935]) in hexagonal ice. Nevertheless, a transition to the ordered counterpart, ice XI, may be reached as well with the help of impurities at low temperatures. A more

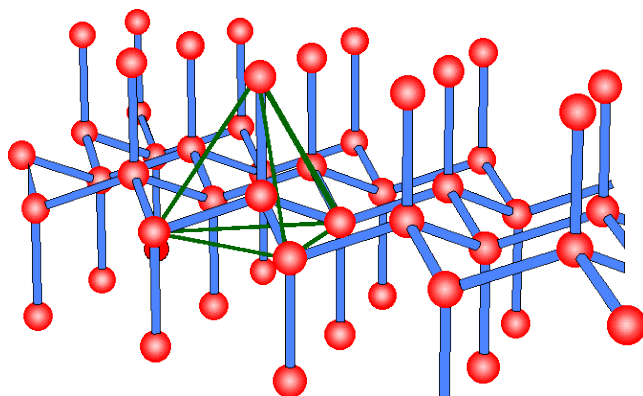


Figure 2.4: Tetrahedral arrangement of oxygen atoms ([de Podesta, 2013]).

detailed description of the ice phases considered in the present study will be given in Chapter 6.

2.4 The hydrogen bond

The hydrogen bond is a dipole-dipole interaction, in which hydrogen is bonded to a highly electronegative atom. In water, it has been studied to a large extent (see [Chaplin, 2013]): It was found that 90 % of the interaction is electrostatic and the rest is covalent. The directional nature of the hydrogen bonds restricts them to 4 connections per water molecule, while van der Waals (vdW) bonded systems may have more neighbors.

With 5-30 kJ/mol it is positioned between the weaker van der Waals interaction and the stronger covalent and ionic bondings. A hydrogen bond donor is present, when a hydrogen atom is attached to a relatively electronegative atom. Then the electron cloud of the hydrogen is deformed towards the electronegative atom and a positive partial charge is formed. A pictorial representation of the hydrogen bond in water is given in Fig. 2.5. This particular atomic configuration enables the acceptance of another electronegative atom at the positive partial charge which may or may not have other hydrogen atoms attached to itself. In the H_2O molecule, each of the 2 lone pairs (Fig. 2.1) acts as an acceptor. This behavior encourages further connections and leads to cluster formations in liquid water.

When entering into a hydrogen bond, the hydrogen atom moves towards the hydrogen bonded oxygen, away from the covalently bonded oxygen and similarly, the lone-pair stretches away from its oxygen atom. Several effects influence the bond length and strength and therefore also the vibrational frequencies: The formation of clusters further increases the O-H distance and decreases the $\text{H}\cdots\text{O}$ and $\text{O}\cdots\text{O}$ distances. Electromagnetic and magnetic effects may affect the hydrogen bond strength. Comparatively strong bending of the bond leads to a substantial weakening of the bond strength. At higher pressures or lower temperatures, the covalent bond is less affected by the densification than the hydrogen bond, leading to a shortening of the hydrogen bond. The strength of the hydrogen bond affects the strength of the corresponding covalent bond: a

Hydrogen Bonding in Water

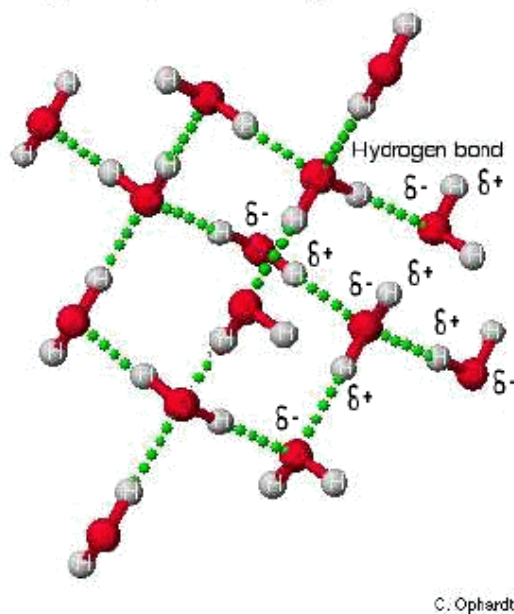


Figure 2.5: Hydrogen bonding ([Ophardt, 2003]).

stronger $\text{H} \cdots \text{O}$ bond leads to a weaker $\text{O}-\text{H}$ covalent bond (and vice versa) and overall to a shorter $\text{O} \cdots \text{O}$ distance. Upon increasing pressure, therefore, the $\text{O}-\text{H}$ bond becomes stretched. Figs. 2.6 and 2.7 show an average molecule link in liquid water. The ideal tetrahedral structure shown in Fig. 2.6 is normally not reached in liquid water. While the directional hydrogen bonds to the molecules denoted 'a' in Fig. 2.6 are less susceptible to deviations, the smeared out lone-pairs holding the 'd' molecules lead to larger deviations (see Chap. 2.1) from the 109° bond angle.

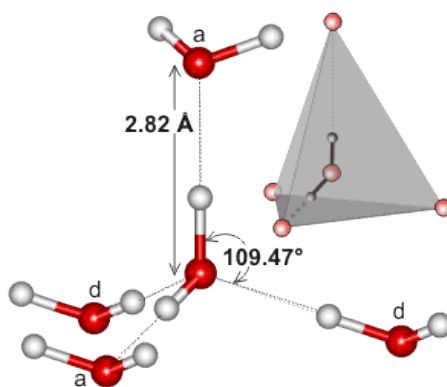


Figure 2.6: Average hydrogen bond in liquid water, H-O-H angle and distance ([Chaplin, 2013]).

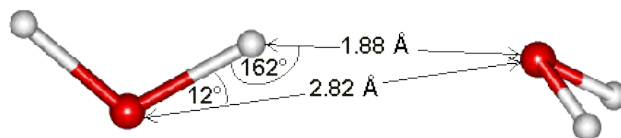


Figure 2.7: Average hydrogen bond in liquid water, O-H-O angles and distances ([Chaplin, 2013]).

2.5 The van der Waals interaction

The van der Waals interaction, although a very weak force, plays an important role in various scientific fields. It is defined ([Nic, 1994]) as all attractive or repulsive forces between molecules (or groups of atoms within the same molecule) excluding forces due to bond formation and forces due to electrostatic interaction of ions or of ionic groups with one another or with neutral molecules.

The forces are caused by correlations in the fluctuating polarizations of nearby particles and include ([Wikipedia, 2013a], [Wikipedia, 2013c]):

Keesom force: attractive interactions between two permanent dipoles that are Boltzmann-averaged over different rotational orientations of the dipoles,

Debye force: attractive interaction between a permanent dipole/multipole on one molecule and a corresponding induced dipole/multipole on a second atom or molecule,

London dispersion force: quantum-induced instantaneous polarization in non-polar molecules, because of the correlated movements of the electrons in interacting molecules. The London dispersion force arises from the interaction of instantaneous multipoles in molecules without permanent multipole moments. With increasing molar mass, this force becomes the dominant part of the van der Waals interaction. In small and highly polar molecules such as water, it is less important than in noble gases. Nevertheless, the dispersion force amounts to 24 % of the total energy of the $\text{H}_2\text{O}-\text{H}_2\text{O}$ molecule interaction ([Wikipedia, 2013b]).

Chapter 3

Computational quantum mechanics

The following sections about the computational quantum mechanical methods employed in the present work are based on the detailed formulation presented in [Thijssen, 1999, Chaps. 4,5] and [Fitzpatrick, 2006]. The DFT section is based on [Fiolhais et al., 2003] and [Harrison, 2002], the ACFDT section on [Harl, 2008].

3.1 Introduction, approximations

In *ab initio* calculations of quantum systems, the many-body Schrödinger equation has to be solved. In principle, a stationary state $|\phi\rangle$ and the corresponding expectation value for the energy E of this quantum system with known Hamiltonian \hat{H} can be obtained by solving either the stationary Schrödinger equation

$$\hat{H}\phi = E\phi \quad (3.1)$$

or the variational form

$$E[\phi] = \frac{\langle \hat{H}|\phi|\hat{H} \rangle}{\langle \hat{H}|\hat{H} \rangle}, \quad (3.2)$$

where the parameter dependent trial wave vector $|\phi\rangle$ is limited to a subspace of the Hilbert space. The *variational theorem* states that the solutions within an arbitrary subspace of the Hilbert space are upper bounds to the true energy and thus can be used as approximations. In spin dependent systems, the wave function $\phi(\mathbf{x}_1, \dots, \mathbf{x}_N)$ consists of $\mathbf{x}_i = (\mathbf{r}_i, s_i)$, a combined vector of electron position \mathbf{r}_i and spin s_i . The exact, non-relativistic, time-independent Hamiltonian in atomic units is

$$\hat{H} = -\frac{1}{2} \sum_{i=1}^N \nabla_i^2 - \frac{1}{2} \sum_{\alpha=1}^K \frac{\nabla_{\alpha}^2}{M_{\alpha}} - \sum_{i,\alpha} \frac{Z_{\alpha}}{|\mathbf{r}_i - \mathbf{R}_{\alpha}|} + \frac{1}{2} \sum_{i \neq j} \frac{1}{|\mathbf{r}_i - \mathbf{r}_j|} + \frac{1}{2} \sum_{\alpha \neq \beta} \frac{1}{|\mathbf{R}_{\alpha} - \mathbf{R}_{\beta}|}, \quad (3.3)$$

where the first two terms represent the kinetic energies of the electrons and the nuclei, respectively. N is the total number of electrons and K the total number of nuclei. The third term is the attracting Coulomb interaction between the

electrons and the nuclei and finally the last two are the repulsive Coulomb terms for the electrons and nuclei. The indices i and α refer to electrons and nuclei, respectively. In atomic units, the atomic number Z_α and atomic mass M_α are the only constants used.

In principle, the above equations would lead to an exact solution of the many-body problem. The high-dimensionality, however, limits exact solutions to just a few particles, in practice. Therefore, *ab initio* methods have to utilize various approximations, which are described in the following sections.

3.1.1 The Born-Oppenheimer approximation

The wave function ϕ and the Hamiltonian depend on the particle positions \mathbf{R}_α and \mathbf{r}_i as well as the spin s_i . The Coulomb interactions thus make solving the Schrödinger equation difficult for more than a few particles. For *ab initio* calculations it is therefore common to apply the Born-Oppenheimer (BO) approximation, which consists in a separation of degrees of freedom, that is, decoupling the motion of nuclei and electrons. The much heavier nuclei are assumed to be fixed in space from the perspective of electrons. The kinetic energy operator of the nuclei as well as the Coulomb interaction between the nuclei are separated from the Hamiltonian. The Coulomb potential between nuclei and electrons can be regarded as an external potential to the electrons and thus the positions of the nuclei, \mathbf{R}_α , enter the electronic Hamiltonian

$$\hat{H}_{\text{BO}} = -\frac{1}{2} \sum_{i=1}^N \nabla_i^2 - \sum_{i,\alpha} \frac{Z_\alpha}{|\mathbf{r}_i - \mathbf{R}_\alpha|} + \frac{1}{2} \sum_{i \neq j} \frac{1}{|\mathbf{r}_i - \mathbf{r}_j|} \quad (3.4)$$

only as parameters. Within the Born-Oppenheimer approximation, the ground state of the system can be determined by varying the positions of the nuclei until a minimum energy is found. In order to get the total energy, the Coulomb term and the kinetic term of the nuclei, have to be taken into account. They can be calculated separately within the BO approximation.

3.1.2 Independent particle approximation

Usually, even within the Born-Oppenheimer approximation, calculations remain challenging due to the many degrees of freedom involved in the electron-electron interaction. These many-body interactions, neglecting time dependence, may collectively be written as a potential $V_{\text{MB}}(\mathbf{r}_1, \mathbf{r}_2, \mathbf{r}_3, \dots, \mathbf{r}_N)$. Supposing non-interacting electrons, the potential can be written as sum over individual potentials

$$V_{\text{IP}} = \sum_{i=1}^N V(\mathbf{r}_i) \quad (3.5)$$

each part only depending on an one-electron position. The Hamiltonian for such a system is split into a sum of one-particle Hamiltonians

$$\hat{H}_{\text{IP}} = -\sum_{i=1}^N \frac{1}{2} \nabla_i^2 + \hat{V}(\mathbf{r}_i), \quad (3.6)$$

where usually the potential function \hat{V} is the same for all electrons. Because of the now uncorrelated electrons, the many-body wave function $\phi_{\text{MB}}(\mathbf{x}_1, \mathbf{x}_2, \mathbf{x}_3, \dots, \mathbf{x}_N)$ can be written as a product of one-electron states

$$\phi(\mathbf{x}_1, \mathbf{x}_2, \mathbf{x}_3, \dots, \mathbf{x}_N) = \phi_1(\mathbf{x}_1) \dots \phi_N(\mathbf{x}_N) \quad (3.7)$$

or as a linear combination of such products to satisfy the anti-symmetry requirement of fermions. Now, instead of a many-body problem there only have to be solved N one-electron Schrödinger equations of the form

$$\hat{H}\phi_i(\mathbf{x}_i) = E_i\phi_i(\mathbf{x}_i), \quad (3.8)$$

where ϕ_i are called “orbitals”, or “spin-orbitals” in systems with spin taken into account. The resulting energy is the sum of the eigenvalues E_i .

This oversimplistic method however neglects the antisymmetry of the electronic wavefunction as well as the electrostatic interaction between the electrons.

3.2 Hartree-Fock theory

A more accurate method for solving the electronic Schrödinger equation is given by the Hartree-Fock approximation. It makes use of the independent particle approximation and assumes that the wave-function can be written as a *single* Slater determinant of one-electron orbitals (Eq. (3.7)). In the case of fermions, such as electrons, the total wave function of the system has to be anti-symmetric with respect to the exchange of two particles. This requirement can be fulfilled by a linear combination of antisymmetrized products of one-electron states. In Hartree-Fock theory the wave function is restricted to such a single linear combination. With a minimal number of terms, in general, this is written as

$$\phi(\mathbf{x}_1, \dots, \mathbf{x}_N) = \frac{1}{\sqrt{N!}} \sum_{\mathbf{P}} \epsilon_{\mathbf{P}} \mathbf{P} \phi_1(\mathbf{x}_1) \dots \phi_N(\mathbf{x}_N) \quad (3.9)$$

and equivalently can be written as Slater determinant

$$\phi = \phi_1(\mathbf{x}_1) \dots \phi_N(\mathbf{x}_N) = \frac{1}{\sqrt{N!}} \begin{vmatrix} \phi_1(\mathbf{x}_1) & \phi_2(\mathbf{x}_1) & \dots & \phi_N(\mathbf{x}_1) \\ \phi_1(\mathbf{x}_2) & \phi_2(\mathbf{x}_2) & \dots & \phi_N(\mathbf{x}_2) \\ \vdots & \vdots & \ddots & \vdots \\ \phi_1(\mathbf{x}_N) & \phi_2(\mathbf{x}_N) & \dots & \phi_N(\mathbf{x}_N) \end{vmatrix}. \quad (3.10)$$

The permutation operator \mathbf{P} permutes the positions of the spin-orbitals and $\epsilon_{\mathbf{P}}$ equals to $+1/-1$ for an even/odd number of permutations. The Slater determinant suffices the Pauli exclusion principle as the value gets zero when two electrons occupy the same state. By neglecting the anti-symmetry requirement, a single product of spin-orbitals $\phi_1(\mathbf{x}_1) \dots \phi_N(\mathbf{x}_N)$ is sufficient. Applying the Hamiltonian to this wave function, one can now multiply the Schrödinger equation by $\phi_l^*(\mathbf{x}_l)$ from the left. Integrating over all but one r_i and summing up s_i , an equation of the independent particle form of Eq. (3.6) is reached:

$$\left[-\frac{1}{2} \nabla^2 - \sum_{\alpha} \frac{Z_{\alpha}}{|\mathbf{r} - \mathbf{R}_{\alpha}|} + \sum_{s'} \sum_l^N \int d^3 r' |\phi_l(\mathbf{r}', s')|^2 \frac{1}{|\mathbf{r} - \mathbf{r}'|} \right] \phi_k(\mathbf{r}, s) = E' \phi_k(\mathbf{r}, s). \quad (3.11)$$

The last term on the left hand side is the Hartree potential in which electron k feels the average potential of all electrons, unfortunately including the k -th orbital itself. Excluding the term would make the operator different for each orbital dramatically increasing the computational load. A physically more reasonable result can be obtained by choosing a Slater determinant as wave function. Such a wave function includes the anti-symmetry requirement and leads to the Schrödinger equation

$$\begin{aligned} \mathcal{F}\phi_k(\mathbf{r}, s) = & \left[-\frac{1}{2}\nabla^2 - \sum_n \frac{Z_n}{|\mathbf{r} - \mathbf{R}_n|} + \sum_{s'} \sum_l^N \int d^3r' |\phi_l(\mathbf{r}', s')|^2 \frac{1}{|\mathbf{r} - \mathbf{r}'|} \right] \phi_k(\mathbf{r}, s) - \\ & - \frac{1}{2} \sum_{s'} \sum_{l,k}^N \int d^3r d^3r' \frac{\phi_k^*(\mathbf{r}, s') \phi_l^*(\mathbf{r}, s') \phi_l(\mathbf{r}', s') \phi_k(\mathbf{r}', s')}{|\mathbf{r} - \mathbf{r}'|} = E^{\text{HF}} \phi_k(\mathbf{r}, s) \end{aligned} \quad (3.12)$$

with Fock operator \mathcal{F} , acting on orbital ϕ_k .

The difference to Eq. (3.11) is the last term in 3.12, which yields an energy contribution

$$E_x^{\text{HF}} = \frac{1}{2} \sum_s \sum_{l,k}^N \int d^3r d^3r' \frac{\phi_k^*(\mathbf{r}, s) \phi_l^*(\mathbf{r}, s) \phi_l(\mathbf{r}', s) \phi_k(\mathbf{r}', s)}{|\mathbf{r} - \mathbf{r}'|} \quad (3.13)$$

which reflects the anti-symmetry of the Slater determinant. It defines the exchange energy due to the anti-symmetry of the total electron wave function. As part of the *random phase approximation* (RPA) (Chap. 3.4, Eq. (3.43)) it will be used as the *exact exchange* energy (EXX).

Eq. (3.12) is non-linear and has to be solved self-consistently. Starting with a trial Slater determinant as wave-function for orbitals entering Eq. (3.12) with index l , the Fock operator is built. Eq. (3.12) can be solved easily, as it consists of an one-electron eigenvalue problem. The resulting orbitals ϕ_k are then used as input again in a next round. This procedure is repeated, until input and output orbitals change only slightly. In the Hartree-Fock approximation, correlations between electrons are neglected entirely, but exchange energy is taken into account exactly.

3.3 Density functional theory

The Hartree-Fock equations are successful in describing various systems, but the fact that the exchange term is non-local, complicates calculations and the lack of correlation limits their predictive power. In 1964, an alternative theory was proposed by Hohenberg and Kohn ([Hohenberg and Kohn, 1964]) which originates from the fact, that *all* properties of a system are uniquely described by *functionals* of the scalar electron ground state density. This theory is known as Density Functional Theory (DFT) and is based on the Hohenberg-Kohn theory and the Kohn-Sham schemes, which are briefly reviewed in the coming sections. Comprehensive introductions to DFT can be found in [Capelle, 2006], [Harrison, 2002] and [Martin, 2004, Chaps. 6,7].

3.3.1 Hohenberg-Kohn theorems

The H-K theorems show that all the properties (observables) of a system can be uniquely described by the functional of the electronic density $n(\mathbf{r})$. This reduces the many-body problem of N electrons ($3N$ spatial coordinates) to 3 spatial coordinates. Hohenberg and Kohn introduced the energy functional

$$E_{\text{HK}}[n] := F[n] + \int d^3r n(\mathbf{r})v_{\text{ext}}(\mathbf{r}) \quad (3.14)$$

with

$$F[n] := \min_{\psi \rightarrow n} \langle \psi | \hat{T} + \hat{V}_{\text{ee}} | \psi \rangle \quad (3.15)$$

being a unique functional of the density $n(\mathbf{r})$. Hohenberg and Kohn proved that

- In an arbitrary, non-degenerate system with N interacting electrons in an external potential v_{ext} , the (unknown) functional $F[n]$ is uniquely determined by the particle density $n(\mathbf{r})$.
- $E_{\text{HK}}[n]$ is always an upper bound to the exact ground state energy.
- At the ground state density, $E_{\text{HK}}[n]$ reaches the exact ground state energy.

The usual solution of the Schrödinger equation is to, outgoing from an external potential v_{ext} , obtain the wavefunctions including the ground state and with that, the ground state density. The H-K theorems close the circle by showing that this mapping is bijective, i.e. it is also possible to calculate from the density $n(\mathbf{r})$ the original potential $v_{\text{ext}}(\mathbf{r})$. This is the left hand side of Fig. 3.1. The H-K theorems were later generalized by [Levy, 1979].

3.3.2 Kohn-Sham *ansatz*

The H-K theorem itself does not help in finding a solution because of the difficulty of obtaining general properties of the system directly from the density.

In 1965, Kohn and Sham showed a way to map the problem of solving a system of interacting particles onto a problem of solving a system of non-interacting particles ([Kohn and Sham, 1965]). As an assumption, they made the *ansatz*, that there exists a fictitious system of non-interacting particles, the so called the Kohn-Sham system, with the same ground state density as the interacting system. To this auxiliary system, the H-K theorem is applied. The K-S system is solved more easily and delivers the ground state energy and density of the original problem. The connection of the systems is shown in Fig. 3.1.

The Hamiltonian for an interacting electron system with applied Born-Oppenheimer approximation (Eq. (3.4)) can shortly be written as

$$\hat{H} = \hat{T} + \hat{V}_{\text{ext}} + \hat{V}_{\text{ee}}, \quad (3.16)$$

where \hat{V}_{ext} represents the external potential and \hat{V}_{ee} the electron-electron Coulomb interaction.

The corresponding energy functional

$$E[n] = T[n] + V_{\text{ext}}[n] + V_{\text{ee}}[n] \quad (3.17)$$

includes the trivial term

$$V_{\text{ext}}[n] = \int v_{\text{ext}}(\mathbf{r})n(\mathbf{r})d^3r \quad (3.18)$$

with the external potential v_{ext} built by the nuclei, but T and V_{ee} are unknown. T formally can be splitted into a kinetic energy part of a non-interacting system, T_s , and the remaining correlations, T_c . This non-interacting kinetic energy,

$$T_s[n] = -\frac{1}{2} \sum_i^N \langle \phi_i | \nabla^2 | \phi_i \rangle, \quad (3.19)$$

can not explicitly be written in terms of n . But implicitly, because ϕ_i itself is a functional of n . n in turn is built by the orbitals ϕ_i :

$$n(\mathbf{r}) = \sum_i^N |\phi_i(\mathbf{r})|^2 \quad (3.20)$$

V_{ee} can be split into a Hartree energy part,

$$V_{\text{H}}[n] = \frac{1}{2} \int \frac{n(\mathbf{r}_1)n(\mathbf{r}_2)}{|\mathbf{r}_1 - \mathbf{r}_2|} d^3r_1 d^3r_2, \quad (3.21)$$

which is the Coulomb interaction of a non-interacting system, and a part with the remaining correlations. Kohn and Sham introduced the exchange-correlation functional E_{xc} , which is the sum of the errors made in using a non-interacting kinetic energy and ignoring exchange energies:

$$E_{\text{xc}}[n] = (T[n] - T_s[n]) + (V_{\text{ee}}[n] - V_{\text{H}}[n]). \quad (3.22)$$

A great amount of energy of the true system already is included in T_s and V_{H} , therefore E_{xc} is comparatively small.

3.3.3 Kohn-Sham equations

The energy functional, Eq. (3.17), after introduction of E_{xc} , reads

$$E[n] = T_s[n] + V_{\text{ext}}[n] + V_{\text{H}}[n] + E_{\text{xc}}[n]. \quad (3.23)$$

At the energy minimum,

$$0 = \frac{\partial E[n]}{\partial n(\mathbf{r})} = \frac{\partial T_s[n]}{\partial n(\mathbf{r})} + \frac{\partial V_{\text{ext}}[n]}{\partial n(\mathbf{r})} + \frac{\partial V_{\text{H}}[n]}{\partial n(\mathbf{r})} + \frac{\partial E_{\text{xc}}[n]}{\partial n(\mathbf{r})} \quad (3.24)$$

holds. Introducing the Hartree potential (the derivative of Eq. (3.21) with respect to $n(\mathbf{r})$),

$$v_{\text{H}}[n](\mathbf{r}) = \int d^3r' \frac{n(\mathbf{r}')}{|\mathbf{r} - \mathbf{r}'|}, \quad (3.25)$$

deriving Eq. (3.18) and further introducing the exchange-correlation potential

$$v_{\text{xc}} = \frac{\partial E_{\text{xc}}}{\partial n}, \quad (3.26)$$

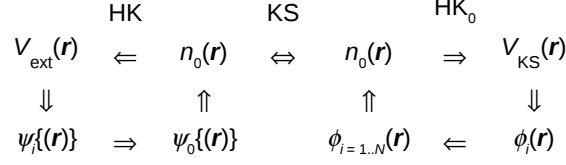


Figure 3.1: Schematic representation of the Kohn-Sham *ansatz*. The left hand side represents the interacting problem with applied H-K theorem to close the circle. The right hand side represents the H-K theorem applied to the non-interacting system, the K-S system. The electron-electron interaction is set to zero and a new external potential, V_{KS} , is introduced. V_{KS} is chosen such that energy and density of the KS system are equal to the interacting one. Via the *ansatz* of using n_0 of the interacting for the non-interacting one, in principle all properties of the interacting system can be obtained by solving the K-S system.

Eq. (3.24) is rewritten as

$$0 = \frac{\partial E[n]}{\partial n(\mathbf{r})} = \frac{\partial T_s[n]}{\partial n(\mathbf{r})} + v_{\text{ext}}(\mathbf{r}) + v_{\text{H}}(\mathbf{r}) + v_{\text{xc}}(\mathbf{r}). \quad (3.27)$$

For a non-interacting system, the Kohn-Sham system, v_{H} and v_{xc} is zero, and therefore

$$0 = \frac{\partial E_s[n]}{\partial n(\mathbf{r})} = \frac{\partial T_s[n]}{\partial n(\mathbf{r})} + v_s(\mathbf{r}). \quad (3.28)$$

In this system, electrons move in the potential v_s and the density solving Eq. (3.28) is of the non-interacting form, n_s . The KS system is connected to the true system (Eq. (3.27)) in the manner that, if v_s is set to

$$v_s(\mathbf{r}) = v_{\text{ext}}(\mathbf{r}) + v_{\text{H}}(\mathbf{r}) + v_{\text{xc}}(\mathbf{r}), \quad (3.29)$$

the solving densities of the true system and the Kohn-Sham system are equal and can be formed by the non-interacting orbitals ϕ_i :

$$n(\mathbf{r}) \equiv n_s(\mathbf{r}) = \sum_i^N |\phi_i|^2. \quad (3.30)$$

The Schrödinger equation of the KS system reads

$$\left[-\frac{1}{2} \nabla^2 + v_s(\mathbf{r}) \right] \phi_i = \epsilon_i \phi_i. \quad (3.31)$$

Eqs. (3.29-3.31) are the Kohn-Sham equations represented by the right hand side of Fig. 3.1. They are used to get the ground state energy $E[n]$ and electron ground state density $n(\mathbf{r})$ of the interacting system by actually solving a non-interacting, the Kohn-Sham system.

In principle, the above is exact but E_{xc} is not known. Nevertheless, the K-S system is much more easy to handle than the interacting system. In actual calculations, E_{xc} has to be approximated using concrete functionals like in the *local density approximation* (LDA) or the *generalised gradient approximation* (GGA) ([Perdew et al., 1996]).

3.4 ACFDT in the random phase approximation

In DFT calculations the exchange-correlation energy E_{xc} is often approximated within LDA, GGA or hybrid functionals, which leads to fast results but have some disadvantages not delivering highly accurate energies and lattice parameters and/or not taking long-range correlation effects into account. A method which provides more reliable results in this regard is found in the linear response theory, which provides the density-density response function. E_{xc} can be expressed as a function of this response function. This is the foundation of the adiabatic connection dissipation-fluctuation theorem (ACFDT). In principle, ACFDT yields exact correlation energies in terms of density-density response functions but for practical purposes, the random phase approximation (RPA) is applied.

3.4.1 Adiabatic connection dissipation-fluctuation theorem

Adiabatic connection

In order to arrive at an expression for E_{xc} , first a set of Hamiltonians,

$$\hat{H}(\lambda) = \hat{T} + \lambda \hat{V}_{ee} + \hat{V}_{ext}(\lambda), \quad (3.32)$$

adiabatically connected via the parameter λ , is introduced. The coupling constant sets the strength of the electron-electron interaction \hat{V}_{ee} . At $\lambda = 0$ the Kohn-Sham system is recovered, whereas at $\lambda = 1$ the exact many-electron Hamiltonian is obtained. The λ -dependence of the external potential $\hat{V}_{ext}(\lambda)$ is chosen in a way, so that the ground state density of the fully interacting system is retained. Therefore, interactions can be turned on from a KS system at $\lambda = 0$ to a fully interacting system at $\lambda = 1$. Combining the energy expressions for the exact many-electron energy

$$\begin{aligned} E &= \langle \phi(1) | \hat{H}(1) | \phi(1) \rangle = \langle \phi(1) | \hat{T} + \hat{V}_{ee} + \hat{V}_{ext}(\lambda) | \phi(1) \rangle = \\ &= \langle \phi(1) | \hat{T} + \hat{V}_{ee} | \phi(1) \rangle + E_{ext} \end{aligned} \quad (3.33)$$

and the K-S ground-state energy

$$E = \langle \phi(0) | \hat{H}(0) | \phi(0) \rangle = \langle \phi(0) | \hat{T} + \hat{V}_{ext}(\lambda) | \phi(0) \rangle = T_s + E_H + E_{ext} + E_{xc}, \quad (3.34)$$

a combined Hartree and exchange correlation energy E_{Hxc} can be written as

$$\begin{aligned} E_{Hxc} &= E_H + E_{xc} = E - E_{ext} - T_s = \\ &= \langle \phi(1) | \hat{H}(1) | \phi(1) \rangle - \langle \phi(1) | \hat{V}_{ext}(1) | \phi(1) \rangle - \\ &\quad - \langle \phi(0) | \hat{H}(0) | \phi(0) \rangle + \langle \phi(0) | \hat{V}_{ext}(0) | \phi(0) \rangle = \\ &= \int_0^1 d\lambda \frac{d}{d\lambda} \left(\langle \phi(\lambda) | \hat{H}(\lambda) | \phi(\lambda) \rangle - \langle \phi(\lambda) | \hat{V}_{ext}(\lambda) | \phi(\lambda) \rangle \right) \end{aligned} \quad (3.35)$$

and after applying the Hellmann-Feynman theorem, the expression

$$E_{Hxc} = \int_0^1 d\lambda \langle \phi(\lambda) | \hat{V}_{ee} | \phi(\lambda) \rangle \quad (3.36)$$

is obtained, that has no dependence on T and therefore also no direct dependence on the orbitals.

Fluctuation-dissipation theorem

Now E_{Hxc} is combined with the key quantity from linear response theory, the *density-density response function*

$$\chi(\mathbf{r}, \mathbf{r}', t - t') = \frac{\delta n(\mathbf{r}, t)}{\delta v_{\text{ext}}(\mathbf{r}', t')}, \quad (3.37)$$

which describes the change of the density n at (\mathbf{r}, t) , when the external potential changes at (\mathbf{r}', t') .

The expression

$$\int_0^\infty d\omega [\chi(\mathbf{r}, \mathbf{r}', i\omega) + \chi(\mathbf{r}', \mathbf{r}, i\omega)] \quad (3.38)$$

with imaginary frequency $i\omega$ can be written in terms of the density operator \hat{n} and density n ,

$$\begin{aligned} & \int_0^\infty d\omega [\chi^\lambda(\mathbf{r}, \mathbf{r}', i\omega) + \chi^\lambda(\mathbf{r}', \mathbf{r}, i\omega)] = \\ & = -\pi \{ \langle 0 | \hat{n}(\mathbf{r}) \hat{n}(\mathbf{r}') | 0 \rangle + \langle 0 | \hat{n}(\mathbf{r}') \hat{n}(\mathbf{r}) | 0 \rangle \} + 2\pi n(\mathbf{r})n(\mathbf{r}') \end{aligned} \quad (3.39)$$

and is valid for any χ^λ as introduced above. The functional E_{Hxc} (Eq. (3.36)) now is written as integral

$$E_{\text{Hxc}} = \frac{1}{2} \int_0^1 d\lambda \int d^3r d^3r' \frac{n^{2,\lambda}(\mathbf{r}, \mathbf{r}')}{|\mathbf{r} - \mathbf{r}'|} \quad (3.40)$$

over the pair density

$$n^{2,\lambda}(\mathbf{r}, \mathbf{r}') = \langle \phi(\lambda) | \hat{n}(\mathbf{r}) \hat{n}(\mathbf{r}') | \phi(\lambda) \rangle - n(\mathbf{r})\delta(\mathbf{r} - \mathbf{r}'). \quad (3.41)$$

Combining 3.40 and 3.39 leads to

$$\begin{aligned} E_{\text{Hxc}} &= \frac{1}{2} \int_0^1 d\lambda \int d^3r d^3r' \frac{1}{|\mathbf{r} - \mathbf{r}'|} \times \\ & \times \left\{ n(\mathbf{r})n(\mathbf{r}') - \left[\frac{1}{\pi} \int_0^\infty \chi^\lambda(\mathbf{r}, \mathbf{r}', i\omega) d\omega \right] - n(\mathbf{r})\delta(\mathbf{r} - \mathbf{r}') \right\}, \end{aligned} \quad (3.42)$$

where the first term is simply the Hartree energy from Eq. (3.21). Further rewriting yields an expression for the exchange-correlation energy $E_{\text{xc}} = E_x[\phi^{\text{KS}}] + E_c$ in which the exchange energy is a functional of the Kohn-Sham orbitals instead of the electron density:

$$E_x[\phi^{\text{KS}}] = -\frac{1}{2} \sum_{n(\text{occ})} \sum_{m(\text{occ})} \int d^3r d^3r' \frac{\phi_m^*(\mathbf{r}') \phi_n(\mathbf{r}') \phi_n^*(\mathbf{r}) \phi_m(\mathbf{r})}{|\mathbf{r} - \mathbf{r}'|} \quad (3.43)$$

The correlation energy in reciprocal space reads

$$E_c = - \int_0^1 d\lambda \int_0^\infty \frac{d\omega}{2\pi} \sum_{\mathbf{q} \in \text{BZ}} \sum_{\mathbf{G}} \frac{4\pi}{|\mathbf{q} + \mathbf{G}|^2} \{ \chi_{\mathbf{G}, \mathbf{G}}^\lambda(\mathbf{q}, i\omega) - \chi_{\mathbf{G}, \mathbf{G}}^{\text{KS}}(\mathbf{q}, i\omega) \}. \quad (3.44)$$

3.4.2 Random phase approximation

Eqs. (3.43) and (3.44) are exact, in principle, but the response function χ^λ is unknown. A connection between χ^{KS} and χ^λ exists in a Dyson equation, expressed in reciprocal space,

$$\begin{aligned} \chi_{\mathbf{G},\mathbf{G}'}^\lambda(\mathbf{q}, i\omega) &= \chi_{\mathbf{G},\mathbf{G}'}^{\text{KS}}(\mathbf{q}, i\omega) + \\ &+ \sum_{\mathbf{G}_1, \mathbf{G}_2} \chi_{\mathbf{G},\mathbf{G}_1}^{\text{KS}}(\mathbf{q}, i\omega) \left(\frac{4\pi\lambda}{|\mathbf{q} + \mathbf{G}_1|^2} \delta_{\mathbf{G}_1, \mathbf{G}_2} + f_{\text{xc}, \mathbf{G}_1, \mathbf{G}_2}^\lambda(\mathbf{q}, i\omega) \right) \chi_{\mathbf{G}_2, \mathbf{G}'}^\lambda(\mathbf{q}, i\omega). \end{aligned} \quad (3.45)$$

The exchange-correlation kernel in real space,

$$f_{\text{xc}}^\lambda[n](\mathbf{r}, \mathbf{r}', t - t') = \frac{v_{\text{xc}}^\lambda(\mathbf{r}, t)}{n(\mathbf{r}', t')}, \quad (3.46)$$

is the functional derivative of exchange-correlation potential with respect to the density. In the random phase approximation, this quantity is set to zero, which, after rearrangements, leads to a separation of χ^λ and χ^{KS} in reciprocal space:

$$\chi_{\mathbf{G},\mathbf{G}'}^{\text{RPA},\lambda}(\mathbf{q}, i\omega) = \sum_{\mathbf{G}_1} (1 - \lambda \chi^{\text{KS}} \nu)_{\mathbf{G},\mathbf{G}_1}^{-1} \chi_{\mathbf{G}_1, \mathbf{G}'}^{\text{KS}}(\mathbf{q}, i\omega) \quad (3.47)$$

with Coulomb kernel

$$\nu_{\mathbf{G},\mathbf{G}'}(\mathbf{q}) = \frac{4\pi}{|\mathbf{G} + \mathbf{q}|^2} \delta_{\mathbf{G},\mathbf{G}'}. \quad (3.48)$$

Finally, an expression for the correlation energy is obtained as

$$E_c = \int_0^\infty \frac{d\omega}{2\pi} \sum_{\mathbf{q} \in \text{BZ}} \sum_{\mathbf{G}} \left\{ (\ln[1 - \chi^{\text{KS}}(\mathbf{q}, i\omega) \nu(\mathbf{q})])_{\mathbf{G},\mathbf{G}'} + \nu_{\mathbf{G},\mathbf{G}'}(\mathbf{q}) \chi_{\mathbf{G},\mathbf{G}'}^{\text{KS}}(\mathbf{q}, i\omega) \right\}. \quad (3.49)$$

The usually not feasible lambda-integration is omitted in this expression. In practice, the total electronic ground-state energy from ACFDT with applied random phase approximation can be calculated by adding the Hartree-Fock energy of the Kohn-Sham system to the correlation energy from Eq. (3.49):

$$E = T_s [\{\phi^{\text{KS}}\}] + E_{\text{H}}[n] + E_x [\{\phi^{\text{KS}}\}] + E_c^{\text{RPA}} [\chi^{\text{KS}}] = E_{\text{HF}} [\{\phi^{\text{KS}}\}] + E_c^{\text{RPA}}. \quad (3.50)$$

Chapter 4

Vibrational and dynamical properties

The following sections are largely based on [Ashcroft and Mermin, 1976].

4.1 Phonons in molecules and solids

4.1.1 Dynamic lattice model

Various physical effects were shown to be unexplainable with models that keep the atoms in crystal structures at fixed positions. Effects like sound transmission, heat capacity, elastic properties and all sorts of scattering would not be possible within a static lattice model. To study such effects, we may now allow the atoms to move around their equilibrium positions \mathbf{R} on the Bravais lattice. The actual position

$$\mathbf{r}(\mathbf{R}) = \mathbf{R} + \mathbf{u}(\mathbf{R}) \quad (4.1)$$

is written as the vector sum of the Bravais lattice position \mathbf{R} and a displacement $\mathbf{u}(\mathbf{R})$. With some potential function Φ , the corresponding potential energy is

$$U = \frac{1}{2} \sum_{\mathbf{R}\mathbf{R}'} \Phi(\mathbf{r}(\mathbf{R}) - \mathbf{r}(\mathbf{R}')) = \frac{1}{2} \sum_{\mathbf{R}\mathbf{R}'} \Phi(\mathbf{R} - \mathbf{R}' + \mathbf{u}(\mathbf{R}) - \mathbf{u}(\mathbf{R}')) \quad (4.2)$$

For small displacements (or better: small potential changes), a Taylor series in $\mathbf{u}(\mathbf{R}) - \mathbf{u}(\mathbf{R}')$ can be truncated at the quadratic term. This approximation is sufficient to describe a lot of physical properties and is called the *harmonic approximation*. As there is no change in energy when the crystal is moved as a whole, the linear term vanishes. In many dynamical problems, the constant amount of energy from the equilibrium position

$$U^{\text{eq}} = \frac{1}{2} \sum_{\mathbf{R}\mathbf{R}'} \Phi(\mathbf{R} - \mathbf{R}') \quad (4.3)$$

is subtracted and the energy in the harmonic approximation then is written as

$$U^{\text{harm}} = U - U^{\text{eq}} = \frac{1}{4} \sum_{\mathbf{R}\mathbf{R}'} \sum_{\mu, \nu=x,y,z} [u_{\mu}(\mathbf{R}) - u_{\mu}(\mathbf{R}')] \Phi_{\mu\nu}(\mathbf{R} - \mathbf{R}') [u_{\nu}(\mathbf{R}) - u_{\nu}(\mathbf{R}')] \quad (4.4)$$

$$\Phi_{\mu\nu}(\mathbf{r}) = \frac{\partial^2 \Phi(\mathbf{d})}{\partial d_\mu \partial d_\nu} \quad (4.5)$$

with $\mathbf{d} = \mathbf{R} - \mathbf{R}'$. A more common form of writing this is

$$U^{\text{harm}} = \sum_{\mathbf{R}\mathbf{R}'\mu\nu} u_\mu(\mathbf{R}) D_{\mu\nu}(\mathbf{R} - \mathbf{R}') u_\nu(\mathbf{R}') \quad (4.6)$$

with

$$D_{\mu\nu}(\mathbf{R} - \mathbf{R}') = \delta_{\mathbf{R},\mathbf{R}'} \sum_{\mathbf{R}''} \Phi_{\mu\nu}(\mathbf{R} - \mathbf{R}'') - \Phi_{\mu\nu}(\mathbf{R} - \mathbf{R}'). \quad (4.7)$$

The moving atoms imply that the wave-function is changing continuously. As it is difficult considering the states, in which the electrons are not in an equilibrium, commonly the *adiabatic approximation* is applied, which makes use of the fact, that the electrons move much faster than the nucleus (a fact, that is also used in the Born-Oppenheimer approximation, Sec. 3.1.1).

4.1.2 Normal modes

For a large enough system, where surface effects are of no importance to the oscillations within the crystal, the *Born-von Karman periodic boundary conditions* ([Ashcroft and Mermin, 1976, Chap. 22, p431]) may be applied in order to describe the system with a single unit cell. The boundary conditions lead to a finite number of distinct solutions. In the harmonic approximation, the displacements $\mathbf{u}(\mathbf{R})$ and momenta $\mathbf{P}(\mathbf{R})$ are quadratic functions. In classical mechanics a three-dimensional crystal within this approximation can be solved exactly and with N ions the solution can be represented as $3N$ independent oscillators. These are called the normal modes of the oscillating system. There are different solutions based on the dimensionality of the problem and on whether the Bravais lattice has a basis or not, as shown for example in [Ashcroft and Mermin, 1976, Chap. 22].

4.1.3 Normal modes of an one-dimensional lattice

In a one-dimensional lattice with a one-atomic basis, the atoms have a fixed temporal equilibrium distance a and the Bravais lattice R is built by na with integer n . $u(na)$ shall be the displacement at position na (Fig. 4.2). The harmonic potential energy is

$$U^{\text{harm}} = \frac{1}{2} K \sum_n [u(na) - u([n+1]a)]^2, \quad (4.8)$$

with some coupling function K . The equations of motion are

$$M\ddot{u}(na) = -\frac{\partial U^{\text{harm}}}{\partial u(na)} = -K [2u(na) - u([n-1]a) - u([n+1]a)] \quad (4.9)$$

with mass M . The solutions shall be plane waves of the form

$$u(na, t) \propto e^{i(kna - \omega t)}. \quad (4.10)$$

Here, $k = 2\pi/\lambda$ is the wave number of the wave with wavelength λ . $\omega = 2\pi/T$ is the angular frequency of the wave and T is its period.

For a lattice with N sites and Born-von Karman boundary conditions

$$e^{ikNa} = 1 \quad (4.11)$$

from which follows that

$$k = \frac{2\pi n}{aN} \quad (4.12)$$

with integer n . The dispersion relation $\omega = \omega(k)$ is then

$$\omega = \left(a \sqrt{\frac{K}{M}} \right) |k| \quad (4.13)$$

and this single curve is called the *acoustic* branch. It is caused by the coherent movement of the lattice atoms out of their equilibrium positions.

If the basis is changed to a two-atomic one, the solution changes in the way, that an additional branch appears (Fig. 4.1). It is based on out-of-phase movements of the different atoms in one unit cell. This mode may be excited by infrared radiation and therefore is called the *optical* branch ([Wikipedia, 2013a]). Fig. 4.2 shows the acoustic and optical vibrations in a linear diatomic chain.

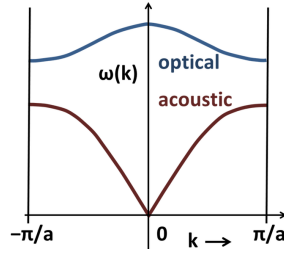


Figure 4.1: Acoustic and optical branch in an one-dimensional lattice ([Wikipedia, 2013a]).

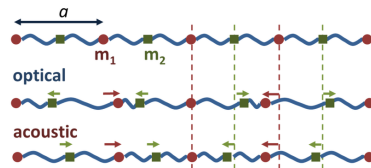


Figure 4.2: Acoustic and optical vibrations in a linear diatomic chain ([Wikipedia, 2013a]).

4.1.4 Normal modes of a three-dimensional lattice

In three dimensions, the harmonic potential is generalized and expressed in matrix notation as

$$U^{\text{harm}} = \frac{1}{2} \sum_{\mathbf{R}\mathbf{R}'} \mathbf{u}(\mathbf{R}) \mathbf{D}(\mathbf{R} - \mathbf{R}') \mathbf{u}(\mathbf{R}') \quad (4.14)$$

The matrix with matrix elements $D_{\mu\nu}$ itself has the important properties

$$D_{\mu\nu}(\mathbf{R} - \mathbf{R}') = D_{\nu\mu}(\mathbf{R}' - \mathbf{R}) \quad (4.15)$$

and

$$\sum_{\mathbf{R}} D_{\mu\nu}(\mathbf{R}) = 0. \quad (4.16)$$

The solutions for the equations of motion

$$M\ddot{\mathbf{u}}(\mathbf{R}) = - \sum_{\mathbf{R}'} \mathbf{D}(\mathbf{R} - \mathbf{R}') \mathbf{u}(\mathbf{R}') \quad (4.17)$$

shall be, like in Eq. (4.10), of the form

$$\mathbf{u}(\mathbf{R}, t) = \boldsymbol{\epsilon} e^{i(\mathbf{k}\mathbf{R} - \omega t)}. \quad (4.18)$$

$\boldsymbol{\epsilon}$ is a vector to be determined and with periodic boundary conditions

$$\mathbf{u}(\mathbf{R} + N_i \mathbf{a}_i) = \mathbf{u}(\mathbf{R}) \quad (4.19)$$

the wave vector is restricted to

$$\mathbf{k} = \frac{n_1}{N_1} \mathbf{b}_1 + \frac{n_2}{N_2} \mathbf{b}_2 + \frac{n_3}{N_3} \mathbf{b}_3 \quad (4.20)$$

in which $N_1, N_2, N_3, N = N_1 N_2 N_3$ and n_i are integer values. The reciprocal lattice vectors \mathbf{b}_j with corresponding lattice vectors \mathbf{a}_i have the property $\mathbf{a}_i \mathbf{b}_j = 2\pi \delta_{ij}$. Adding a reciprocal lattice vector \mathbf{K} of the primitive cell to \mathbf{k} does not change the atomic displacement because of

$$e^{i\mathbf{K}\mathbf{R}} \equiv 1. \quad (4.21)$$

Therefore there are only N distinct solutions for \mathbf{k} . Eqs. (4.17) and (4.18) lead to the eigenvalue problem

$$M\omega^2 \boldsymbol{\epsilon} = \tilde{\mathbf{D}}(\mathbf{k}) \boldsymbol{\epsilon} \quad (4.22)$$

where

$$\tilde{\mathbf{D}}(\mathbf{k}) = \sum_{\mathbf{R}} \mathbf{D}(\mathbf{R}) e^{-i\mathbf{k}\mathbf{R}} \quad (4.23)$$

is the *dynamical matrix*, $\boldsymbol{\epsilon}$ are eigenvectors. From Eq. (4.15) follows, that there are 3 real-valued eigenvectors $\boldsymbol{\epsilon}_j$ for every \mathbf{k} and therefore a total of $3N$ solutions. In a mono-atomic basis, there are now 3 acoustic branches, of which one is longitudinal and two are transverse.

When a multi-atomic basis is present, additional optical branches appear (Fig. 4.3). The number of normal modes is $3N$, where N is the number of atoms in the basis. Three of the modes are (one longitudinal and two transverse) acoustic and the remaining are (longitudinal or transverse) optical.

4.1.5 Energies and phonons

The normal modes described in the previous chapter can be transformed into Fourier space, in which the energy transport of the mode is assigned a corpuscular character with an defined frequency and *crystal momentum*.

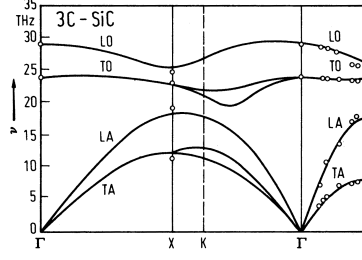


Figure 4.3: Acoustic and optical branches in β -SiC ([Kushwaha, 1982]).

As the ions are quantum particles, a quantization occurs and the allowed energy eigenvalues of each independent oscillator are given by $(n_{\mathbf{k}s} + \frac{1}{2}\hbar\omega_s(\mathbf{k}))$ with integer $n_{\mathbf{k}s}$. A summation over the branches $s = 1, 2, 3$ and every wave vector \mathbf{k} present in the crystal delivers the total energy

$$E = \sum_{\mathbf{k}s} (n_{\mathbf{k}s} + \frac{1}{2}\hbar\omega_s(\mathbf{k})). \quad (4.24)$$

The excitation number $n_{\mathbf{k}s}$ associated with the independent oscillators (normal modes) are usually referred to as *phonons*, similarly to the photons of electromagnetic waves.

Phonons are quasi-particles and with respect to the acoustic and optical modes there exist acoustic and optical phonons. The description with phonons is a more compact form than a formulation with wave vectors and branches and emissions and absorptions of quantized electromagnetic waves can be described by just summing up wave vectors.

4.2 Lattice dynamics and forces

The total energy of a crystal can be expressed in the harmonic approximation as a series

$$E_{\text{tot}} = E_{\text{tot}}^{(0)} + \sum_{a\kappa\alpha} \sum_{b\kappa'\beta} \frac{1}{2} \left(\frac{\partial^2 E_{\text{tot}}}{\partial u_{\kappa\alpha}^a \partial u_{\kappa'\beta}^b} \right) u_{\kappa\alpha}^a u_{\kappa'\beta}^b + \dots \quad (4.25)$$

truncated at $E^{(2)}$. The first order derivative term, $E^{(1)}$, is zero in equilibrium. $u_{\kappa\alpha}^a$ describes a displacement of atom κ of cell a in direction α . The second order term includes the matrix of interatomic force constants

$$C_{\kappa\alpha,\kappa'\beta}(a,b) = \left(\frac{\partial^2 E_{\text{tot}}}{\partial u_{\kappa\alpha}^a \partial u_{\kappa'\beta}^b} \right) \quad (4.26)$$

which leads to the force on a given atom

$$F_{\kappa\alpha}^{ab} = - \sum_{\kappa',\beta} C_{\kappa\alpha,\kappa'\beta}(a,b) u_{\kappa'\beta}^b. \quad (4.27)$$

The Fourier transform of Eq. (4.26) may be used to get the dynamical matrix (Eq. (4.23))

$$\tilde{D}_{\kappa\alpha,\kappa'\beta}(\mathbf{k}) = \tilde{C}_{\kappa\alpha,\kappa'\beta}(\mathbf{k}) / (M_{\kappa} M_{\kappa'})^{1/2} \quad (4.28)$$

which has a direct connection to the phonon frequencies $\omega_{m\mathbf{k}}$ and eigenvectors $\mathbf{e}_{m\mathbf{k}}(\kappa\alpha)$ of mode m :

$$\sum_{\kappa',\beta} \tilde{D}_{\kappa\alpha,\kappa'\beta}(\mathbf{k}) \mathbf{e}_{m\mathbf{k}}(\kappa',\beta) = \omega_{m\mathbf{k}}^2 \mathbf{e}_{m\mathbf{k}}(\kappa\alpha). \quad (4.29)$$

The energy contribution $E^{(2)}$ may be derived from *density function perturbation theory* (DFPT) or by using *finite differences*. The former method has the advantage over the latter, that no real-space calculations of the super-cell have to be performed. Also, on phonon calculations, DFPT may be used to get the *Born effective charges* ([Baroni et al., 2001]). A concise introduction to DFPT is given in the next section.

4.3 Density functional perturbation theory

Sections 4.3.1 and 4.3.2 are based on [Tulip, 2004], in which more details are available.

4.3.1 Perturbation theory

The *ansatz* of a perturbation theory in quantum mechanics is that a small perturbation to a system in equilibrium can be written as a power series in λ

$$X(\lambda) = X^{(0)} + \lambda X^{(1)} + \lambda^2 X^{(2)} + \dots \quad (4.30)$$

with expansion coefficients

$$X^{(n)} = \frac{1}{n!} \left. \frac{d^n X}{d\lambda^n} \right|_{\lambda=0}. \quad (4.31)$$

X is some physical quantity and λ is a (small) perturbing parameter which is zero at equilibrium.

Assuming a first order perturbation, all quantities of the Schrödinger equation

$$H|\psi\rangle = \epsilon|\psi\rangle \quad (4.32)$$

have to be expanded up to $X^{(1)}$:

$$H = H^{(0)} + \lambda H^{(1)}, \quad (4.33)$$

$$|\psi\rangle = |\psi^{(0)}\rangle + \lambda |\psi^{(1)}\rangle, \quad (4.34)$$

$$\epsilon = \epsilon^{(0)} + \lambda \epsilon^{(1)}. \quad (4.35)$$

Substituting Eqs. (4.33-4.35) in Eq. (4.32) leads to

$$(H^{(0)} + \lambda H^{(1)})(|\psi^{(0)}\rangle + \lambda |\psi^{(1)}\rangle) = (\epsilon^{(0)} + \lambda \epsilon^{(1)})(|\psi^{(0)}\rangle + \lambda |\psi^{(1)}\rangle). \quad (4.36)$$

Expanding Eq. (4.36) and comparing the coefficients of each power of λ (in this case just λ^1), a set of equations (Eqs. (4.37-4.38)) is yield.

Once the Schrödinger equation

$$H^{(0)}|\psi^{(0)}\rangle = \epsilon^{(0)}|\psi^{(0)}\rangle \quad (4.37)$$

for the unperturbed Hamiltonian $H^{(0)}$ is solved, the first-order equation

$$H^{(0)}|\psi^{(1)}\rangle + H^{(1)}|\psi^{(0)}\rangle = \epsilon^{(0)}|\psi^{(1)}\rangle + \epsilon^{(1)}|\psi^{(0)}\rangle \quad (4.38)$$

is used to yield $\epsilon^{(1)}$ and $|\psi^{(1)}\rangle$.

4.3.2 Perturbation of the Kohn-Sham potentials

In the density functional perturbation theory (DFPT), the Kohn-Sham orbitals are the starting point and with the *Sternheimer* equation ([Sternheimer and Foley, 1953], [Sternheimer, 1954], see Eq. (4.38))

$$(H_{\text{KS}}^{(0)} - \epsilon_n^{(0)})|\psi_n^{(1)}\rangle = -(H_{\text{KS}}^{(1)} - \epsilon_n^{(1)})|\psi_n^{(0)}\rangle \quad (4.39)$$

a variation in the orbitals is obtained. $H_{\text{KS}}^{(1)}$ is the first order perturbation of the Kohn-Sham potential:

$$H_{\text{KS}}^{(1)} = T^{(1)} + v_{\text{ext}}^{(1)}(\mathbf{r}) + e^2 \int \frac{n^{(1)}(\mathbf{r}')}{|\mathbf{r} - \mathbf{r}'|} d\mathbf{r}' + \int \frac{\delta v_{\text{xc}}}{\delta n(\mathbf{r}')} n^{(1)}(\mathbf{r}') d\mathbf{r}'.. \quad (4.40)$$

The first order energy is then given by

$$\epsilon_n^{(1)} = \langle \psi_n^{(0)} | H_{\text{KS}}^{(1)} | \psi_n^{(0)} \rangle \quad (4.41)$$

and the orbitals by

$$|\psi_n^{(1)}\rangle = \sum_{m \neq n} C_{nm}^{(1)} |\psi_m^{(0)}\rangle \quad (4.42)$$

in which the coefficients are

$$C_{nm}^{(1)} = \frac{\langle \psi_m^{(0)} | H_{\text{KS}}^{(1)} | \psi_n^{(0)} \rangle}{\epsilon_n^{(0)} - \epsilon_m^{(0)}}. \quad (4.43)$$

Together with the first order density perturbation

$$n^{(1)}(\mathbf{r}) = \sum_{n=1}^N \psi_n^{(0)*}(\mathbf{r}) \psi_n^{(1)}(\mathbf{r}) + \psi_n^{(1)*}(\mathbf{r}) \psi_n^{(0)}(\mathbf{r}), \quad (4.44)$$

equations 4.41-4.44 form a set of self-consistent equations.

4.4 Dynamical charges (Born effective charges)

When dealing with phonons and in order to calculate infrared intensities, it is required to pass over from static charges to dynamical charges. The dynamical charge tensor describes the coupling of phonons with the electric field resulting from the long-range character of the Coulomb potential in polar crystals.

As a phonon excites a molecular vibration, in the presence of dipoles (in general: a polar crystal) the dipole moment (in general: the polarization) changes. The definition of the dynamical charge is the linear order variation of the macroscopic polarization per unit cell in direction β , arising from a rigid displacement of the sublattice of atom κ in direction α , times the unit cell volume Ω_0 ([Ghosez et al., 1998]):

$$Z_{\kappa\alpha\beta}^* = \Omega_0 \frac{\partial \mathcal{P}_\beta}{\partial u_{\kappa\alpha}} \quad (4.45)$$

In crystals, the boundary conditions for the macroscopic electric field \mathcal{E} influence the polarization \mathcal{P} , and the dynamical charge has to be written more generally as

$$Z_{\kappa\alpha\beta}^* = \left. \frac{\partial \mathcal{P}_\beta}{\partial u_{\kappa\alpha}} \right|_{\mathcal{E}=0} + \Omega_0 \sum_j^3 \frac{\partial \mathcal{P}_\beta}{\partial \mathcal{E}_j} \frac{\partial \mathcal{E}_j}{\partial u_{\kappa\alpha}} \quad (4.46)$$

From Eq. (4.46), historically, different charges were defined, one of them is the *Born effective charge* or *transverse charge* ([Born, 1988]):

$$Z_{\kappa\alpha\beta}^* = \left. \frac{\partial \mathcal{P}_\beta}{\partial u_{\kappa\alpha}} \right|_{\mathcal{E}=0}, \quad (4.47)$$

which assumes a zero macroscopic electric field.

4.5 Infrared spectra

In infrared (IR) spectroscopy, electromagnetic waves (photons) are absorbed by the specific vibrational modes of a molecule in the range between 650 cm^{-1} and 4000 cm^{-1} . Translational modes can be found down to the far-infrared range of about 50 cm^{-1} . The frequency of the dipole oscillations of a molecule is the same as that of the vibration of the ions and can be expressed in terms of the frequencies of the normal modes in the harmonic approximation. If the energy (frequency) of a normal mode matches that of the incident wave, the energy (a photon) may be absorbed and a normal mode excited (a phonon generated). For a polar crystal, the same mechanism applies. A comparison of theoretical with experimental values is done via the oscillator strength of mode m (which is the first-order infrared intensity) ([Giannozzi and Baroni, 1994])

$$I_m^{\text{IR}} \propto \sum_{\alpha} \left| \sum_{\kappa\beta} \frac{\partial \boldsymbol{\mu}_{\alpha}}{\partial u_{\kappa\beta}} \mathbf{e}_{m\mathbf{k}}(\kappa\alpha) \right|^2. \quad (4.48)$$

$\boldsymbol{\mu}_{\alpha}$ is the dipole moment, $u_{\kappa\beta}$ the displacement of atom κ in cell α and $\mathbf{e}_{m\mathbf{k}}(\kappa\alpha)$ the m th normal-mode eigenvector.

This can be generalized for a macroscopic polarization and expressed using the definition of the Born effective charge (Eq. (4.47)) ([Giannozzi and Baroni, 1994]):

$$I_m^{\text{IR}} \propto \sum_{\alpha} \left| \sum_{\kappa\beta} Z_{\kappa,\alpha\beta}^* \mathbf{e}_{m\mathbf{k}}(\kappa\alpha) \right|^2. \quad (4.49)$$

Chapter 5

Computational setup

All *ab initio* calculations were done with the Vienna Ab initio Simulation Package (VASP), which uses pseudo-potentials or the projector-augmented wave (PAW) method and a plane wave basis set for performing ab-initio quantum-mechanical molecular dynamics simulations. Further literature and seminal VASP papers include: [Kresse and Hafner, 1993], [Kresse and Furthmüller, 1996], [Blöchl, 1994] and [Kresse, 1999]. The phases were taken from various sources: [Santra, 2011], [Geiger, 2011], [Hirsch and Ojamäe, 2004], [Londono et al., 1993, data set IX2], [Salzmann, 2006], [Salzmann et al., 2009], [Knight and Singer, 2008]

5.1 Relaxation and volume scan

The equilibrium properties of the structure were found by performing a volume scan for the energy minimum at the PBE level of theory. PBE stands for *Perdew-Burke-Ernzerhof* and is a widely used generalized gradient approximation (GGA) to the exchange-correlation functional of the Kohn-Sham scheme ([Perdew et al., 1996]). At each volume, the cell shape and the atoms were relaxed keeping only the volume fixed (ISIF=4). To obtain the equilibrium values, the resulting energy-volume curve of each structure was fitted using a 3rd order Birch-Murnaghan equation of state

$$E(V) = E_0 + \frac{9V_0B_0}{16} \left\{ \left[\left(\frac{V_0}{V} \right)^{\frac{2}{3}} - 1 \right]^3 B'_0 + \left[\left(\frac{V_0}{V} \right)^{\frac{2}{3}} - 1 \right]^2 \left[6 - 4 \left(\frac{V_0}{V} \right)^{\frac{2}{3}} \right] \right\}. \quad (5.1)$$

For the relaxation, a conjugate-gradient algorithm (IBRION=2) was used. The energy cutoff for the plane wave basis set (ENCUT) was set to 800 eV. PAW/PBE potentials were used throughout the whole procedure. For the k-point sampling, a Gamma centered Monkhorst-Pack scheme with $6 \times 6 \times 6$ points was used. At the equilibrium volume, an additional relaxation was performed to refine the structural properties. At each volume, the partial occupancies were finally obtained with a tetrahedron method with Blöchl corrections (ISMEAR=-5) and without relaxation (IBRION=-1). This procedure provides accurate total energy values.

The complete INCAR file of a volume scan calculation reads:
ISIF=4

```

ENCUT=800
ISMear=0
IBRION=2
NSW=25
NELMIN=6
EDIFF=1E-6
EDIFFG=-0.01

```

5.2 RPA setup

With the PBE relaxed structures as input, a volume scan was performed at the RPA level. The energy-volume curve again was fitted with the BM EOS Eq. (5.1). The total energy of the system is then computed as the sum of the RPA energy plus the exchange energy. Two different methods were carried out:

- The RPA correlation energy was combined with the exact exchange energy (EXX) from Hartree-Fock calculations.
- RPA was combined with a self-consistent HF calculation (denoted as SCHF in this work).

The exact exchange energy is evaluated using PBE orbitals while in the SCHF method, self-consistently relaxed HF orbitals are used. An energy cutoff of 450eV was set in the RPA calculations. For both methods, `POTCAR` versions with harder than the normal PAW/PBE potentials were used. A Gamma centered Monkhorst-Pack scheme was taken to sample the k-point mesh, while the maximum number of volume points was dependent on the convergence behavior of the particular ice phase.

The RPA setup for RPA+EXX follows the 4 steps procedure of the general recipe to calculate ACFDT-RPA total energies from the VASP guide:

1. All occupied orbitals of the DFT-Hamiltonian are calculated:

```

ENCUT=450
GGA = PE
EDIFF = 1E-6
ISMear = 0

```

2. The exact exchange energy is calculated:

```

ENCUT=450
ALGO = EIGENVAL ; NELM = 1
LWAVE=.FALSE.
LHFCALC = .TRUE. ; AEXX = 1.0 ; ALDAC = 0.0 ; AGGAC = 0.0
HFRcut=-1
ISMear = 0

```

3. The exact diagonalization of the DFT Hamiltonian is performed:

```

ENCUT=450
NBANDS = (maximum number of plane-waves)
ALGO = S

```

```

NELM = 1
GGA = PE
EDIFF = 1E-6
LOPTICS = .TRUE.
ISMear = 0

```

4. Finally, the ACFDT-RPA correlation energy is calculated:

```

ENCUT=450
NBANDS = (maximum number of plane-waves)
ALGO = ACFDT
NOMEGA = 16 ; OMEGATL = 1000
ISMear = -1 ; SIGMA = 0.1

```

The self-consistent Hartree-Fock calculation consists of the first step from RPA+EXX followed by the HF part:

```

ISTART=1
ENCUT=450
ISMear = 0
LHFCALC = .TRUE. ; AEXX = 1.0 ; ALDAC = 0.0 ; AGGAC = 0.0
ALGO = All ; TIME = 0.4
PRECFOCK = Normal
LWAVE = .FALSE.

```

In the hydrogen bond, the Pauli repulsion has a strong effect. A self-consistent HF (SCHF) calculation yields less Pauli repulsion than the exact-exchange (EXX) calculation from DFT orbitals (see Chap. 3.2), which results in a stronger binding energy for SCHF. In the two variants (self-consistent and EXX), with which the exchange energy of the solids and the single H₂O molecule has been evaluated, this has the effect, that the energy difference between the molecule and the bulk is larger in the self-consistent calculations.

5.3 Infrared spectra

For particular structures, the infrared spectrum was computed. The dynamical matrix and the Born effective charges were determined using density functional perturbation theory with use of symmetry operations to speed up calculations IBRION=8. An energy cutoff of 1000 eV was set for the PBE potential.

Additionally to the spectra from PBE, the Hessian matrix was calculated by using finite differences IBRION=6 with an optPBE-vdW functional ([Klimeš et al., 2010]). An energy cutoff of 1000 eV was used again. To obtain the infrared intensities from this setup, the vibrational modes from the vdW setup were combined with the Born effective charges from the linear response calculation.

The peaks were broadened by a Lorentzian distribution

$$F(f) = \frac{1}{\pi} \text{Im} \frac{1}{f - f_0 + i\eta} \quad (5.2)$$

which reflects the natural broadening due to finite lifetimes of excited states. η specifies the half-width at half-maximum.

The complete INCAR file for an IR calculation with linear response reads:

```
ENCUT=1000
LEPSILON= .TRUE.
ISIF=4
ISMear=0
IBRION=8
EDIFF=1E-8
NELMIN=6
```

The vdW calculations were performed with the following INCAR file:

```
ENCUT=1000
LEPSILON= .TRUE.
IBRION=6
EDIFF=1E-8
ISMear=0
NELMIN=6
LUSE_VDW = .TRUE.
AGGAC = 0.0000
GGA = OR
```

For all IR calculations, the VASP PBE potentials PAW_PBE H_h 06Feb2004 and PAW_PBE O_h 06Feb2004 were used. The k-point sampling was done with a Gamma centered Monkhorst-Pack scheme with $2 \times 2 \times 2$ points.

Chapter 6

PBE and RPA results

In this chapter, equilibrium energies and volumes from DFT and RPA calculations are presented. Furthermore, the bulk modulus B and its first pressure derivative B' derived from the BM EOS are shown. Lattice parameters of the VASP optimized unit cells are given. All values are compared to experimental and theoretical values if available.

The energy convergence is expected to be better than 1 meV for PBE and RPA calculations. The volume however, strongly varies with energy variations and thus, a volume error of $\pm 0.25 \text{ \AA}^3$ has to be expected.

If available, the energy difference to ice I_h is given in the results tables. If not otherwise mentioned, it is related to the I_h energy of the same work.

Note, that the volume results show a volume shift between RPA+EXX and RPA+SCHF over the entire pressure range and thus it seems reasonable to compare the volumes relative to the hexagonal phase (Fig. 6.34).

6.1 Phases investigated

Table 6.1 and Fig. 6.1 show an overview of the phases which have been investigated in this work. Proton ordered phases were preferred over their disordered counterparts, because they can be described with smaller unit cells. A comprehensive overview of all known ice phases is given in [Chaplin, 2012]. Corresponding space groups can be found in [College, 1999].

phase	space group	cell	cell ¹	mol. ¹
I _h	P6 ₃ /mmc (#194)	hexagonal	simple monoclinic	12
I _c (a)	I4 ₁ md (#109)	tetragonal	body c. tetragonal	2
I _c (b)	Pna2 ₁ (#33)	orthorhombic	simple orthorhombic	4
I _c (c)	P4 ₁ (#76)	tetragonal	simple tetragonal	8
I _c (d)	P4 ₁ 2 ₁ 2 (#92)	tetragonal	simple tetragonal	4
XI Cmc2 ₁	Cmc2 ₁ (#36)	orthogonal	base c. orthorhombic	4
XI Pna2 ₁	Pna2 ₁ (#33)	orthorhombic	simple orthorhombic	8
IX	P4 ₁ 2 ₁ 2 (#92)	tetragonal	simple tetragonal	12
II	R $\bar{3}$ (#148)	rhombohedral	trigonal (rhombohedral)	12
XIII	P2 ₁ /a (#14) ^a	monoclinic	simple monoclinic	28
XV	P1 (#1) ^b	triclinic	triclinic	10
VIII	I4 ₁ /amd (#141)	tetragonal	body c. tetragonal	4
X	Pn $\bar{3}$ m (#224)	cubic	simple cubic	2

Table 6.1: Phases investigated. The Bravais lattice of the VASP optimized cell and the number of molecules per unit cell are given by cell¹ and mol.¹.

^aRef.[Salzmann et al., 2006], ^bRef.[Salzmann et al., 2009].

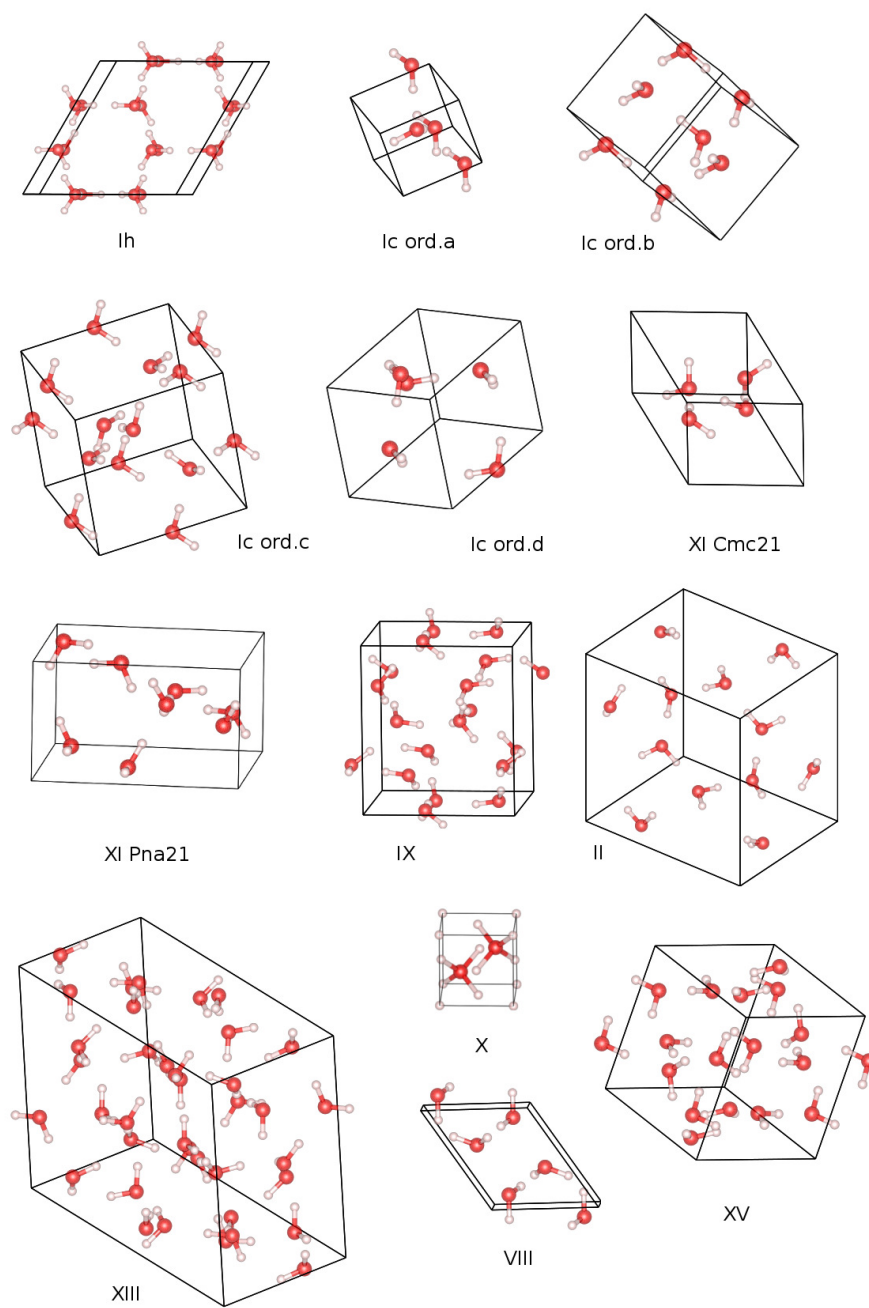


Figure 6.1: Structures investigated.

6.2 Ice crystal energy convergence

At the PBE level, a $6 \times 6 \times 6$ k-points mesh was sufficient for all phases to give a converged total energy.

At the RPA level, however, the energy components behave differently. The RPA correlation energy converges relatively fast with increasing k-points, so on some phases a $3 \times 3 \times 3$ k-points mesh was sufficient to get an energy with accuracy of few tenth of a meV. The exact exchange energy requires a denser k-point mesh than that of the RPA energy calculation. The error made in the HF calculations decreases by $1/(\text{number of k-points})^3$ and an extrapolation leads to the energy of infinite k-points for both, EXX and SCHF energy. An example for a k-points extrapolation is shown in Fig. 6.2.

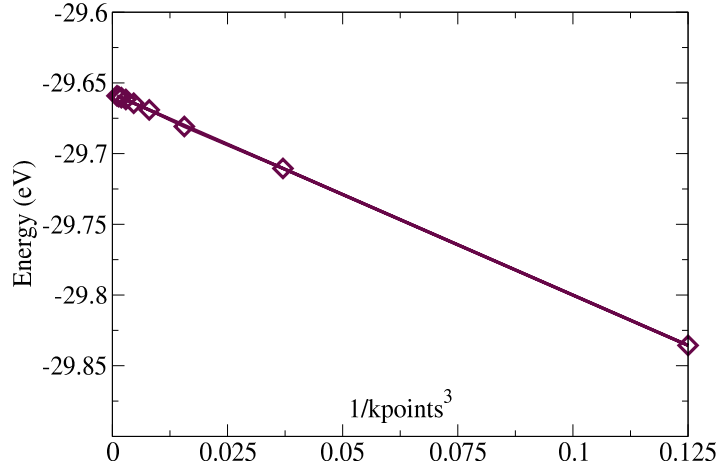


Figure 6.2: Example of a k-points extrapolation.

6.3 H₂O molecule energy convergence

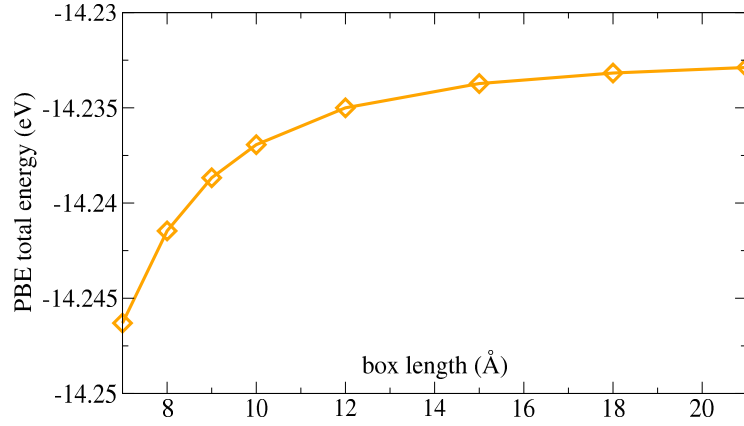
In order to get the cohesive energy of the ice phases, the energy of a single H₂O molecule has to be subtracted from the total energy of a crystal molecule:

$$E_{\text{coh}} = E_{\text{ice}}/N - E_{\text{H}_2\text{O}}. \quad (6.1)$$

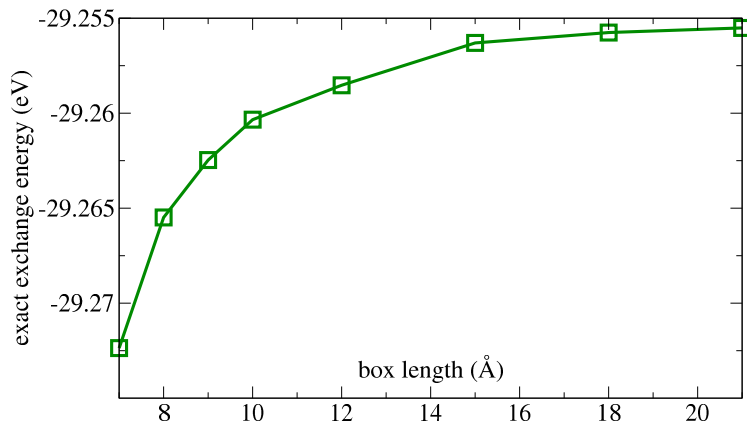
The molecule was relaxed at the PBE level at different box volumes and $6 \times 6 \times 6$ k-points. From the relaxed structures, energies have been calculated. Since at the RPA level, the correlation energy is more expensive to obtain than the exchange energy, they were treated separately. The RPA correlation energy was taken at a volume of $7 \times 7 \times 7 \text{ \AA}^3$ and $3 \times 3 \times 3$ k-points. The exchange energies were extrapolated to infinite k-points at each volume point taken from PBE calculations. Fig. 6.3 shows the energy convergence with respect to box length of the PBE relaxed structures as well as the EXX and SCHF exchange energies.

The RPA energy contribution for the H₂O molecule was found to be -12.426 eV . EXX and SCHF energy were estimated to -29.254 eV and -29.479 eV respectively.

a) PBE total energy convergence



b) EXX convergence



c) SCHF exchange energy convergence

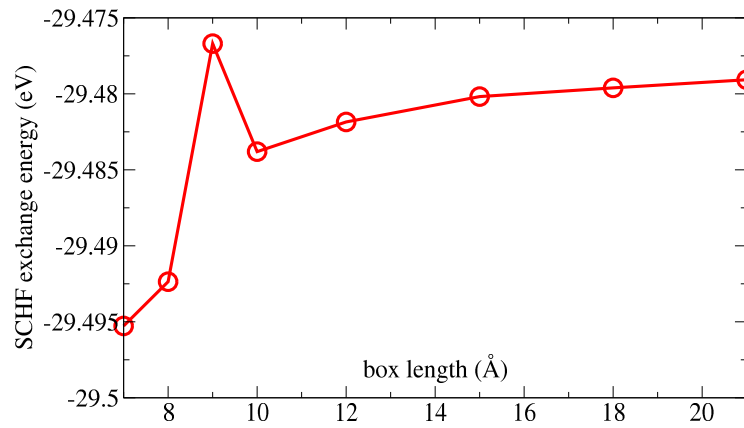


Figure 6.3: Energy convergence of the H₂O molecule with respect to the box length for the PBE total energy as well as the EXX and SCHF exchange energies.

6.4 Ice I_h

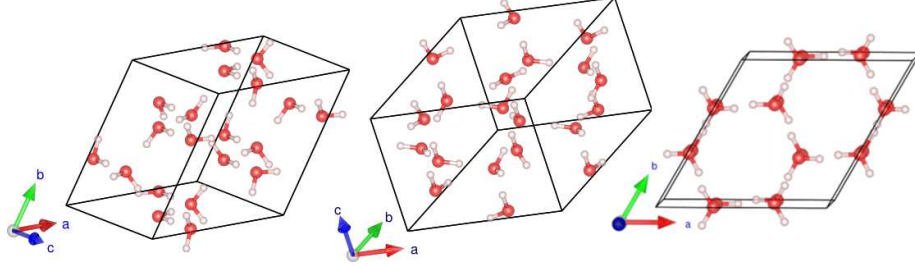


Figure 6.4: Ice I_h structure.

Hexagonal ice I_h is the structure, from which snow and most natural ice is formed. It has symmetry D_{6h} , the space group is $P6_3/mmc$ (#194), and there are 4 molecules in the unit cell. The water molecules form hexagonal rings, which together in a plane form sheets. The sheets are ABABAB-stacked so that every third sheet is placed directly over the first. The proton structure is disordered. An informative depiction in this respect can be found e.g. in [Fukazawa et al., 2005]. Because of the disorder, a compromise has to be made for the size of the super-cell. It has been shown in [Pan et al., 2010] that the ground state energy of the 12 molecule cell suggested by [Hamann, 1997] and chosen in this work (see Fig. 6.4), is in the range of about 3 meV of the one corresponding to a bigger 96 molecule cell which in turn delivers a good representation of the randomness of the protons.

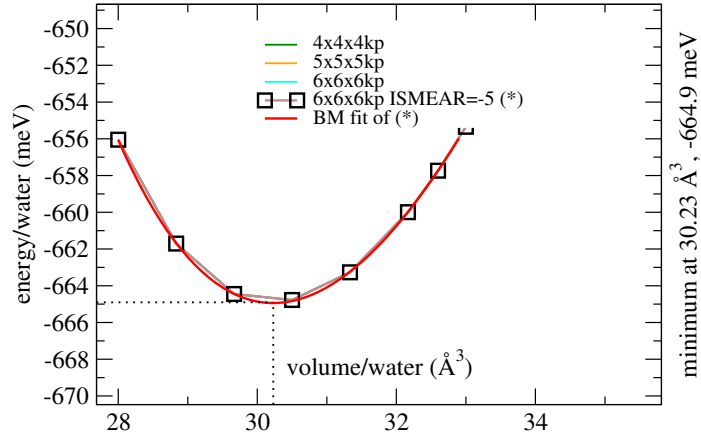
X-ray powder diffraction at 10 – 265 K was performed by [Röttger et al., 2012], which reported lattice parameters $a = 4.4969(2)$ Å and $c = 7.3211(3)$ Å for H_2O as well as $a = 4.4982(2)$ Å and $c = 7.3233(6)$ Å for D_2O extrapolated to 0 K for a unit cell described by 4 molecules. An extrapolation of the volume to 0 K leads to unit cell volumes of $32.0537(40)$ Å³ for H_2O and $32.0829(38)$ Å³ for D_2O , respectively. [Petrenko, 1999] reports cell dimensions of $a = 4.518$ Å and $c = 7.356$ Å and a volume of 32.50 Å³ at 253 K. Table 6.2 summarizes structural results from the PBE calculation as well as experimental values.

The cohesive energy of ice I_h was measured and extrapolated to zero pressure and temperature to yield -610 meV (-58.82 kJ/mol) in [Whalley, 1984]. There are several experimental bulk moduli given in [Hobbs, 1974], ranging from 8.72

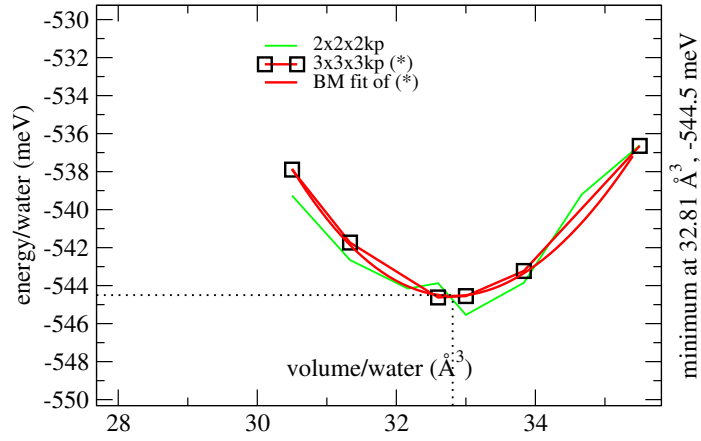
	a (Å)	c (Å)	c/a
PBE	4.4003	7.2008	1.6364
Expt. ^a	4.4969	7.3211	1.6280
Expt. ^b	4.518	7.356	1.628
MC/TIP4P ^c	4.490	7.318	1.630
MC/NvdE ^d	4.441(1)	7.248(1)	1.6321(4)

Table 6.2: Structural results for ice I_h , ^aRef.[Röttger et al., 2012] extrapolated to 0 K, ^bRef.[Petrenko, 1999], ^cRef.[Vega et al., 2005]: MC simulation with a TIP4P model at 250 K and zero pressure, ^dRef.[Rick, 2005]: MC simulation with a NvdE model ([Nada and van der Eerden, 2003]) at 25 K.

a) Ice I_h , PBE



b) Ice I_h , RPA+EXX



c) Ice I_h , RPA+SCHF

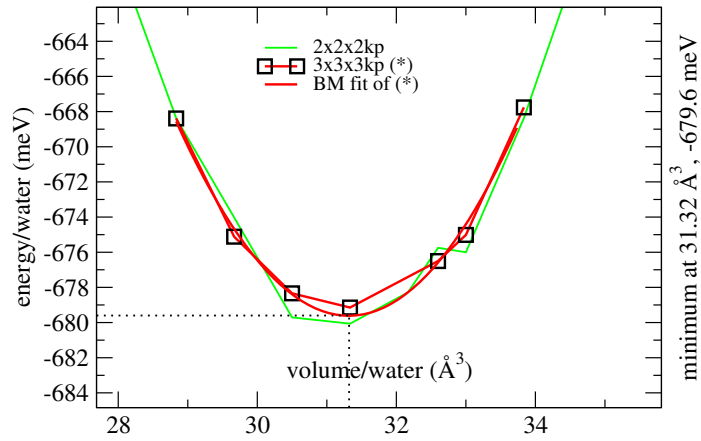


Figure 6.5: Ice I_h - PBE, RPA+EXX and RPA+SCHF energy-volume curves.

	E (meV)	V (\AA^3)	B (GPa)	B'
PBE	-665	30.23	14.65	5.58
RPA+EXX	-545	32.81	12.39	1.61
RPA+SCHF	-680	31.31	18.43	-1.29
Expt.	-610 ^a	32.05 ^b	8.72...11.3 ^c	
Expt.		32.50 ^d	10.9 ^{ac}	
DMC ^e	-605 ± 5	31.69 ± 0.01	18.3 ± 0.1	
FHI-aims/PBE ^e	-636	30.76		
FHI-aims/PBE0+vdW ^{TS} _e	-672	29.88		
PBE		31.82 ^f		
MC TIP4P/Ice ^g	-714	31.87		
MC TIP4P/2005 ^g	-653	31.33		
Quickstep/PBE ^h	-703 ± 2			

Table 6.3: Results for ice I_h . Cohesive energy and equilibrium volume are per molecule. ^aRef.[Whalley, 1984] at zero pressure and temperature, ^bRef.[Röttger et al., 2012], ^cRef.[Hobbs, 1974] (see text), ^dRef.[Petrenko, 1999] at 253 K, ^eRef.[Santra et al., 2011] [Santra et al., 2013]: PBE and PBE0+vdW^{TS} potential calculations with the FHI-aims software, Diffusion Quantum Monte Carlo simulations with the CASINO software package, ^fRef.[Hamann, 1997], ^gRef.[Aragones et al., 2007] at 0 K and zero pressure calculated with TIP4P/Ice and TIP4P/2005 within a Monte Carlo simulation, ^hRef.[Pan et al., 2008] Fig. 1.: PBE simulation performed with the Quickstep software package.

to 11.3 GPa. The value of 10.9 GPa, which [Whalley, 1984] referenced to [Hobbs, 1974], could not be retraced. It is overestimated by 20 – 80 %. Table 6.3 summarizes our obtained theoretical values for the total energy, volume, bulk modulus and its first derivative, and compares them with the corresponding experimental and previously calculated values available in literature. Fig. 6.5 shows the energy-volume curves of the PBE and RPA volume scans.

With $2 \times 2 \times 2$ k-points the energy-volume curve is not very smooth, however it improves substantially with $3 \times 3 \times 3$ k-points. Even then accurate estimates for B and B' are difficult to obtain.

PBE yields a reasonable, about 7 % too small volume (30.23 \AA^3). With vdW corrections, the PBE0+vdW^{TS} potential yields an even smaller volume of 29.88 \AA^3 . RPA+EXX and RPA+SCHF show well fitting lattice constants, one overestimating (32.81 \AA^3), one underestimating (31.31 \AA^3) the experimental volumes (32.05 and 32.50 \AA^3). Most likely, SCHF overcontracts the orbitals, reducing the Pauli repulsion too much. The volume shift between RPA+EXX and RPA-SCHF calculations can be seen over the entire pressure range. RPA+SCHF volume is in very good agreement with DMC, also the volumes of MC simulations go well with DMC and experiments.

There might be something odd with the PBE functional, maybe an overestimation of the hydrogen bond. However, it is known, that, depending on the basis set, an overestimation of the energy by about 30 – 100 meV occurs with PBE ([Santra et al., 2013]). Relative to DMC and the experimental result of [Whalley, 1984], our results show an overestimation of about 60 meV.

6.5 Ice XI Cmc2₁

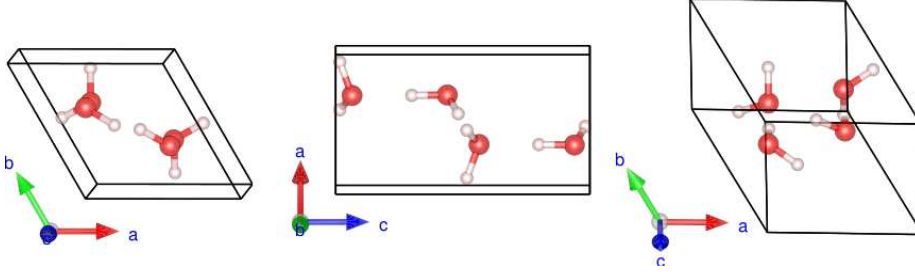


Figure 6.6: Ice XI Cmc2₁ structure.

There are 16 commonly considered possibilities for the protons of the proton-disordered ice I_h to order ([Hirsch and Ojamäe, 2004]). The most stable ([Jackson et al., 1997] [Howe and Whitworth, 1989]) has space group Cmc2₁ (#36) which is a subgroup of P6₃/mmc (#194). It has 4 molecules ([Rick, 2005]) in the orthorhombic unit cell (Fig. 6.6) and is called ice XI or XI_h. It is ferroelectric. An informative depiction of the proton ordering of ice XI and I_h can be found in [Fukazawa et al., 2005].

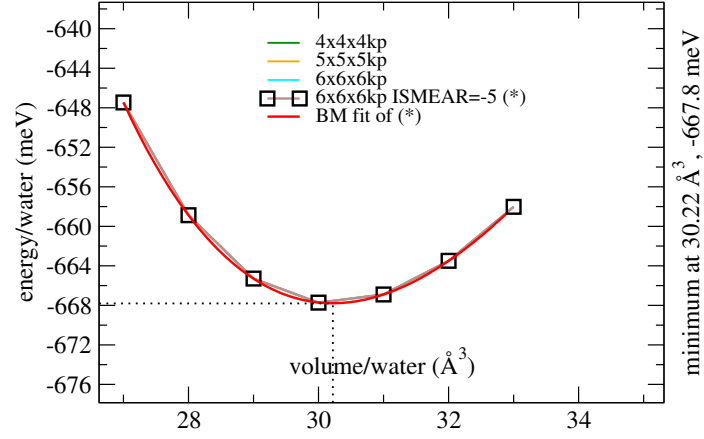
In experiments, KOH-doped (or KOD with D₂O) ice I_h forms to ice XI below about 72 K. It transforms very slowly ([Johari, 1998]), and measurements in [Howe and Whitworth, 1989], [Leadbetter et al., 1985] and [Jackson et al., 1997], were supposed to consist of a mixture of ice I_h and XI ([Fukazawa et al., 2005]). The portion of I_h in the XI phase is not entirely clear, but in [Li et al., 1995] experimentators waited “for 60h to allow a significant amount of transformation”. [Howe and Whitworth, 1989] waited 12 days and estimated, that 57 % must have been transformed from I_h to XI.

Lattice parameters have been measured in [Leadbetter et al., 1985] by neutron powder diffraction on KOD-doped D₂O at 5 K to be $a = 4.5019(5)$ Å, $b = 7.7978(8)$ Å and $c = 7.3280(2)$ Å. Also neutron powder diffraction yielded ([Howe and Whitworth, 1989]) $a = 4.5026(3)$ Å, $b = 7.7803(6)$ Å and $c = 7.2884(8)$ Å at 10 K. [Line and Whitworth, 1996] found lattice parameters $a = 4.465(3)$ Å, $b = 7.859(4)$ Å and $c = 7.292(2)$ Å at 5 K. Based on the lattice parameters, the volumes per water molecule are 32.156 Å³ (19.365 cm³/mol) ([Leadbetter et al., 1985]), 31.916 Å³ (19.220 cm³/mol) ([Howe and Whitworth, 1989]) and 31.985 Å³ (19.262 cm³/mol) ([Line and Whitworth, 1996]). Table 6.4 compares structural data from the PBE calculation with literature values.

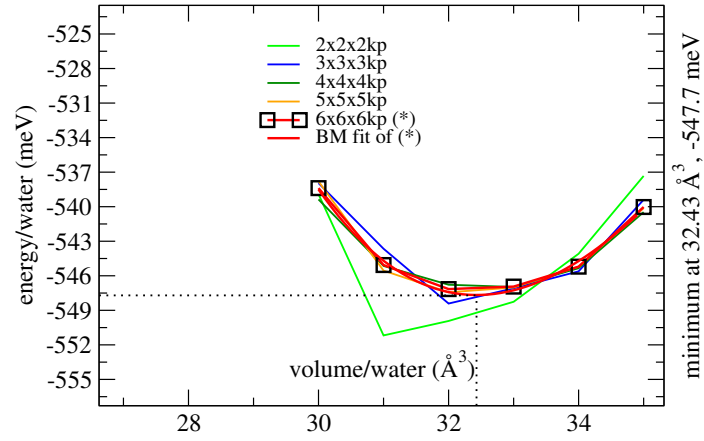
Table 6.5 summarizes energy, volume and the bulk modulus. Fig. 6.7 shows the energy-volume curves of the PBE and RPA volume scans. We note that k-point convergence is slow for RPA, which is mainly a result of the small energy scales considered here (10 meV). Smooth energy curves are only obtained using $6 \times 6 \times 6$ k-points for these small unit cells.

Three independent experiments show volumes of about 32 Å³. PBE is underestimating (30.22 Å³) this volume, but RPA+EXX (+1.3 %) and RPA+SCHF (−3 %) are in good agreement. The optPBE-vdW volume (−1.3 %) is in very good agreement and DMC underestimates the volume by about the same amount as RPA+SCHF. The results on this proton ordered form of the proton disordered hexagonal ice I_h essentially show the same behavior as the disordered phase.

a) Ice XI Cmc2₁, PBE



b) Ice XI Cmc2₁, RPA+EXX



c) Ice XI Cmc2₁, RPA+SCHF

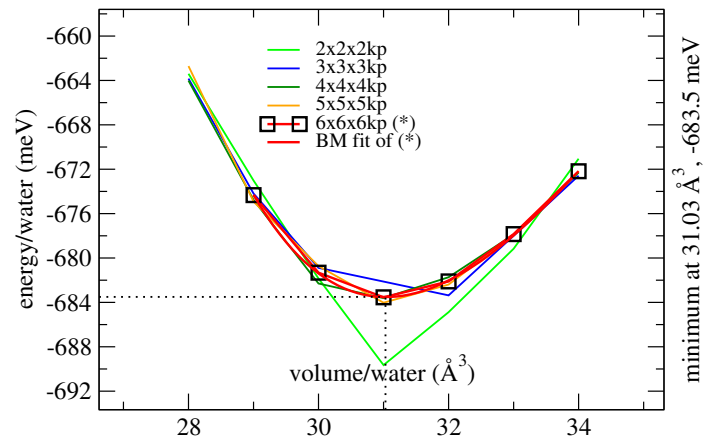


Figure 6.7: Ice XI Cmc2₁ - PBE, RPA+EXX and RPA+SCHF energy-volume curves.

	a (Å)	b (Å)	c (Å)
PBE	4.4018	7.6337	7.1917
Expt. ^a	4.5019(5)	7.7978(8)	7.3280(2)
Expt. ^b	4.5026(3)	7.7803(6)	7.2884(8)
Expt. ^c	4.465(3)	7.859(4)	7.292(2)
HF ^d	4.50	7.80	7.33
CASTEP/PW91 ^e	4.380	7.617	7.207

Table 6.4: Structural results for ice XI Cmc2₁, ^aRef.[Leadbetter et al., 1985], ^bRef.[Howe and Whitworth, 1989], ^cRef.[Line and Whitworth, 1996], ^dRef.[Pisani et al., 1996]: Hartree-Fock calculation, ^eRef.[Hirsch and Ojamäe, 2004]: DFT calculation with a PW91 functional performed with the software package CASTEP.

	E (meV)	V (Å ³)	B (GPa)	B'
PBE	−668 (−3)	30.22	14.83	5.62
RPA+EXX	−548 (−3)	32.43	13.74	5.07
RPA+SCHF	−684 (−4)	31.03	17.66	9.14
Expt. ^a		32.156		
Expt. ^b		31.916		
Expt. ^c		31.985		
optPBE-vdW ^d	−678	31.58		
DMC ^d	−599 ± 2	31.18 ± 0.22		
VASP/PBE ^d	−669			
PBE ^e	−663	30.50	14.60	5.7
vdW-DF2 ^e	−649	33.23	12.59	5.2
Quickstep/PBE ^f	−708(−5)			

Table 6.5: Results for ice XI Cmc2₁. Cohesive energy and equilibrium volume are per molecule, the energy relative to I_h, if available, is written in parentheses. ^aRef.[Leadbetter et al., 1985], ^bRef.[Howe and Whitworth, 1989], ^cRef.[Line and Whitworth, 1996], ^dRef.[Raza et al., 2011], ^eRef.[Murray and Galli, 2012], ^fRef.[Pan et al., 2008] Fig. 1.

6.6 Ice XI Pna2₁

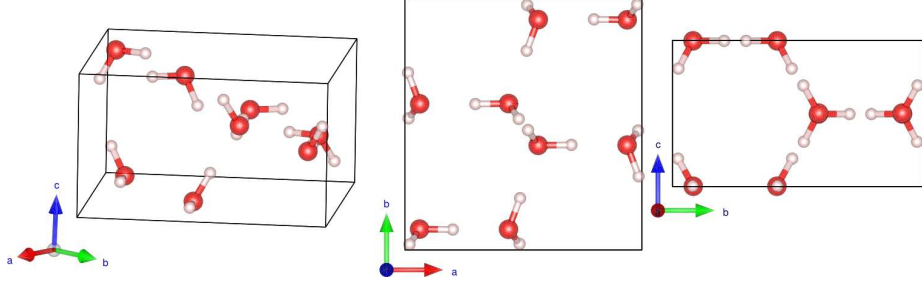


Figure 6.8: Ice XI Pna2₁ structure.

Besides the most stable ice XI Cmc2₁, the second most stable - out of the 16 possible - proton-ordering configurations of hexagonal ice I_h has space group Pna2₁ (#33) and 8 molecules in the orthorhombic unit cell ([Davidson and Morokuma, 1984], [Rick, 2005]) (Fig. 6.8). It is anti-ferroelectric and was proposed as the most stable proton-ordered hexagonal ice earlier in [Davidson and Morokuma, 1984].

Table 6.6 compares structural data from the PBE calculation with literature values.

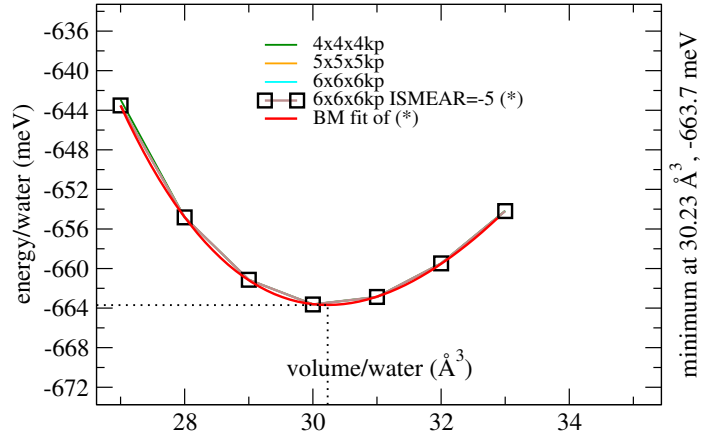
To our knowledge there is no experimental structural or enthalpy data available specifically for XI Pna2₁. Computational calculations (Table 6.7) reported the energy very close to that of ice XI Cmc2₁. Fig. 6.9 shows the energy-volume curves of the PBE and RPA volume scans.

Based on the volumes of ices I_h, I_c and XI Cmc2₁ the experimental volume of ice XI Pna2₁ can be assumed to be about 32 Å³. PBE is underestimating this by -5.5 %. RPA+EXX (+2.4 %) and RPA+SCHF (-1.9 %) are in better agreement with the hypothetical volume. The results on this proton ordered form of the proton disordered hexagonal ice I_h essentially show the same behavior as the disordered phase and probably all arguments apply here as well.

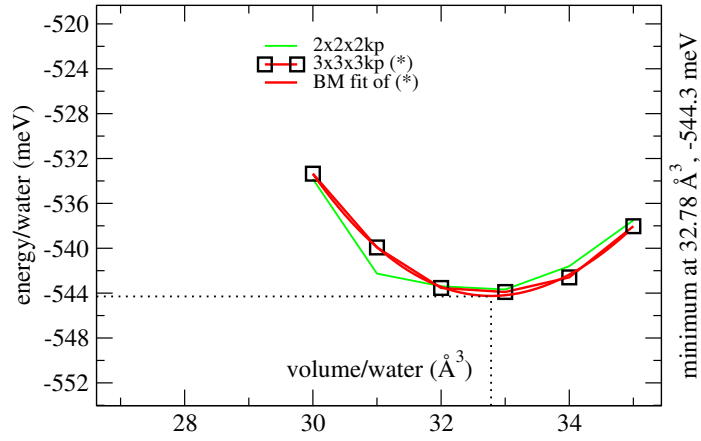
	a (Å)	b (Å)	c (Å)
PBE	4.4275	7.5974	7.1871
HF ^a	4.40	7.90	7.33
CASTEP/PW91 ^b	4.390	7.657	7.190

Table 6.6: Structural results for ice XI Pna2₁, ^aRef.[Pisani et al., 1996], ^bRef.[Hirsch and Ojamäe, 2004].

a) Ice XI Pna2₁, PBE



b) Ice XI Pna2₁, RPA+EXX



c) Ice XI Pna2₁, RPA+SCHF

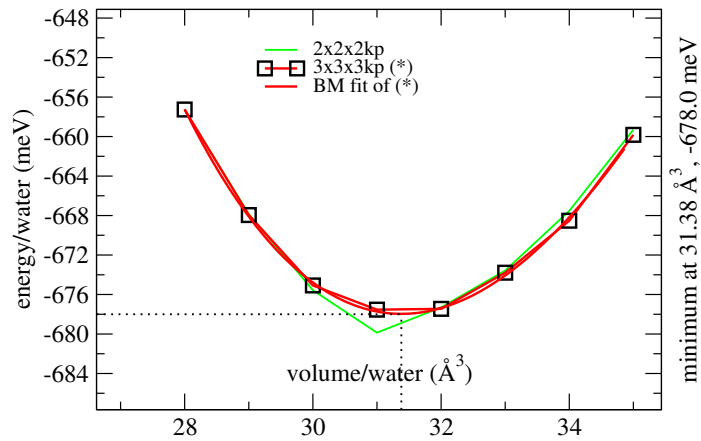


Figure 6.9: Ice XI Pna2₁ - PBE, RPA+EXX and RPA+SCHF energy-volume curves.

	E (meV)	V (\AA^3)	B (GPa)	B'
PBE	-664 (1)	30.23	14.58	5.63
RPA+EXX	-544 (0)	32.78	13.84	1.46
RPA+SCHF	-678 (2)	31.38	15.88	2.74
VASP/PBE ^a	-664			
CASTEP/PW91 ^b	-698	30.211		
Quickstep/PBE ^c	-707(-4)			

Table 6.7: Results for ice XI Pna2₁. Cohesive energy and equilibrium volume are per molecule, the energy relative to I_h , if available, is written in parentheses. ^aRef.[Raza et al., 2011], ^bRef.[Hirsch and Ojamäe, 2004], ^cRef.[Pan et al., 2008, Fig. 1].

6.7 Ice I_c

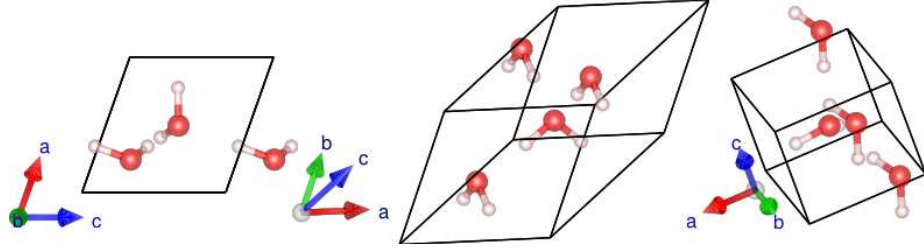


Figure 6.10: Ice I_c (ord. a) structure.

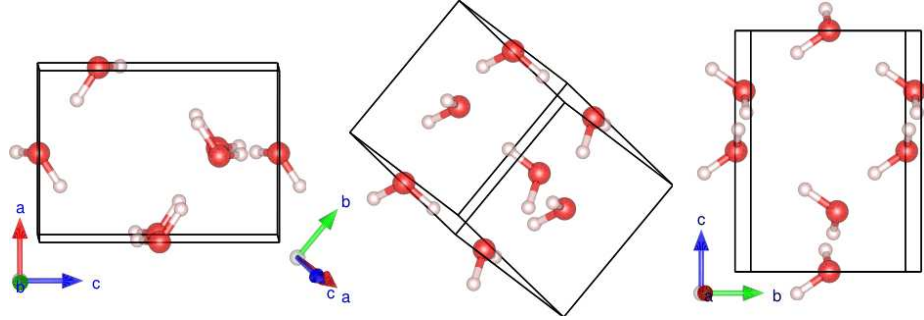


Figure 6.11: Ice I_c (ord. b) structure.

The, with respect to ice I_h , meta-stable cubic ice I_c may be formed artificially at temperatures between about 130 K and 220 K and can naturally be found in the upper atmosphere ([Murray et al., 2005] [Murray and Bertram, 2006] [Murray, 2008]). Above 240 K, ice I_c converts to ice I_h . There has been success in preparing phases of ice with a major portion of cubic ice (e.g. [Murray and Bertram, 2006]) but not a pure phase so far. The proton disordered ice I_c has a face centered cubic lattice, the space group of an 8 molecule cubic cell is $Fd\bar{3}m$ (#227). In a commonly considered alternative supercell, there are 11 different proton configurations possible ([Raza et al., 2011]). Out of them, four

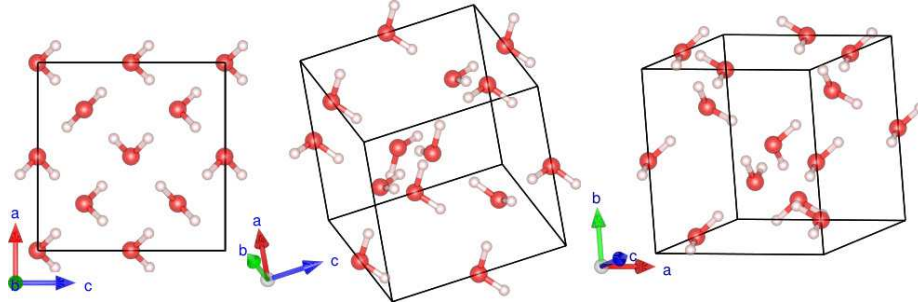


Figure 6.12: Ice I_c (ord. c) structure.

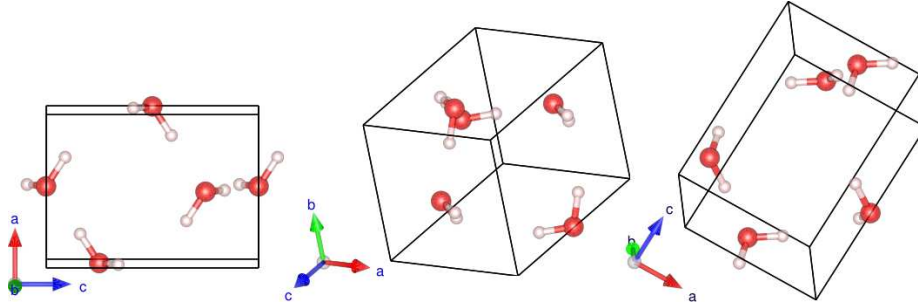


Figure 6.13: Ice I_c (ord. d) structure.

phases have been investigated in this work. Order a , the most stable of all 11 configurations, is ferroelectric and has space group $I4_1md$ (a subgroup of $Fd\bar{3}m$). It has been designated ice XI_c , analogous to the most stable hexagonal ice XI_h ([Raza et al., 2011]). Order b with space group $Pna2_1$ and c with space group $P4_1$ are ferroelectric, whereas order d with space group $P4_12_12$ is anti-ferroelectric. The structures, as they were optimized by VASP including symmetry operations, are shown in Figs. 6.10-6.13. Table 6.8 lists the structural parameters of the PBE optimized cells.

Figs. 6.14-6.17 show the energy-volume curves of the PBE and RPA volume scans. Table 6.9 compares our energy results with other theoretical and experimental values.

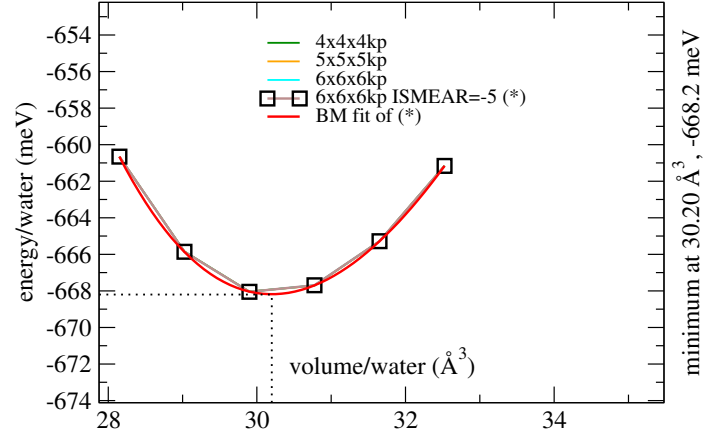
Ice I_c should be less stable than ice I_h , this result has not been achieved for all configurations and methods. The energy relative to I_h (in parentheses) is only less negative for order c and d whereas order a is predicted more stable and the RPA calculations for order b are essentially isoenergetic with I_h .

Interestingly the energy differences between I_h and I_c and the various I_c

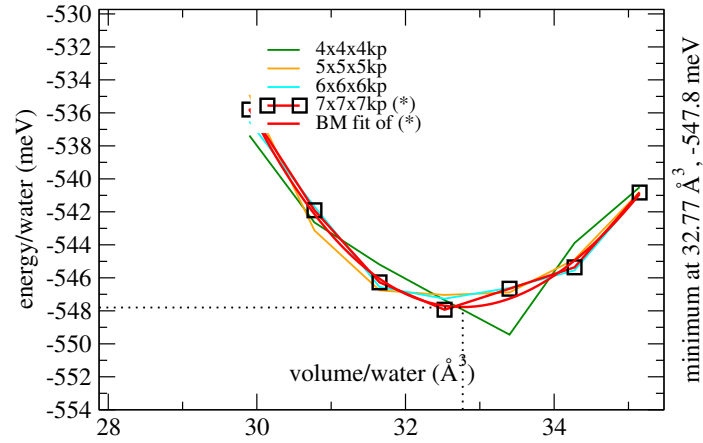
	VASP cell	a (Å)	b/a	c/a
PBE, ord. a	body centered tetragonal	4.4059	1.0003	1.4138
PBE, ord. b	simple orthorhombic	4.4189		1.4010
PBE, ord. c	simple tetragonal	6.2295		0.9996
PBE, ord. d	simple tetragonal	4.4350		1.3874

Table 6.8: Structural results for ice I_c .

a) Ice I_c (ord. a), PBE



b) Ice I_c (ord. a), RPA+EXX



c) Ice I_c (ord. a), RPA+SCHF

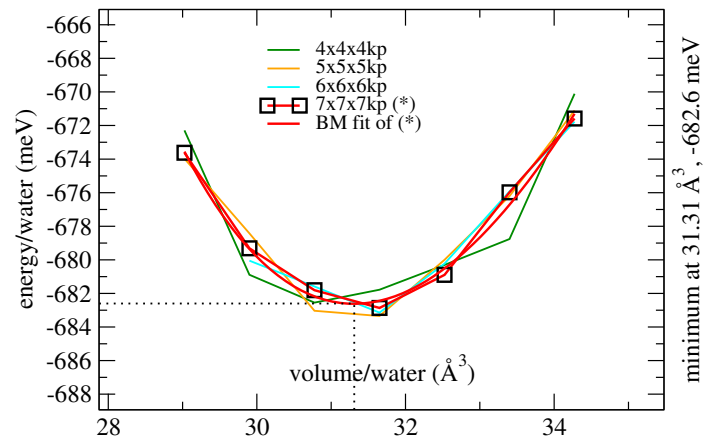
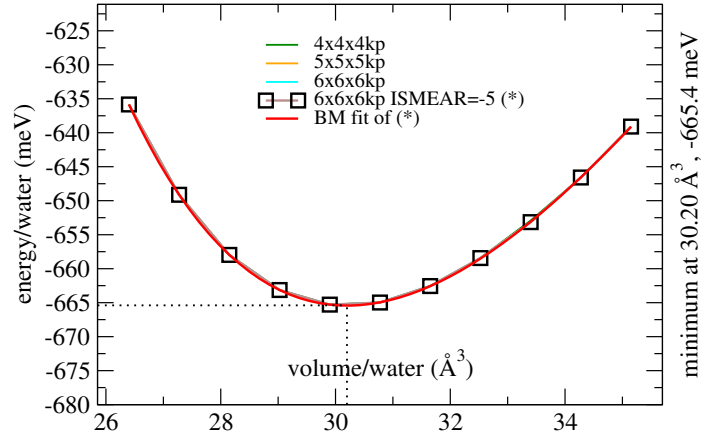
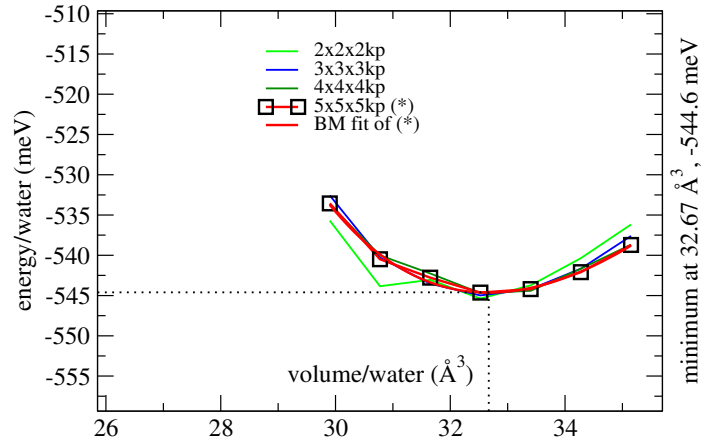


Figure 6.14: Ice I_c (ord. a) - PBE, RPA+EXX and RPA+SCHF energy-volume curves.

a) Ice I_c (ord. b), PBE



b) Ice I_c (ord. b), RPA+EXX



c) Ice I_c (ord. b), RPA+SCHF

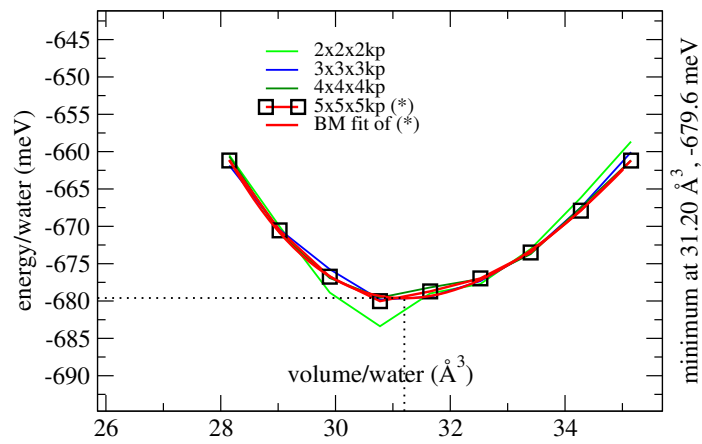
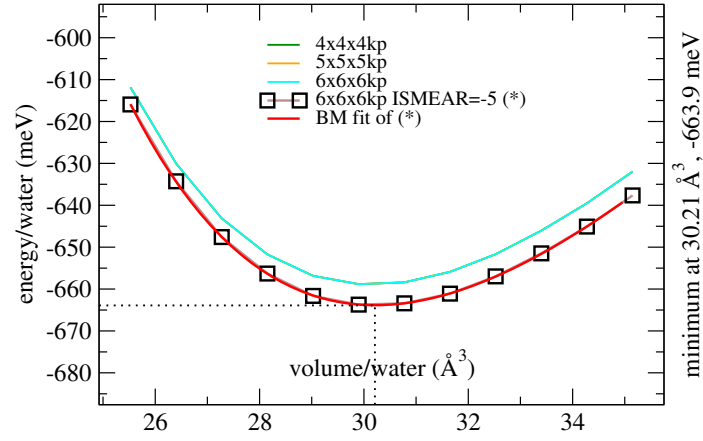
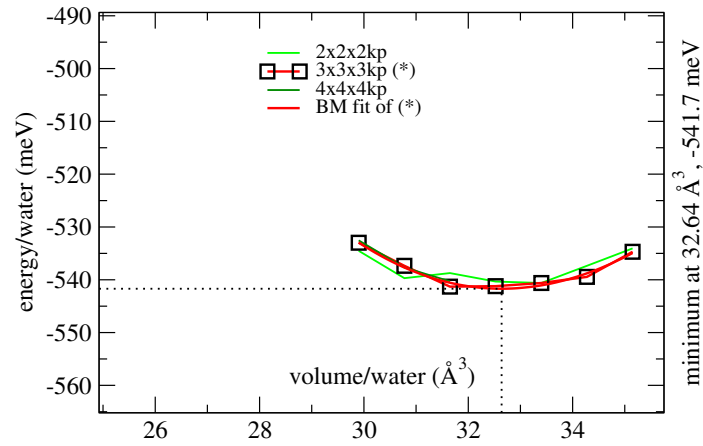


Figure 6.15: Ice I_c (ord. b) - PBE, RPA+EXX and RPA+SCHF energy-volume curves.

a) Ice I_c (ord. c), PBE



b) Ice I_c (ord. c), RPA+EXX



c) Ice I_c (ord. c), RPA+SCHF

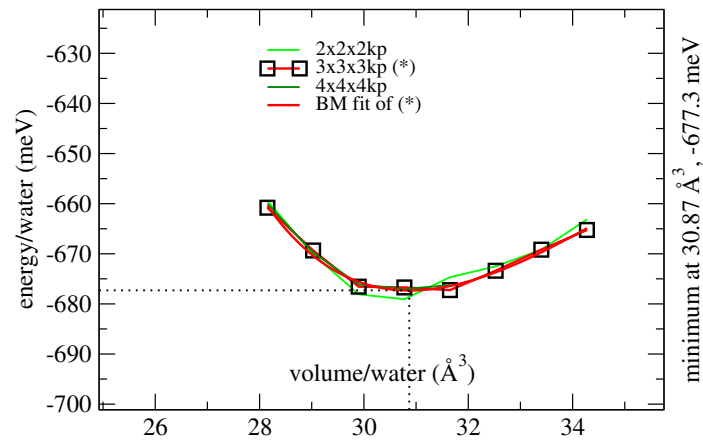
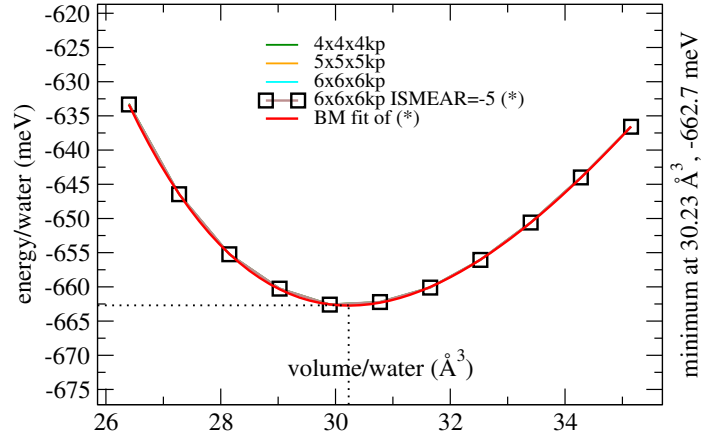
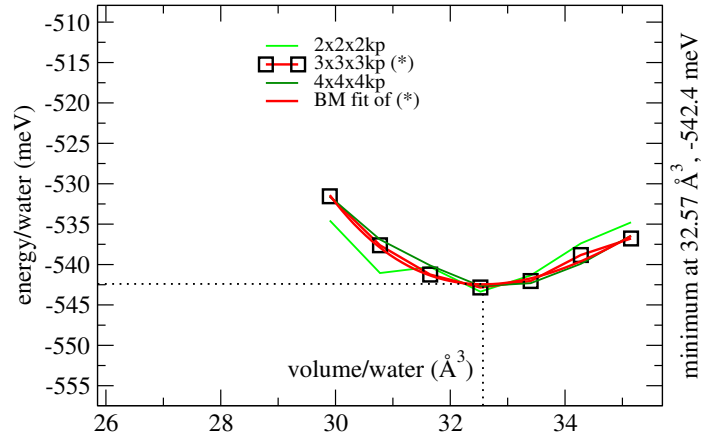


Figure 6.16: Ice I_c (ord. c) - PBE, RPA+EXX and RPA+SCHF energy-volume curves.

a) Ice I_c (ord. d), PBE



b) Ice I_c (ord. d), RPA+EXX



c) Ice I_c (ord. d), RPA+SCHF

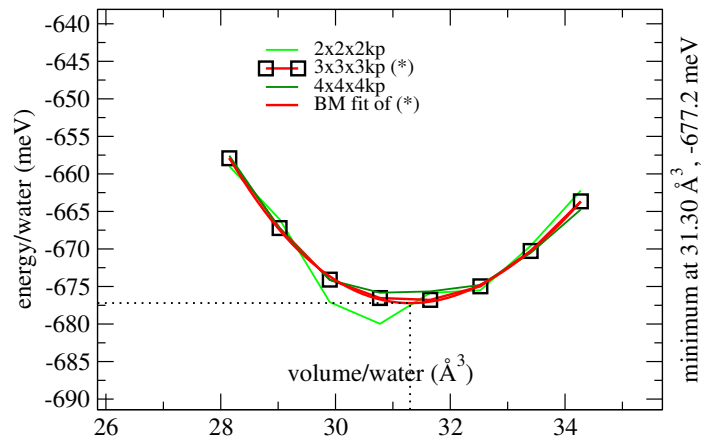


Figure 6.17: Ice I_c (ord. d) - PBE, RPA+EXX and RPA+SCHF energy-volume curves.

	E (meV)	V (\AA^3)	B (GPa)	B'
I_c (ord. a) (XI_c)				
PBE	-668 (-3)	30.20	14.82	5.63
RPA+EXX	-548 (-3)	32.77	13.81	2.56
RPA+SCHF	-683 (-3)	31.31	15.21	4.50
optPBE-vdW ^a	-677	31.53		
DMC ^a	-599 ± 2	31.28 ± 0.31		
I_c (ord. b)				
PBE	-665 (0)	30.20	14.64	5.76
RPA+EXX	-545 (0)	32.67	11.93	6.63
RPA+SCHF	-680 (0)	31.20	15.61	6.06
I_c (ord. c)				
PBE	-664 (1)	30.21	14.57	5.63
RPA+EXX	-542 (3)	32.64	11.74	0.53
RPA+SCHF	-677 (2)	30.87	16.07	10.39
I_c (ord. d)				
PBE	-663 (2)	30.23	14.49	5.43
RPA+EXX	-542 (2)	32.57	12.19	9.05
RPA+SCHF	-677 (2)	31.30	17.20	2.67
I_c (disordered)				
Expt. ^b	n/a (0.37)			
Expt. ^c	n/a (0.36)			
Expt. ^d	n/a (0.52)			
Expt. ^e		32.105		
PBE ^f	-663	30.50	14.67	5.7
vdW-DF2 ^f	-648	33.29	12.96	5.5

Table 6.9: Results for ice I_c . Cohesive energy and equilibrium volume are per molecule, the energy relative to I_h , if available, is written in parentheses. ^aRef.[Raza et al., 2011], ^bRef.[Yamamuro et al., 1987], ^cRef.[Handa et al., 1986b], ^dRef.[Handa et al., 1986a], ^eRef.[Petrenko, 1999] at 72 K and 0 GPa, ^fRef.[Murray and Galli, 2012]: DFT calculation with the vdW-DF2 density functional ([Lee et al., 2010]).

phases is almost entirely independent of the method. PBE, RPA+EXX and RPA+SCHF all yield identical values. Only DMC seems to give perfect agreement with experiment, but it is certainly not guaranteed that the DMC was k-point converged, and even the statistical error bars (5 meV for I_h) are so large that DMC might yield a different order when converged.

Experimentally, the enthalpy difference of an ice I_h to I_c transition was measured to be 0.37 meV (35.6 ± 0.8 J/mol, adjusted for 0 K) in [Yamamuro et al., 1987]. Handa et al. also measured the enthalpy difference to around 35 J/mol ([Handa et al., 1986b]), 50 J/mol ([Handa et al., 1986a]) and in the range of about 30 – 50 J/mol ([Handa et al., 1988]), depending on the origin of the I_c phase. Other literature values show energy differences around or below 1 meV (see [Raza et al., 2011] [Yamamuro et al., 1987]), in which surface effects are supposed to be responsible for higher values ([Ghormley, 1968]).

We however note that these energy differences are between the two disordered polymorphs, and whereas our I_h structure represents the true disordered I_h well, the cubic structure I_c (ord. a) is very well ordered. Interestingly the ordered phase of I_h (XI_h) considered in chapter 6.5 is isoenergetic to the ordered phase of cubic ice. We believe that this is fully consistent with the experimental results and hence our values are most likely even more accurate than DMC.

Like in the proton disordered hexagonal phase (Section 6.4), there may be an overestimation of the hydrogen bond in the PBE functional. RPA+EXX and RPA+SCHF volumes are in good agreement with experiment. Both, optPBE-vdW and DMC are underestimating the experimental volume but are in reasonable agreement too.

6.8 Ice IX

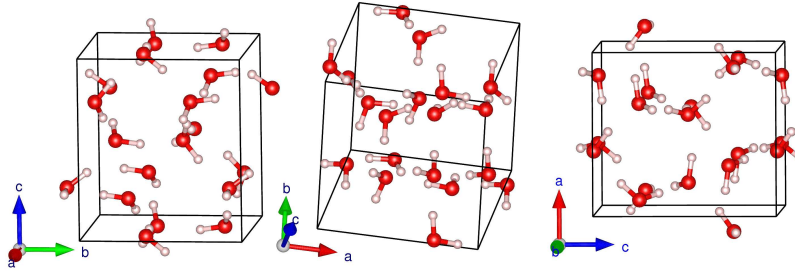
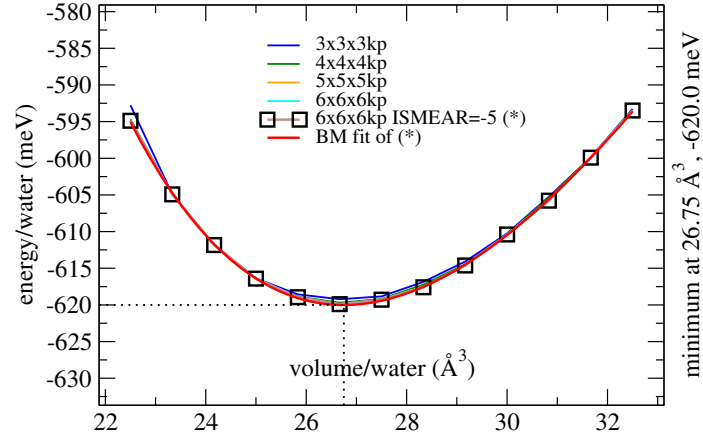


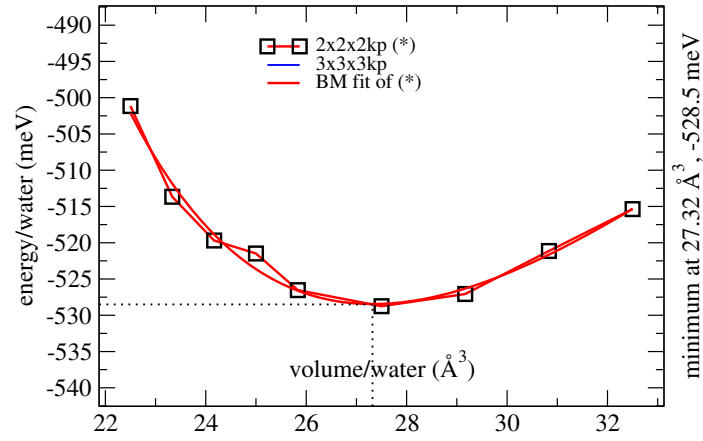
Figure 6.18: Ice IX structure.

When cooling the almost ([Londono et al., 1993]) proton disordered ice III sufficiently fast ([La Placa et al., 1973]) and keeping a pressure range of 270 – 320 MPa, proton ordering starts at about 210 K. Below 165 K, where protons are almost ordered, the phase is designated ice IX due to earlier measurements ([Whalley et al., 1968]) of the dielectric constant. Ordering completes only at lower temperatures ([Londono et al., 1993]). Ice III and IX both have the space group $P4_12_12$ (#92).

a) Ice IX, PBE



b) Ice IX, RPA+EXX



c) Ice IX, RPA+SCHF

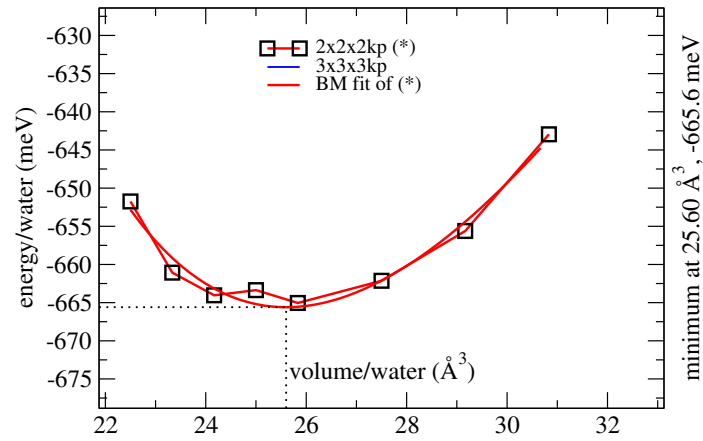


Figure 6.19: Ice IX - PBE, RPA+EXX and RPA+SCHF energy-volume curves.

	a (Å)	c (Å)	c/a
PBE	6.5845	7.3921	1.1227
Expt. ^a	6.6782(2)	6.7027(3)	1.0037(1)
Expt. ^b	6.73 ± 0.01	6.83 ± 0.01	1.0149

Table 6.10: Structural results for ice IX, ^aRef.[Londono et al., 1993], ^bRef.[La Placa et al., 1973].

	E (meV)	V (Å ³)	B (GPa)	B'
PBE	−620 (45)	26.75	9.19	3.50
RPA+EXX	−528 (16)	27.32	6.37	5.83
RPA+SCHF	−666 (14)	25.60	8.89	3.75
Expt.	−607 (3) ^a	25.63 ^b	10 ^a	
Expt.	−606 (4) ^c	25.80 ^d	8.9 ^e	
FHI-aims/PBE ^f	−587 (49)	26.06		
FHI-aims/PBE0+vdW ^{TSf}	−670 (2)	23.85		
MC TIP4P ^g	−635			
MD SPC/E ^g	−584			

Table 6.11: Results for ice IX. Cohesive energy and equilibrium volume are per molecule, the energy relative to I_h , if available, is written in parentheses. ^aRef.[Whalley, 1984] at zero pressure and temperature (see text for bulk modulus), ^bRef.[Londono et al., 1993], ^cRef.[Handa et al., 1988, Table 4], ^dRef.[La Placa et al., 1973], ^eRef.[Gammon et al., 1983], ^fRef.[Santra et al., 2011] [Santra et al., 2013], ^gRef.[Baranyai et al., 2005]: MC simulation with TIP4P model at 5 K, −0.20(5) GPa and molecular dynamics simulation with a SPC/E model ([Berendsen et al., 1987]) at 5 K, −0.08(2) GPa.

The tetragonal unit cell is pseudo-cubic ($c/a \approx 1$) and contains 12 water molecules (Fig. 6.18). Ice IX is anti-ferroelectric ([Knight and Singer, 2006]).

Neutron diffraction studies with D₂O ([Londono et al., 1993]) showed lattice parameters of $a = 6.7199(1)$ Å, $c = 6.7919(1)$ Å and $c/a = 1.0107(1)$ as well as a cell volume of 25.63 Å³ per molecule at zero pressure and 30 K. An earlier measurement of [La Placa et al., 1973] showed $a = 6.73 \pm 0.01$ Å and $c = 6.83 \pm 0.01$ Å. Table 6.10 compares structural data from the PBE calculation with literature values.

Brillouin scattering in [Gammon et al., 1983] yielded a bulk modulus of 8.899 GPa. Also, it was estimated in [Whalley, 1984] with a simple model, where the compressibility is given by $\kappa = 9/Nkr^2$, in which N is the number density of molecules, k the intermolecular hydrogen-bonded O-O force constant, and r the mean O-O distance. This led to $\kappa = 10$ Mbar^{−1}, and thus a bulk modulus of 10 GPa.

Table 6.11 summarizes energy, volume and the bulk modulus. Fig. 6.19 shows the energy-volume curves of the PBE and RPA volume scans.

The energy relative to ice I_h was calculated for zero pressure and temperature to be 3.5 meV (0.34 kJ/mol) in [Whalley, 1984], which, with the cohesive energy of ice I_h of −610 meV (−58.82 kJ/mol) ([Whalley, 1984]), results in a cohesive energy of −606.5 meV for ice VIII. Another measurement shows a relative enthalpy of 3.7 meV (0.353 ± 0.006 kJ/mol) ([Handa et al., 1988, Table 4]) at

zero pressure and a temperature of 143 K.

PBE0+vdW is overbinding and yields a too small volume. PBE is able to predict both, energy and volume in this moderate-pressure phase rather accurately. RPA+EXX is underestimating the binding, but with +6 % it is in good agreement with experiment. An excellent agreement with experimental volumes and pressures yields RPA+SCHF. The energy relative to I_h already shows a comparatively large deviation of about 40 meV from experiment for PBE, whereas with only about 10 meV deviation RPA energies are in better agreement with experiments.

6.9 Ice II

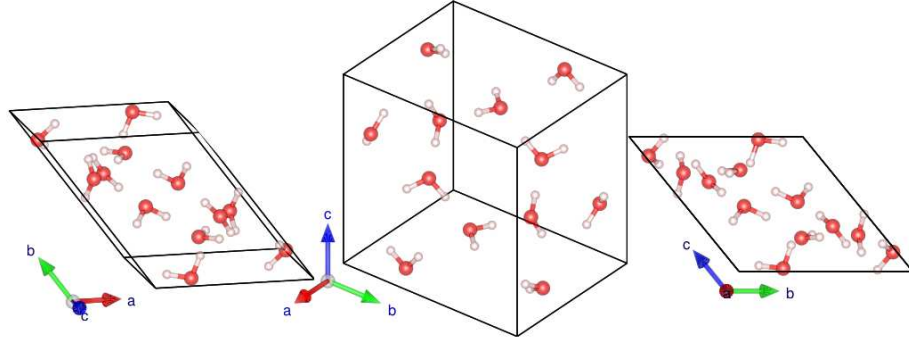


Figure 6.20: Ice II structure.

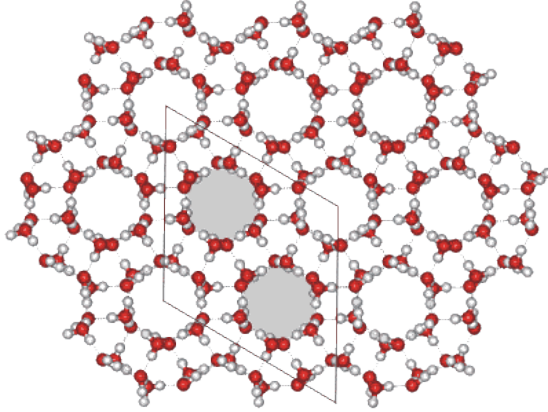


Figure 6.21: Alternative ice II unit cell, top view ([Chaplin, 2012]).

Ice II is a proton ordered phase with space group $R\bar{3}$ (#148) ([Kamb, 1964a]). It has no direct proton disordered counterpart but may be formed from ices I_h at 198 K and 300 MPa, ice V at 238 K or by cooling ice III ([Chaplin, 2012]) (see phase diagram, Fig. 2.3). At ambient pressure and above 160 K it transforms into ice I_c . The 12 molecule rhombohedral unit cell (Fig. 6.20) consists of

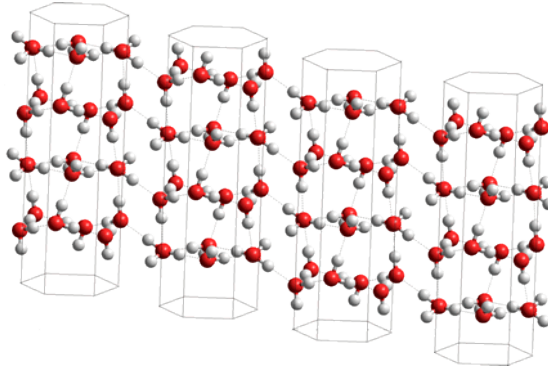


Figure 6.22: Alternative ice II unit cell, side view ([Chaplin, 2012]).

	a (Å)	α (°)	a_h (Å)	c_h (Å)	c/a
PBE	7.6605	112.809	12.7618	6.2892	0.4928
Expt. ^a	7.741	113.1	12.918(0)	6.221(0)	0.4816(0)
Expt. ^b	7.734	113.1	12.9035(3)	6.2338(2)	0.483
MC TIP4P ^c	7.78	113.1	12.9828	6.2530	0.4816

Table 6.12: Structural results for ice II, ^aRef.[Lobban et al., 2002], ^bRef.[Fortes et al., 2005], ^cRef.[Vega et al., 2005].

two hexagonal rings connected by hydrogen bonds. An alternative hexagonal (triply-primitive) unit cell with 36 molecules (Figs. 6.21 and 6.22) gives a better view at the hexagonal structure and is also used in literature for structural data.

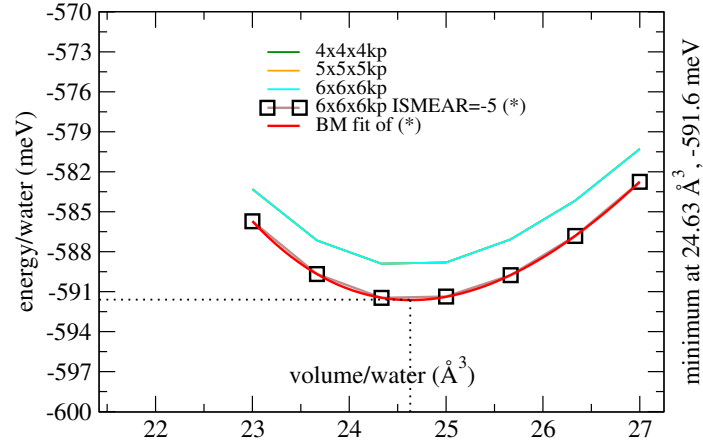
The lattice parameters of the rhombohedral cell were determined in [Kamb, 1964a] with X-ray to be $a = 7.78(1) \pm 0.01$ Å and $\alpha = 113.1 \pm 0.2^\circ$ ($a = b = 12.97 \pm 0.02$ Å, $c = 6.25 \pm 0.01$ Å for the hexagonal cell) at atmospheric pressure and 123 K, although most probably helium inclusion significantly affected the structure and led to a stuffed ice helium hydrate ([Lobban et al., 2002]), therefore the data may not be used for comparisons. The corresponding hexagonal cell was measured with powder neutron diffraction with D₂O in ensured absence of such inclusions at least in [Lobban et al., 2002] and [Fortes et al., 2005]:

In the previous experiment, lattice parameters at about 200 K were found to be $a_h = 12.918(0)$ Å, $c_h = 6.221(0)$ Å ($a = 7.741$ Å, $\alpha = 113.1^\circ$) and $c_h/a_h = 0.4816(0)$ at 0.28 GPa as well as $a_h = 12.864(0)$ Å, $c_h = 6.186(0)$ Å ($a = 7.707$ Å, $\alpha = 113.1^\circ$) and $c_h/a_h = 0.4809(0)$ at 0.48 GPa. Volumes per water molecule and densities at these pressures were $V = 24.97$ Å³ ($\rho = 1.330$ g/cm³) and $V = 24.63$ Å³ ($\rho = 1.348$ g/cm³), respectively, and the isothermal bulk modulus was determined to be 14.8(1) GPa.

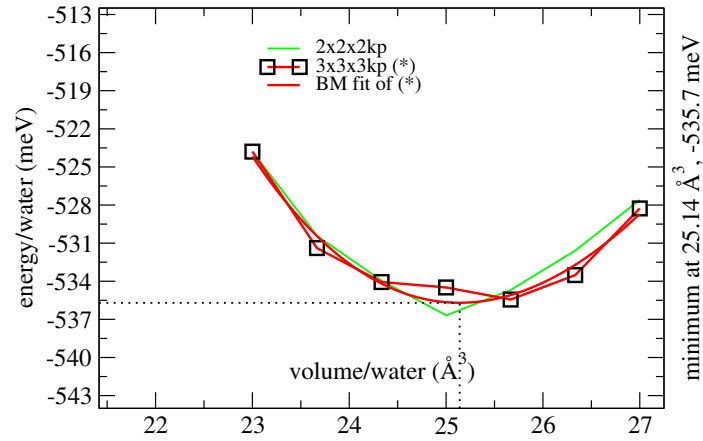
In the latter measurement, [Fortes et al., 2005], lattice parameters at about 5 K and ambient pressure were $a_h = 12.9035(3)$ Å, $c_h = 6.2338(2)$ Å ($a = 7.734$ Å, $\alpha = 113.1^\circ$) and $c_h/a_h = 0.483$. The measured volume was 24.97 Å³ and the bulk modulus, referenced to 225 K, was 12.13 ± 0.07 GPa (with a fixed first pressure derivative of 6.0 taken from *ab initio* calculations). Table 6.12 summarizes structural results from the PBE calculation as well as experimental values.

The energy difference to ice I_h was calculated for zero pressure and temperature to be 0.59 meV (0.057 kJ/mol) ([Whalley, 1984]) and thus, ice II is just

a) Ice II, PBE



b) Ice II, RPA+EXX



c) Ice II, RPA+SCHF

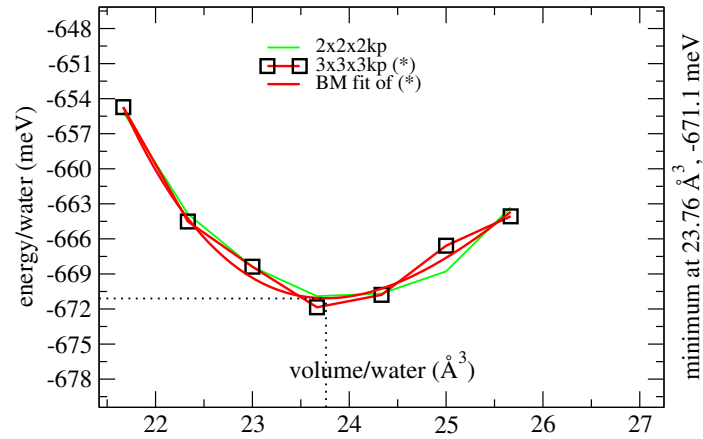


Figure 6.23: Ice II - PBE, RPA+EXX and RPA+SCHF energy-volume curves.

	E (meV)	V (\AA^3)	B (GPa)	B'
PBE	−592 (73)	24.63	15.16	5.27
RPA+EXX	−536 (9)	25.14	17.97	3.22
RPA+SCHF	−671 (9)	23.76	20.61	9.87
Expt.	−610 (0) ^c	24.97 ^b	12.13 ± 0.07 ^b	
Expt.	−609 (1) ^a	24.63 ^e	10 ^a	
Expt. ^e		24.97	14.8(1)	
DMC ^d	−609 ± 5 (−4)	24.7 ± 0.2	20.1 ± 0.4	
FHI-aims/PBE ^d	−567 (69)	24.97		
FHI-aims/PBE0+vdW ^{TSd}	−666 (6)	23.63		
MC TIP4P/Ice ^f	−705 (9)	24.66		
MC TIP4P/2005 ^f	−653 (9)	24.30		

Table 6.13: Results for ice II. Cohesive energy and equilibrium volume are per molecule, the energy relative to I_h , if available, is written in parentheses. ^aRef.[Whalley, 1984] at zero pressure and temperature (see text for bulk modulus), ^bRef.[Fortes et al., 2005] volume at about 5 K and ambient pressure, the bulk modulus at 225 K with a fixed first pressure derivative of 6.0, ^cRef.[Handa et al., 1988] at 162 K and ambient pressure, ^dRef.[Santra et al., 2011] [Santra et al., 2013], ^eRef.[Lobban et al., 2002] at 0.48 resp. 0.28 GPa, ^fRef.[Aragones et al., 2007] at 0 K and zero pressure.

slightly less stable than ice I_h . With the cohesive energy of ice I_h of −610 meV (−58.82 kJ/mol) from [Whalley, 1984], the cohesive energy of ice II is −609.4 meV. [Whalley, 1984] also estimated (see also ice IX results) the bulk modulus to be about 10 GPa.

Another measurement shows a relative enthalpy of 0.19 ± 0.05 meV (0.018 ± 0.005 kJ/mol) ([Handa et al., 1988, Table 4]) at zero pressure and a temperature of 162 K. Table 6.13 summarizes energy, volume, bulk modulus and its first pressure derivative. Fig. 6.23 shows the energy-volume curves of the PBE and RPA volume scans.

PBE shows a comparatively large deviation of +73 meV, whereas RPA+EXX and RPA+SCHF yield reasonable results. The lower stability of +9 meV relative to I_h is the same for both, RPA+EXX and RPA+SCHF. DMC predicts this phase to be equally or more stable than hexagonal ice, the volume agreement, however is excellent. PBE0+vdW^{TS} and MC also yield reasonable volumes and PBE0+vdW^{TS} correctly predicts the phase less stable than I_h .

6.10 Ice XIII

In 2006, ice XIII (Fig. 6.24) was successfully prepared and the structure determined by neutron powder diffraction ([Salzmann, 2006]). The proton-ordered ice XIII phase has the monoclinic $P2_1/a$ (#14) ([Salzmann et al., 2006]) space group and the unit cell contains 28 molecules. It is formed from the proton-disordered ice V by doping with HCl below 130 K and at 0.5 GPa. The unit cell parameters in this experiment were measured to be $a = 9.2417(1)$ \AA , $b = 7.4724(1)$ \AA , $c = 10.2970(1)$ \AA and $\beta = 109.6873(9)^\circ$ ($\alpha = \gamma = 90^\circ$) at ambient pressure and 80 K. This results in a volume of 23.9114 \AA^3 per water molecule. Table 6.14

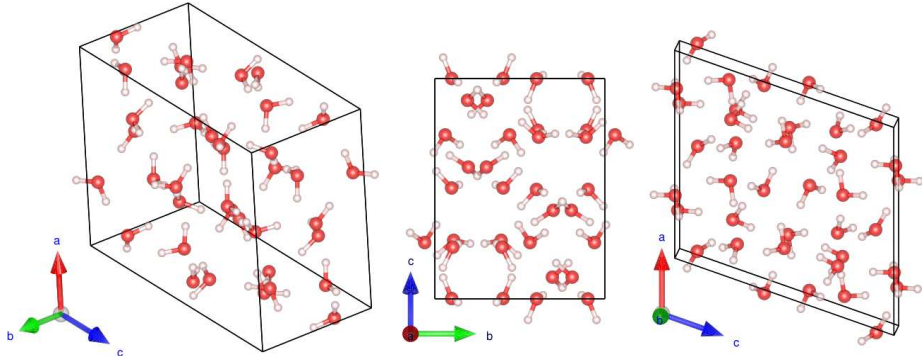


Figure 6.24: Ice XIII structure.

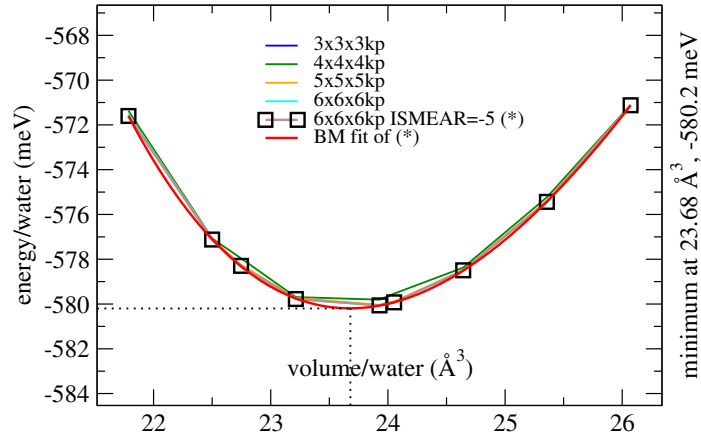


Figure 6.25: Ice XIII - PBE energy-volume curves.

compares structural data from the PBE calculation with literature values.

In [Salzmann, 2006], the effects of doping have been studied, and the maximum enthalpy difference they reached between the XIII-V (and vice versa) transition was 250 J/mol (2.6 meV). Together with the enthalpy of the V- I_h transition of 966 ± 6 J/mol (10.0 meV) ([Handa et al., 1988]) or 950 J/mol (9.8 meV) ([Whalley, 1984]) this yields a difference to ice I_h of about 1.2 kJ/mol (13 meV). With the cohesive energy of ice I_h of -58.82 kJ/mol (-610 meV) [Whalley, 1984], the cohesive energy of ice XIII is -57.62 kJ/mol (-597 meV). Table 6.15 summarizes and compares with experimental and theoretical values energy, volume, bulk modulus and its first pressure derivative. Fig. 6.25 shows the energy-volume curve of the volume scan.

	a (Å)	b (Å)	c (Å)	α (°)	β (°)	γ (°)
PBE	9.1520	7.4900	10.2484	90	109.30	90
Expt. ^a	9.2417(1)	7.4724(1)	10.2970(1)	90	109.6873(9)	90

Table 6.14: Structural results for ice XIII, ^aRef.[Salzmann, 2006] at ambient pressure and 80 K.

	E (meV)	V (\AA^3)	B (GPa)	B'
PBE	−580 (85)	23.67	15.05	6.11
Expt. ^a	−597 (13)	23.911		
MC TIP4P/2005 ^b	−614	23.684		
MC TIP4P/Ice ^b	−675	24.027		
FHI-aims/PBE ^c	−556 (80)	24.07		
FHI-aims/PBE0+vdW ^{TSc}	−661 (11)	22.47		

Table 6.15: Results for ice XIII. Cohesive energy and equilibrium volume are per molecule, the energy relative to I_h in parentheses. ^aRef.[Salzmann, 2006] XIII-V transformation at ambient pressure and 80 K, [Handa et al., 1988] V- I_h transformation at 144 K and ambient pressure, [Whalley, 1984] I_h energy at zero pressure and temperature. Summation of I_h energy and energy differences V- I_h and XIII-V (see text), ^bRef.[Martin-Conde et al., 2006] residual internal energy, volumes for D_2O , ^cRef.[Santra et al., 2011] [Santra et al., 2013].

The PBE binding energy shows a growing error with increasing pressure, however the volume is comparatively well described (about -5%) with respect to the experimental value. PBE0+vdW^{TS} overestimates the binding energy, also the volume is estimated too small. MC simulations are able to predict a volume in good agreement with experiments.

RPA calculations for this specific phase were omitted due to the large unit cell.

6.11 Ice XV

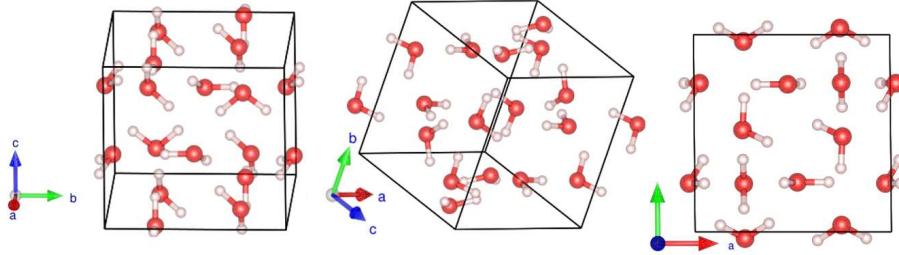
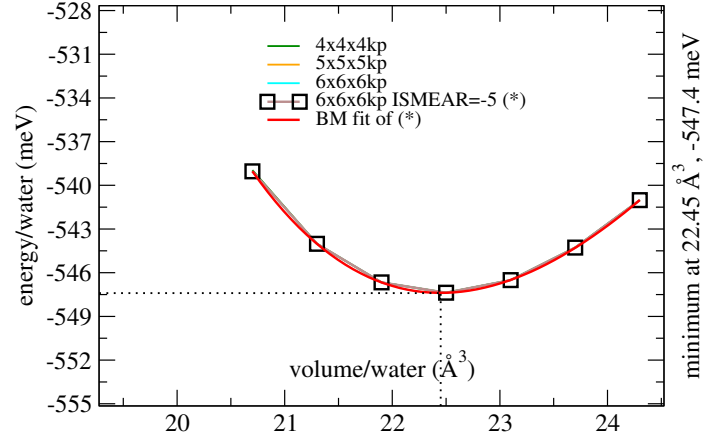


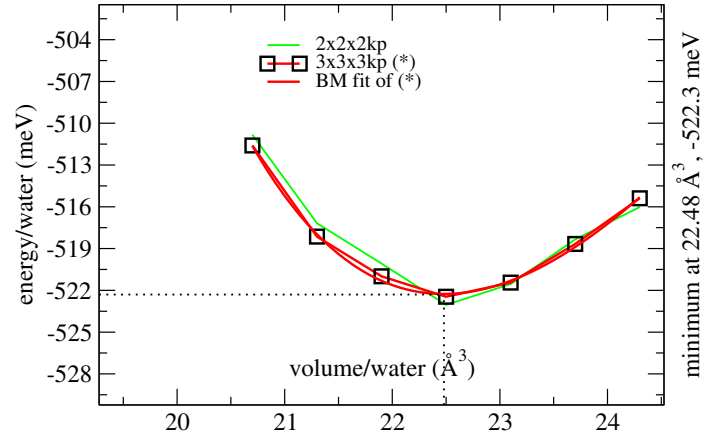
Figure 6.26: Ice XV structure.

In 2009, the proton-ordered counterpart to the proton-disordered phase VI has been identified ([Salzmann et al., 2009]) and named ice XV. It is stable below 130 K in the pressure range from 0.8 GPa to 1.5 GPa. The triclinic structure (Fig. 6.26) has space group $P\bar{1}$ (#2). It has been shown to be anti-ferroelectric also in [Salzmann et al., 2009], although ferroelectricity was predicted by theory ([Knight and Singer, 2005], [Kuo and Kuhs, 2006]). The pseudo-orthorhombic structure has been identified by neutron diffraction and D_2O ice at ca. 0.9 GPa and 80 K to $a = 6.2323 \text{ \AA}$, $b = 6.2438 \text{ \AA}$, $c = 5.7903 \text{ \AA}$ (90.06° , 89.99° , 89.92°) in [Salzmann et al., 2009]. This leads to a volume of 22.532 \AA^3 ($13.569 \text{ cm}^3/\text{mol}$). Table 6.16 compares structural data from the PBE calculation with literature

a) Ice XV, PBE



b) Ice XV, RPA+EXX



c) Ice XV, RPA+SCHF

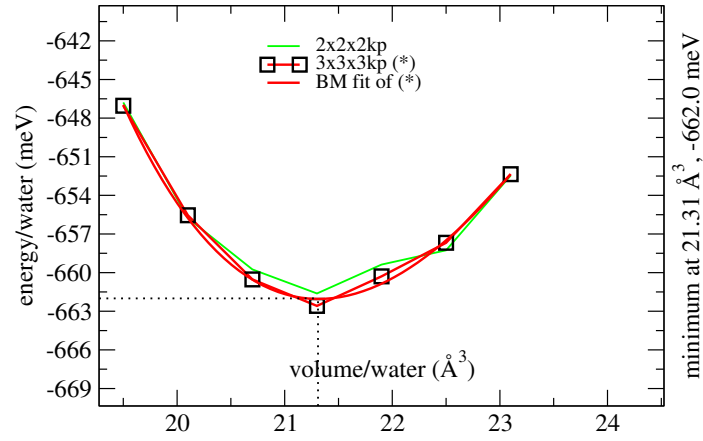


Figure 6.27: Ice XV - PBE, RPA+EXX and RPA+SCHF energy-volume curves.

	a (Å)	b (Å)	c (Å)	α (°)	β (°)	γ (°)
PBE	6.2145	6.2162	5.8116	90.15	89.75	90.49
Expt. ^a	6.2323	6.2438	5.7903	90.06	89.99	89.92

Table 6.16: Structural results for ice XV, ^aRef.[Salzmann et al., 2009] at 0.9 GPa and 80 K.

	E (meV)	V (Å ³)	B (GPa)	B'
PBE	−547 (118)	22.45	16.18	6.17
RPA+EXX	−522 (22)	22.48	19.04	7.99
RPA+SCHF	−662 (18)	21.32	25.24	6.26
Expt. ^a		22.53		
FHI-aims/PBE ^b	−526 (110)	22.82		
FHI-aims/PBE0+vdW ^{TSb}	−646 (26)	21.45		

Table 6.17: Results for ice XV. Cohesive energy and equilibrium volume are per molecule, the energy relative to I_h , if available, is written in parentheses, ^aRef.[Salzmann et al., 2009] at 0.9 GPa and 80 K, ^bRef.[Santra et al., 2011] [Santra et al., 2013].

values.

Explicit measurements of enthalpy or bulk modulus of this comparatively new phase in literature are not available. Table 6.17 lists energies, volumes, bulk moduli and the first pressure derivative. Fig. 6.27 shows the energy-volume curves of the PBE and RPA volume scans.

Although ice XV is yet a moderate-pressure phase, the PBE binding energy is too small because of missing vdW interaction. With respect to the volumes of the next phases upon rising the pressure, XIII and VIII, all volumes in Table 6.17 are reasonable. However, missing DMC and zero temperature experimental values make comparisons rather difficult. With respect to the experimental value, PBE and RPA+EXX agree well and RPA+SCHF deviates by only −5.4 %. With increasing pressure, PBE0+vdW^{TS} performs better than PBE due to the vdW interaction getting more important. The energy relative to I_h is in agreement with RPA values and PBE clearly underbinds this phase.

6.12 Ice VIII

Ice VIII is the proton ordered form of the proton disordered ice VII with tetragonal space group $I4_1/amd$ (#141) and 8 molecules in the unit cell. The oxygen sublayer is the same for both structures and all molecules have an equivalent environment. The structure, shown in Fig. 6.28, consists of two interpenetrating, but not interconnected cubic ice I_c sublattices ([Kuhs et al., 1984]). The sublattices have opposite dipole moments, which results in an anti-ferroelectric structure ([Pruzan et al., 1993]). A disorder-order transition happens at about 5°C when cooling down at pressures starting from about 2 GPa. At 0 K, the phase exists up to about 52 GPa for H_2O and 62 GPa for D_2O (see detailed phase diagrams in [Besson et al., 1997] and [Pruzan et al., 1993]).

Neutron powder diffraction measurements in [Kuhs et al., 1984] with D_2O

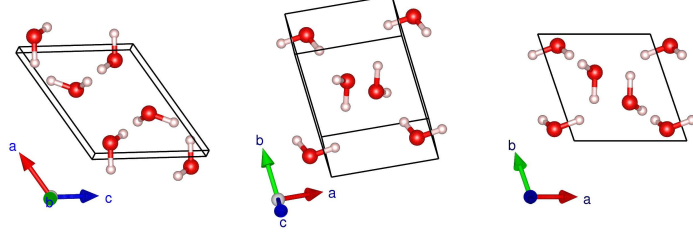


Figure 6.28: Ice VIII structure.

	a (Å)	c (Å)	c/a
PBE	4.8401	6.9827	1.4427
Expt. ^a	4.656(1)	6.775(1)	1.4551(5)
Expt. ^b	4.6779(5)	6.8029(10)	1.4543
MC TIP4P ^c	4.538	6.940	1.5293

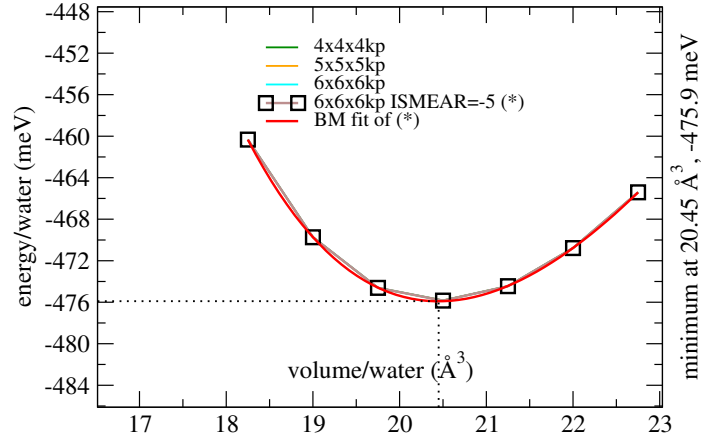
Table 6.18: Structural results for ice VIII, ^aRef.[Kuks et al., 1984], ^bRef.[Jorgensen et al., 1984], ^cRef.[Vega et al., 2005].

at 10 K and 2.4 GPa showed cell dimensions $a = 4.656(1)$ Å, $c = 6.775(1)$ Å, a c/a ratio of 1.4551(5) and a density, calculated for H₂O, of 1.628 mg/mm³ (18.360 g/cm³). In situ neutron powder diffraction measurements in [Jorgensen et al., 1984] with D₂O at 269 K and 2.5 GPa yielded $a = 4.6779(5)$ Å, $c = 6.8029(10)$ Å as well as a volume of 18.609 Å³ per molecule. Furthermore, an early X-ray diffraction experiment was done in [Kamb, 1964b], although the phase was reported as ice VII and later revised to be ice VIII. But the data is unclear and will not be used here. Table 6.18 summarizes structural results from the PBE calculation as well as experimental values.

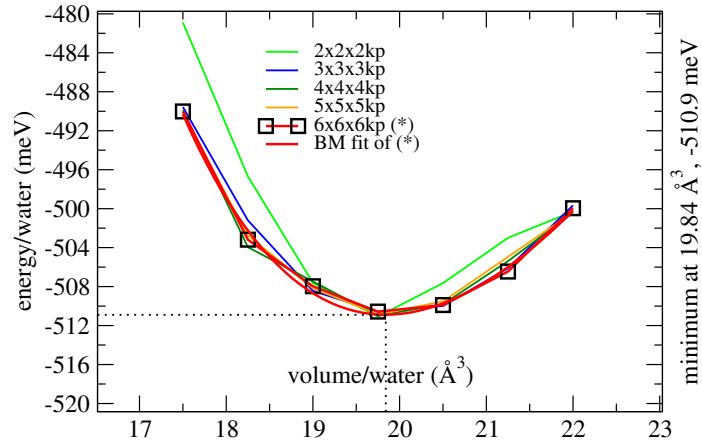
The energy relative to ice I_h was calculated for zero pressure and temperature to be 33 meV (3.16 kJ/mol) ([Whalley, 1984]), which, with the cohesive energy of ice I_h of −610 meV (−58.82 kJ/mol) ([Whalley, 1984]), results in a cohesive energy of −577 meV for ice VIII. Another measurement shows a relative enthalpy of 28 meV (2.702 ± 0.025 kJ/mol) ([Handa et al., 1988, Table 4]) at zero pressure and a temperature of 124 K. [Whalley, 1984] also estimated (see also ice IX results) the bulk modulus to about 15.9 GPa. The bulk modulus was calculated in [Yoshimura et al., 2006, Table 1] with a Vinet EOS to be 27.9 ± 0.3 GPa. The first pressure derivative is 3.6 ± 0.5 . The collection of the computed and previously reported values of volume, energy, bulk modulus and its derivative is given in Table 6.19. Fig. 6.29 shows the energy-volume curves of the PBE and RPA volume scans.

VIII is a high-pressure phase and thus all vdW including density functionals should give better results. The experimental values vary a lot (with a mean value of about 19.0 Å³) and the MC volume seems to be too low. DMC values seem to be reasonable and it makes sense to compare our results with them since DMC was excellent for all other considered phases. As opposed to the low-pressure hexagonal ice, PBE now overestimates the volume. PBE0+vdW^{TS}

a) Ice VIII, PBE



b) Ice VIII, RPA+EXX



c) Ice VIII, RPA+SCHF

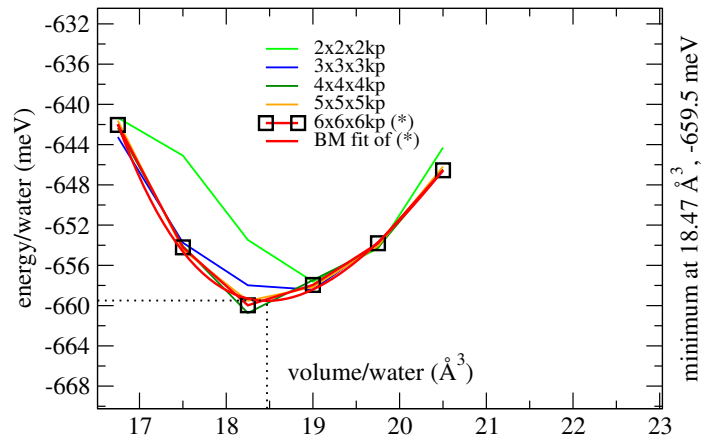


Figure 6.29: Ice VIII - PBE, RPA+EXX and RPA+SCHF energy-volume curves.

	E (meV)	V (\AA^3)	B (GPa)	B'
PBE	−476 (189)	20.45	16.43	5.65
RPA+EXX	−511 (34)	19.84	18.17	5.60
RPA+SCHF	−660 (20)	18.47	26.04	8.36
Expt.	−577 (33) ^a	18.61 ^b	15.9 ^a	
Expt. ^c		20.09	27.9 ± 0.3	3.6 ± 0.5
Expt.	−582 (28) ^d	18.36 ^e		
DMC ^f	−575 ± 5 (30)	19.46 ± 0.02	23.8 ± 0.5	
FHI-aims/PBE ^f	−459 (177)	20.75		
FHI-aims/PBE0+vdW ^{TSf}	−596 (76)	19.70		
PBE ^g	−485	20.44	16.55	6.1
vdW-DF2 ^g	−620	21.01	20.76	5.7
MC TIP4P	−492 ^h	17.86 ⁱ		
MD SPC/E ^h	−520			

Table 6.19: Results for ice VIII. Cohesive energy and equilibrium volume are per molecule, the energy relative to I_h , if available, is written in parentheses. ^aRef.[Whalley, 1984] at zero pressure and temperature (see text for bulk modulus), ^bRef.[Jorgensen et al., 1984], ^cRef.[Yoshimura et al., 2006, Table 1], ^dRef.[Handa et al., 1988], ^eRef.[Kuhs et al., 1984], ^fRef.[Santra et al., 2011] [Santra et al., 2013], ^gRef.[Murray and Galli, 2012], ^hRef.[Baranyai et al., 2005] at 5 K and 1.20(4) GPa (SPC/E) resp. 2.00(20) GPa (TIP4P), ⁱRef.[Vega et al., 2005] at 10 K and 2.4 GPa.

underestimates the binding with respect to DMC, noticeable in both, volume and relative energy. The RPA values, however, show a remarkably similar behavior as for I_h . The RPA+EXX is larger than the DMC value, whereas the RPA+HF is smaller than the DMC value. The energies show the same trend, with an overestimation of the binding energy for RPA+HF and an underestimation for RPA+EXX, as it was the case for all yet considered phases.

6.13 Ice X

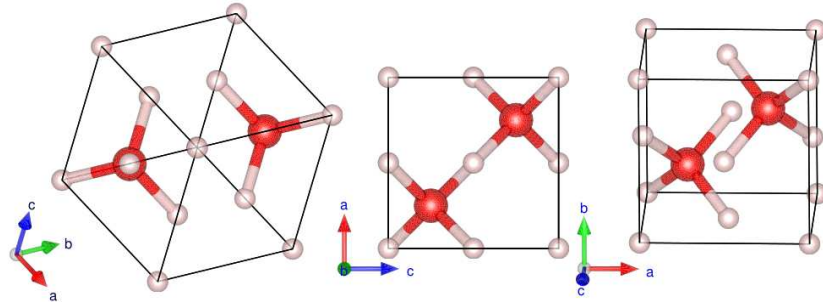
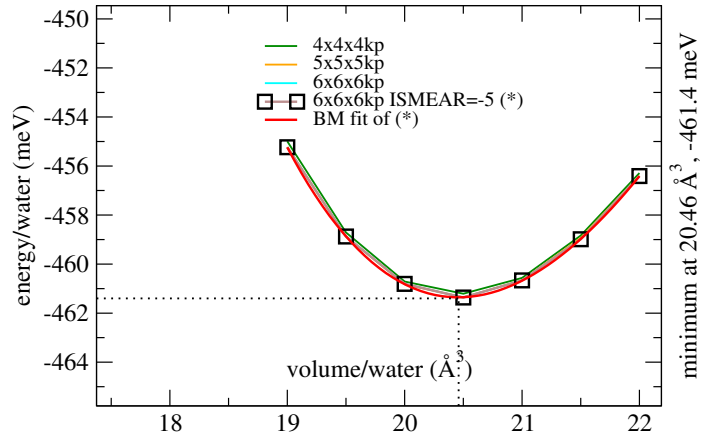


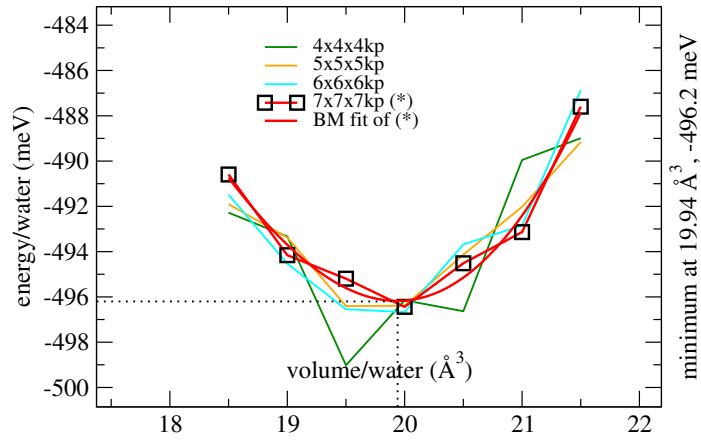
Figure 6.30: Ice X structure.

Ice VII transforms to ice X ([Polian and Grimsditch, 1984]) (Fig. 6.30) under increasing pressure beginning at about 62 GPa ([Goncharov et al., 1996],

a) Ice X, PBE



b) Ice X, RPA+EXX



c) Ice X, RPA+SCHF

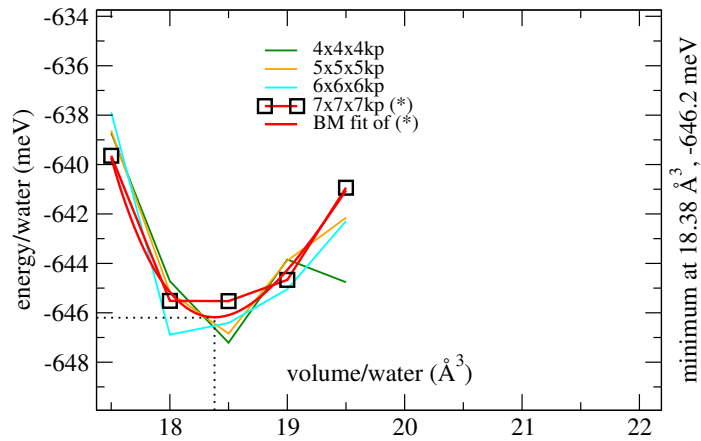


Figure 6.31: Ice X - PBE, RPA+EXX and RPA+SCHF energy-volume curves.

[Aoki et al., 1996] and [Loubeyre et al., 1999]) in a first-order transition ([Hirsch and Holzapfel, 1986]) while keeping the $Pn\bar{3}m$ (#224) space group. There are two positions possible in the proton-disordered ice VII to put a proton along each O-O-axis. During compression, these two positions move into a single symmetric point. Actually the proton permanently tunnels between the two minimum positions of the double-well potential and therefore the *ice rules* are violated. The ice X phase is stable up to at least 210 GPa ([Goncharov et al., 1996]). The oxygen atoms are bcc arranged, and the H-atoms are finally positioned symmetrically between them (Fig. 6.30).

BM EOS of ice VII under static compression to 128 GPa at 300 K can be found in [Hemley et al., 1987, Table 1]. The equation of state therein crosses the VII-X phase transition and solely one EOS for both phases is used. It reports a zero-pressure volume of $12.3 \pm 0.3 \text{ cm}^3/\text{mol}$ (20.42 \AA^3) and zero-pressure bulk modulus of $23.7 \pm 0.9 \text{ GPa}$ as well as a first pressure derivative of 4.15 ± 0.07 . The volume leads to lattice parameters for the cubic cell of $a = 2.733 \pm 0.03 \text{ \AA}$ ([Hemley et al., 1987, Table 1]). At the presumed VII-X transition pressure, [Hemley et al., 1987, Table 1] shows a volume of about $6 \text{ cm}^3/\text{mol}$.

An X-ray diffraction experiment in [Loubeyre et al., 1999] for ice VII with pressure up to 170 GPa at 300 K shows a Vinet EOS fitted volume of $14.52 \text{ cm}^3/\text{mol}$ (24.111 \AA^3), a bulk modulus of 4.26 GPa and a first pressure derivative of 7.75. Another experiment in [Somayazulu et al., 2008] shows similar values. In [Ahart et al., 2011], Brillouin scattering up to over 100 GPa at about 300 K reports $14.2 \pm 1.5 \text{ cm}^3/\text{mol}$ ($23.58 \pm 2.5 \text{ \AA}^3$), a bulk modulus of $5.0 \pm 1.5 \text{ GPa}$ and a first pressure derivative of 8.1 ± 0.9 .

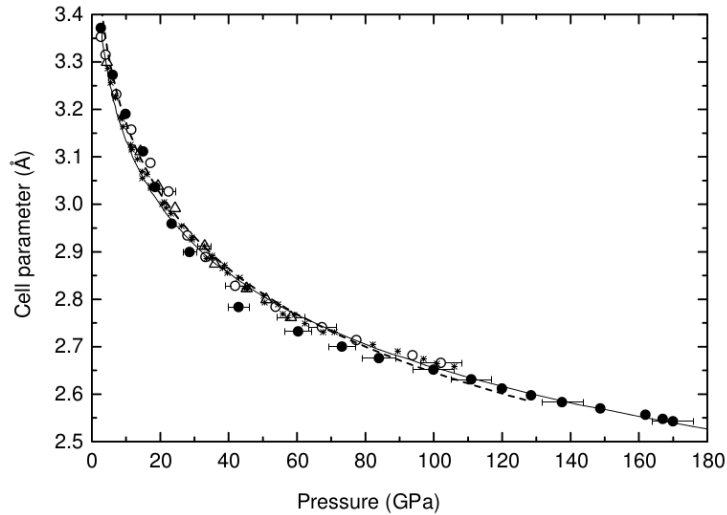


Figure 6.32: Pressure over cell parameter diagram of ice X, for references see [Loubeyre et al., 1999, Fig. 1].

Table 6.20 summarizes structural results from the PBE calculation for the distorted cell as well as experimental values.

To our knowledge, there is no experimental enthalpy difference of the VII-X transition available at the time of writing. Molecular dynamics simulations in [Baranyai et al., 2005] with SPC/E and TIP4P yielded a configurational internal

	a (Å)
PBE	3.4458
Expt. ^a	3.44
Expt. ^b	3.64
Expt. ^c	3.61

Table 6.20: Structural results for ice X for the distorted cell with 2 molecules, experimental values at several conditions (see text). ^aRef.[Hemley et al., 1987] at 300 K, extrapolated to zero pressure (BM EOS), ^bRef.[Loubeyre et al., 1999] at 300 K, extrapolated to zero pressure (Vinet EOS), ^cRef.[Ahart et al., 2011] at about 300 K, extrapolated to zero pressure (Vinet EOS).

	E (meV)	V (Å ³)	B (GPa)	B'
PBE	−461 (204)	20.46	16.02	5.73
RPA+EXX	−496 (48)	19.94	19.85	−5.86
RPA+SCHF	−646 (33)	18.38	36.67	18.23
Expt. ^a		20.4 ± 0.5	23.7 ± 0.9	4.15 ± 0.07
Expt. ^b		24.11	4.26	7.75
Expt. ^c		23.58 ± 2.5	5.0 ± 1.5	8.1 ± 0.9
MD SPC/E ^d	1172		146(2)	
MD TIP4P ^d	1118		139(2)	

Table 6.21: Results for ice X for the distorted configuration. Cohesive energy and equilibrium volume are per molecule, the energy relative to I_h , if available, is written in parentheses. Experimental values listed are at different conditions (see text). ^aRef.[Hemley et al., 1987] at 300 K, V and B' at zero pressure (BM EOS), ^bRef.[Loubeyre et al., 1999] at 300 K, V and B' at zero pressure (Vinet EOS), ^cRef.[Ahart et al., 2011] at about 300 K, V and B' at zero pressure (Vinet EOS), ^dRef.[Baranyai et al., 2005] energies at 5 K, pressures at 300 K.

energy of +113.1 kJ/mol (+1172 meV) as well as +107.9 kJ/mol (+1118 meV) at 5 K and a pressure of 146(2) GPa resp. 139(2) GPa at 300 K, which is hardly sensible indicating that SPC/E and TIP4P were used outside their regime of validity.

Ab initio calculations provide wrong prediction for the symmetric configuration when the hydrogen atom is placed exactly in the middle between the O atoms. In fact the obtained volume of 12.5 Å³ is about 40 % smaller than the one of the distorted configuration. The resulting relative energy with respect to I_h is equally odd, +850...+1000 meV. A reason for this was found in the double-well potential mentioned above. Simply placing the hydrogen in the middle leads to much too high energies.

As a workaround, a similar six-atom unit cell configuration has been chosen, in which the hydrogen atoms are positioned slightly aside the middle. Table 6.21 lists energy, volume, bulk modulus and its first pressure derivative of the distorted cell. Fig. 6.31 shows the energy-volume curves of the PBE and RPA volume scans.

Like in the high-pressure ice VIII, the experimental volumes vary a lot (with a mean value of about 22.7 Å³). Taking only the volumes from [Hemley et al., 1987] and [Ahart et al., 2011] within their tolerances, a volume of around 21 Å³ seems plausible and better matches the trend when considering all phases. An extrapolation to zero temperature probably decreases the volume by another 4 – 5 % ([Sugimura et al., 2009]) to about 20 Å³. In that case, RPA+EXX is the best match and RPA+SCHF is underestimating the volume.

Remember that, although the phase transition is very seamless and without a significant hysteresis (see also the evolution of the cell parameter with pressure in Fig. 6.32), the literature values are possibly just valid for the VII phase. Because of the seamless phase transition from ice VII to ice X, it is not always reported whether the phase transition took actually place.

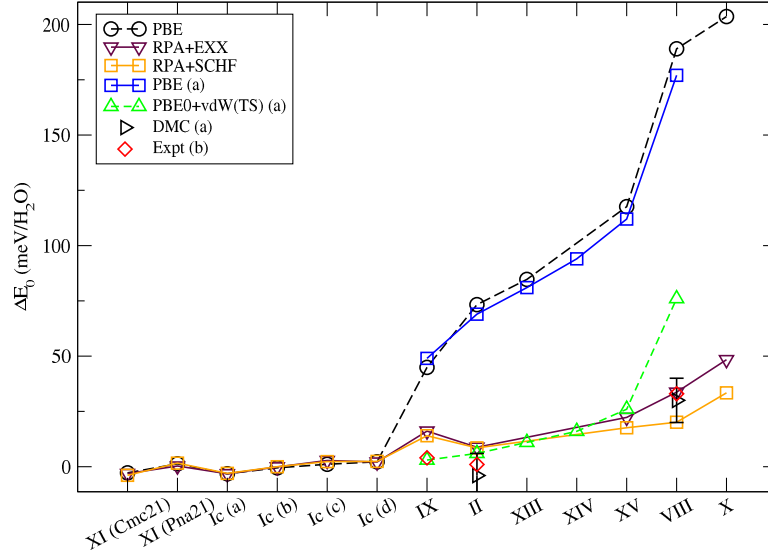
6.14 Total energy and equilibrium volume

In this section, an overview of the equilibrium volumes and energies of all phases investigated is presented.

The PBE and RPA equilibrium energies of the investigated phases are shown in Table 6.22 in combination with exact-exchange and self-consistent Hartree-Fock energies. In order to obtain the separate portions of the energy at equilibrium volume from Eq. (5.1), the RPA and HF parts were fitted using a simple polynomial fit around the equilibrium volume. Table 6.22 lists the exchange and correlation energy contributions at the equilibrium obtained from the BM EOS.

Figs. 6.33 and 6.34 show the equilibrium total energies and volumes of the investigated phases relative to ice I_h.

a) Total energies relative to ice I_h



b) Total energies relative to ice I_h with focus on the low-pressure phases

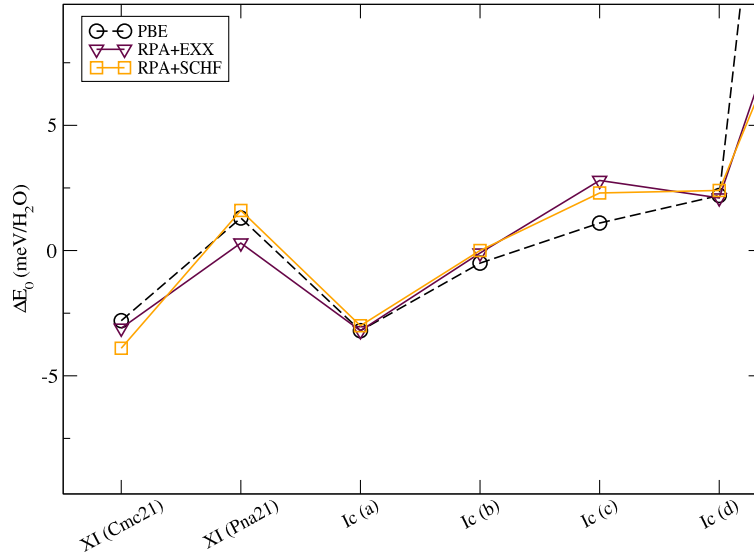
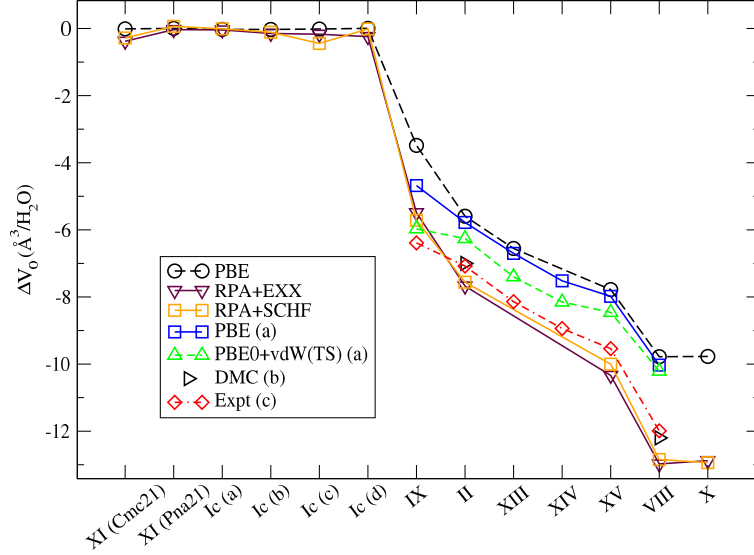


Figure 6.33: Total energies relative to ice I_h . ΔE_0 is the energy with respect to the I_h energy for the same method: $\Delta E_0 = E_0(\text{phase}) - E_0(I_h)$. ^aRef.[Santra et al., 2013], ^bRef.[Whalley, 1984].

a) Equilibrium volumes relative to ice I_h . ΔV_0 is the volume with respect to the I_h volume for the same method: $\Delta V_0 = V_0(\text{phase}) - V_0(I_h)$.



b) Equilibrium volumes for various methods ($V_0(\text{method})$) relative to the experimental volumes ($V_0(\text{expt})$), when available ([Whalley, 1984]). For XIV, no expt. data is available. The expt. value for Pna2₁, which is also not available, was assumed to be 32 Å³. The disordered I_c expt. value was used for the four ordered I_c phases. For ice X, an expt. value of 21 Å³ was assumed.

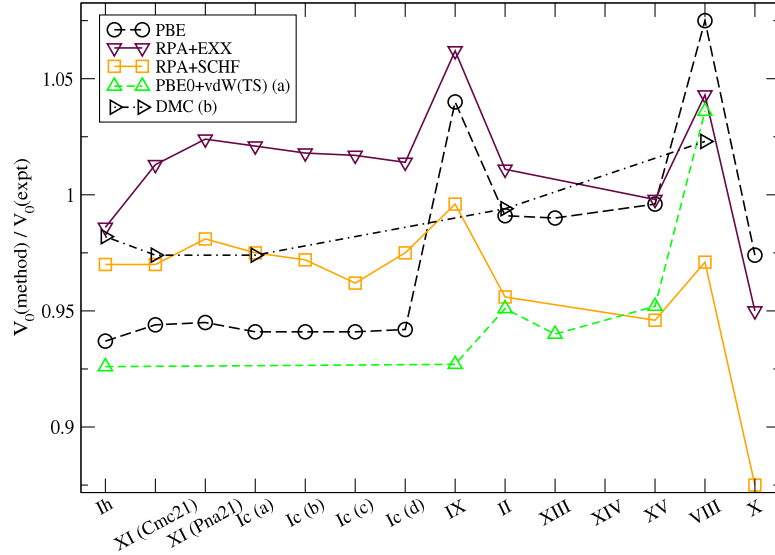


Figure 6.34: Equilibrium volumes. ^aRef.[Santra et al., 2013], ^bXI Cmc2₁ and I_c (a) from [Raza et al., 2011], I_h, II and VIII from [Santra et al., 2013], ^cRef.[Whalley, 1984].

Phase	PBE	EXX	RPA ^a	SCHF	RPA ^b
H ₂ O	-14.2324	-29.2544	-12.4263	-29.4791	-12.4263
I _h	-14.8973	-29.4664	-12.7588	-29.7996	-12.7854
I _c (a)	-14.9006	-29.4670	-12.7615	-29.8003	-12.7875
I _c (b)	-14.8978	-29.4643	-12.7612	-29.7973	-12.7874
I _c (c)	-14.8965	-29.4632	-12.7592	-29.7897	-12.7926
I _c (d)	-14.8951	-29.4623	-12.7609	-29.7987	-12.7840
XI Cmc2 ₁	-14.9002	-29.4611	-12.7672	-29.7950	-12.7935
XI Pna2 ₁	-14.8961	-29.4669	-12.7581	-29.8004	-12.7829
IX	-14.8523	-29.4194	-12.7903	-29.7519	-12.8187
II	-14.8242	-29.4228	-12.7937	-29.7474	-12.8292
XIII	-14.8126				
XV	-14.7798	-29.3872	-12.8158	-29.7156	-12.8518
VIII	-14.7083	-29.3451	-12.8467	-29.6662	-12.8985
X	-14.6938	-29.3345	-12.8423	-29.6477	-12.9036

Table 6.22: Energy contribution to the total energy in eV from PBE, RPA+EXX and RPA+SCHF calculations. ^{ab}The RPA contribution to the total energy evaluated for the positions minimizing the EXX+RPA energy-volume curve, respectively the SCHF+RPA energy-volume curve.

At low pressures, RPA and PBE yield the same relative energies. The cubic ordered ice I_c(a) matches that of the hexagonal ordered ice XI Cmc2₁, which makes a lot of sense. The disordered cubic ice is most likely the average of the ordered structures. The ferroelectric I_c(a) is more stable than the antiferroelectric I_c(d) phase.

Due to missing vdW interaction, PBE shows a steep increase in energy as the volume decreases. RPA+EXX and RPA+SCHF behave very similarly. They are in excellent agreement with DMC, when DMC data is available.

Ice II is a little bit too unstable compared to experiment and DMC, however, the origin is unclear. Ice VIII is in excellent agreement between RPA and DMC and in better agreement than PBE+vdW.

PBE volumes are too small for low-pressure phases and vdW correction makes it worse. For high-pressure phases PBE is quite good and vdW correction makes it even better.

RPA+EXX yield too large volumes for all phases. This behavior is also true for other materials, in particular vdW bonded systems ([Ren et al., 2013]). RPA+SCHF, on the other hand, is consistently too large.

When the relative volume change compared to I_h is considered, both do very well.

Chapter 7

Infrared intensities

The understanding of infrared spectra of water and ice is of great importance for various scientific fields like biology, chemistry, geology and astronomy. Different aggregation states of water and different phases of ice show different IR spectra. This fact enables the remote detection of water and ice especially on planets. Molecular vibrations, which are directly related to the spectral features, are of importance in chemical-physical, atmospheric, geophysical and other processes.

Ab initio calculations of [Profeta and Scandolo, 2011] showed that many features of the IR spectrum of I_h may not be covered by simple models: In GGA DFPT calculations, they showed that LO-TO splitting and the proton disorder of ice I_h as well as an *ab initio* description of the electronic response is required to interpret the available experimental data. Long-range Coulomb interactions of induced dipoles are required to observe all details of the spectrum. Absorption above 300cm^{-1} may be accessible only through the use of *ab initio* force constants and by not neglecting anharmonic effects.

In this work, infrared intensities have been calculated for the cubic I_c phases, the hexagonal phase I_h (Section 6.4) and two XI phases with space groups $\text{Cmc}2_1$ (Section 6.5) and $\text{Pna}2_1$ (Section 6.6). For a more accurate comparison the 8 molecule I_c supercells (Figs. 7.1-7.4) were used instead of the irreducible cells obtained by VASP from symmetry operations (Figs. 6.10-6.13).

In [Bertie, 1967], H_2O -ices I_c and I_h showed IR peaks at 222 cm^{-1} at 168 K and 229 cm^{-1} at 100 K ($\pm 20\text{ K}$ for both temperatures and a missing correction for reflection at the interfaces is mentioned in [Warren, 1984, p. 1212]). They found no detectable difference in the far-IR range peaks for I_c and I_h .

In [Bertie and Jacobs, 1977] for the first time, significant differences between I_h and I_c were observed for H_2O and D_2O at $4.3 \pm 0.1\text{ K}$. Among other features, peaks at 233.7 cm^{-1} (I_h) and 233.0 cm^{-1} (I_c) were detected (Fig. 7.5).

DFPT calculations in [Profeta and Scandolo, 2011] provide an extensive first-principles view of features not gained by simpler models. Fig. 7.6 shows the IR spectrum of the proton disordered hexagonal ice, which was obtained by summing over the proton ordered phases. The method used in the present work did not make use of LO-TO splitting, therefore the I_h peaks in this work, 244.6 cm^{-1} (vdW-DFT) and 233.5 cm^{-1} (GGA), should best be compared with the peak at 238 cm^{-1} of the thick dashed line in Fig. 7.6.

Figs. 7.7-7.13 show the H_2O spectral densities obtained from finite differences (optPBE-vdW) and linear response (PBE potential) (see Chap. 5.3) as well

as the results from molecular dynamics simulations (Geiger et al. 2013, not yet published). Linear response and optPBE-vdW more or less yield the same infrared intensities with features shifted along the frequency scale. With respect to MD simulations, the curves are shifted and scaled along the frequency axis, however, the features are similar.

The different proton configurations of I_h and I_c lead to remarkably different intensity curves, a point that was also found by [Profeta and Scandolo, 2011].

The most stable proton order variant of the proton disordered I_h , ice XI Cmc2₁, has different features than I_h : For example, a peak at 150 cm⁻¹, found in experimental data, is not found in XI Cmc2₁ but in the second most stable hexagonal ice XI Pna2₁.

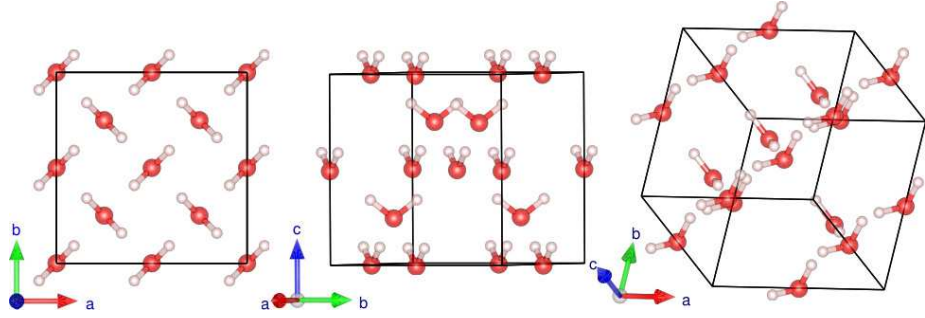


Figure 7.1: Ice I_c (ord. a) structure.

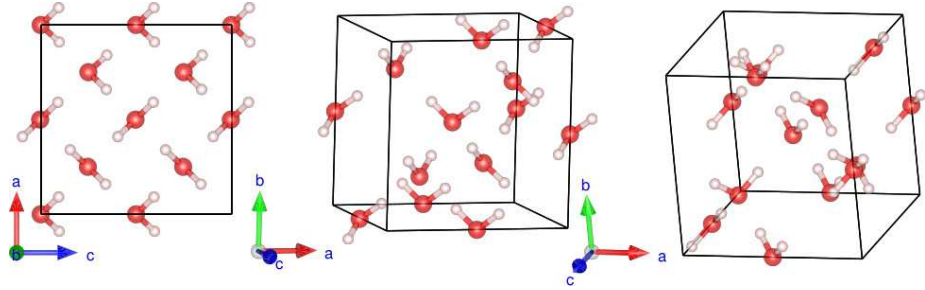


Figure 7.2: Ice I_c (ord. b) structure.

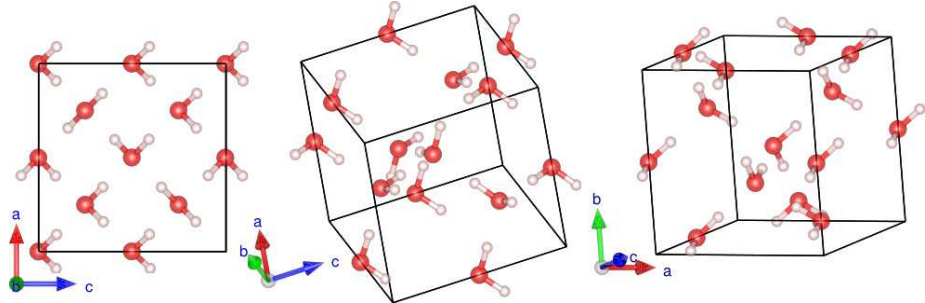


Figure 7.3: Ice I_c (ord. c) structure.

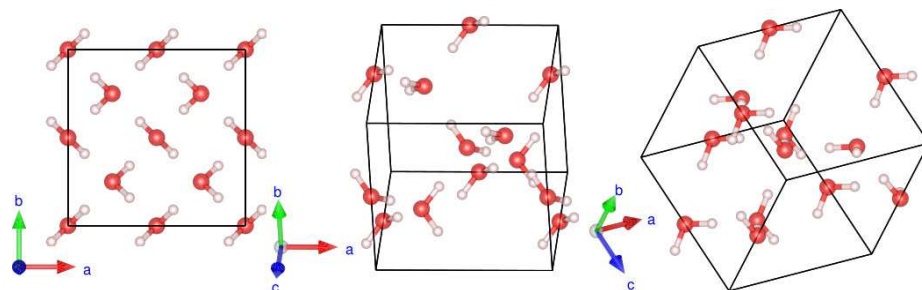


Figure 7.4: Ice I_c (ord. d) structure.

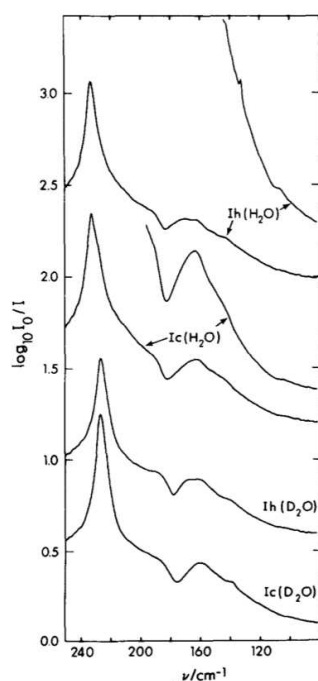


FIG. 2. Far-infrared spectra of ice I at 4.3°K. The spectra of ice Ih (H_2O), ice Ic (H_2O), and ice Ih (D_2O) have been raised by 1.75, 1.0, and 0.5 units, respectively. The sharp feature at 132 cm^{-1} in the top curve is due to crystal quartz windows that were used for that spectrum only.

Figure 7.5: Far-IR intensities from [Bertie and Jacobs, 1977].

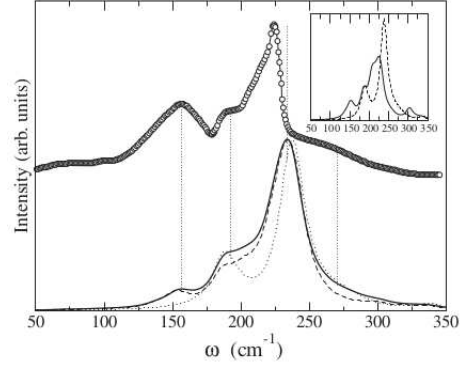


FIG. 2. Open circles represent the experimental spectrum from Refs. 10 and 13. The solid bold line represents $\epsilon''(\omega)$ calculated summing over the 17 different phases and integrating the LO-TO splitting over \mathbf{q} . The thick dashed line represents $\epsilon''(\omega)$ calculated summing over the 17 different phases without LO-TO splitting. The dotted line represents $\epsilon''(\omega)$ calculated integrating the LO-TO splitting over \mathbf{q} , but only for the ground state $Cmc2_1$. Inset: IR spectrum of the two lowest energy structures (see text).

Figure 7.6: Far-IR intensities from [Profeta and Scandolo, 2011].

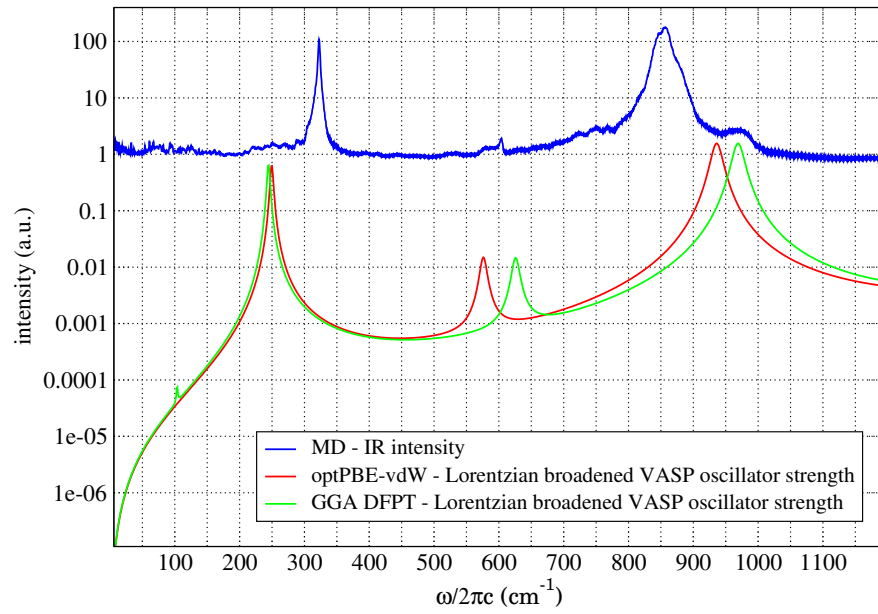


Figure 7.7: Ice I_c (ord. a) IR spectrum.

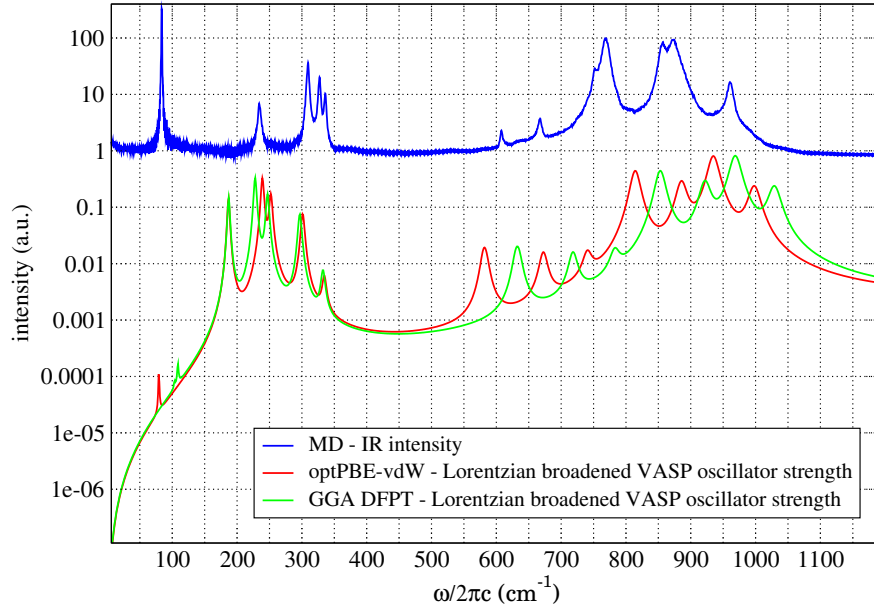


Figure 7.8: Ice I_c (ord. b) IR spectrum.

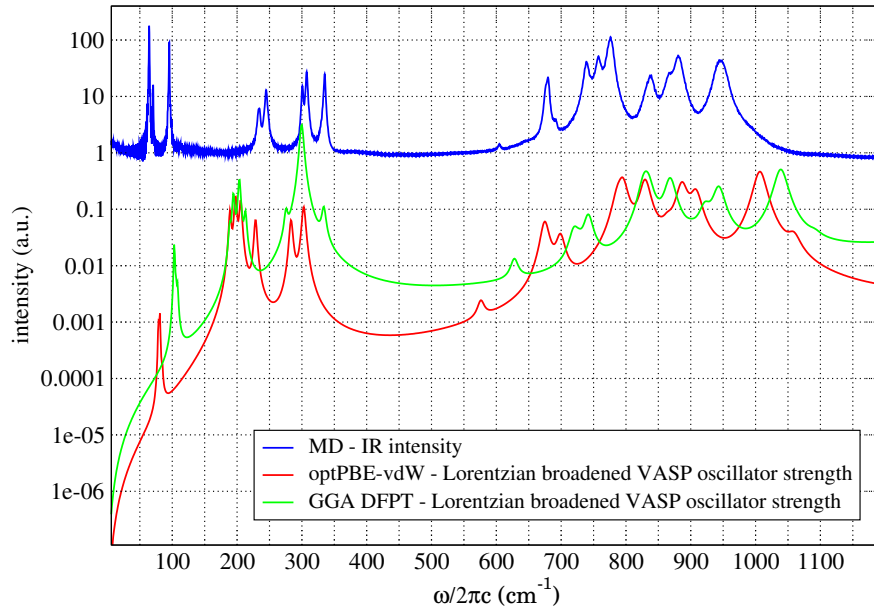


Figure 7.9: Ice I_c (ord. c) IR spectrum.

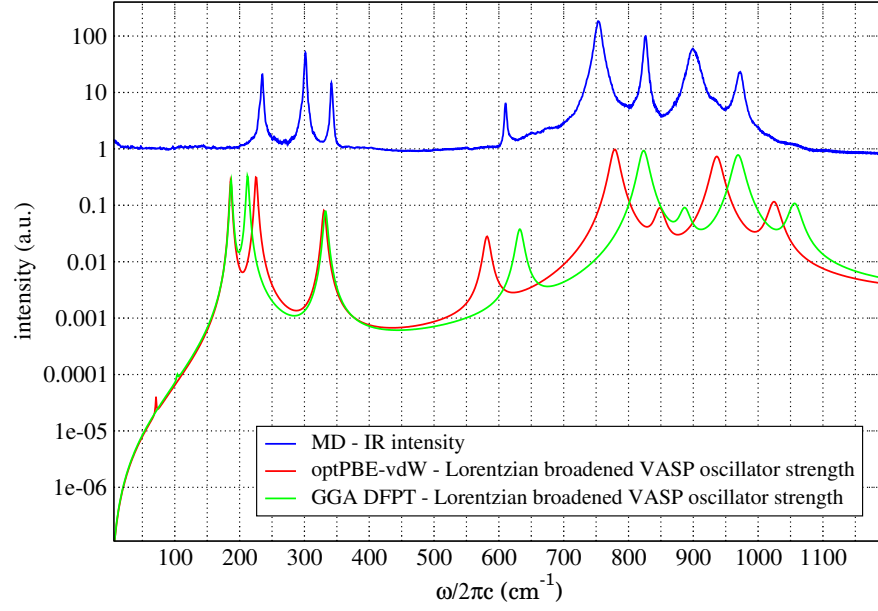


Figure 7.10: Ice I_c (ord. d) IR spectrum.

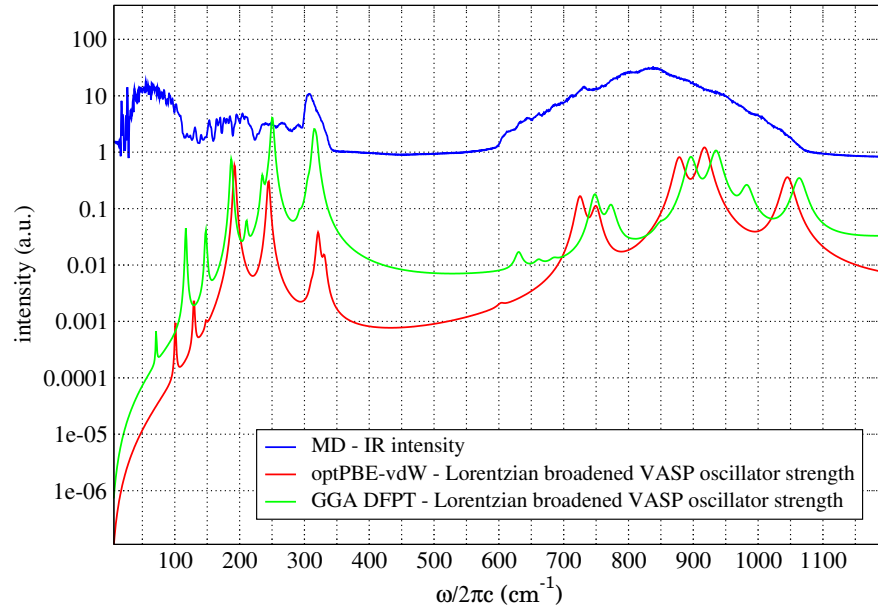


Figure 7.11: Ice I_h IR spectrum.

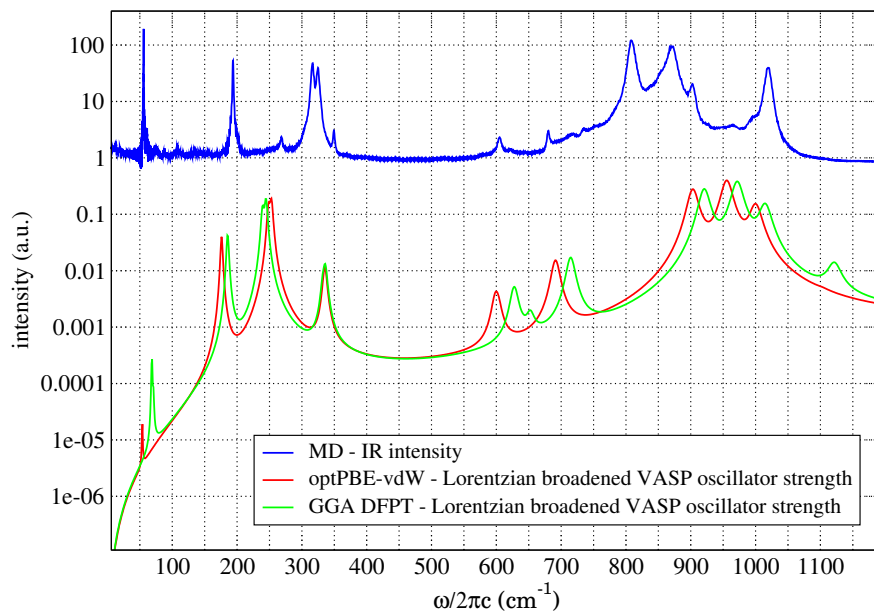


Figure 7.12: Ice XI $Cmc2_1$ IR spectrum.

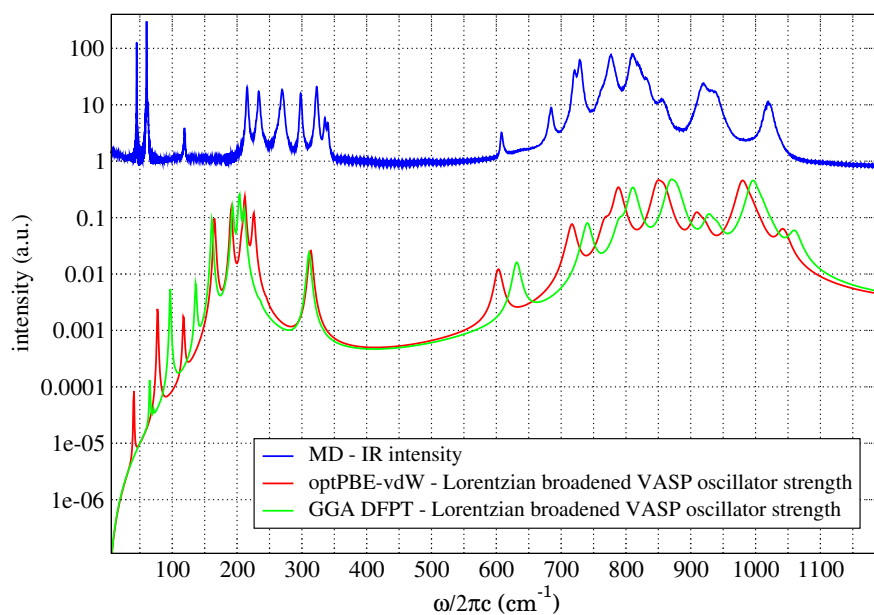


Figure 7.13: Ice XI $Pna2_1$ IR spectrum.

Chapter 8

Summary and conclusions

Several water ice phases have been investigated regarding ground state energies, lattice parameters, pressures and bulk moduli.

We reviewed, with respect to reasonableness, and compared our results with previous experimental and theoretical results. DMC and PBE0+vdW^{TS} were taken mainly from [Santra et al., 2011] and [Santra et al., 2013] and others, experimental values from [Whalley, 1984], [Handa et al., 1988, Table 4] and others.

MC simulations from various sources predict the volumes in good agreement with RPA, DMC and experiments.

PBE0+vdW^{TS} ([Santra et al., 2011]) at low- to mid-pressures, underestimates the volume due to overestimated vdW interaction. Overall, PBE0+vdW^{TS} performs worse than RPA and DMC but better than PBE.

We find that PBE, due to missing vdW interactions, strongly underestimates the binding energy on high-pressure phases. However, PBE can keep up with RPA at low-pressure phases which could be due to other effects overestimating the energy at those phases. In particular, the self interaction error, which is cancelled exactly in HF theory, is only incomplete cancelled in DFT and leads to insufficient repulsion compared with HF exchange. This however, works better for some phases than for other phases.

RPA, combined with both, EXX and SCHF, yields reasonable results over the entire pressure range and compared to experiments and DMC ([Santra et al., 2011]), only slightly underestimates the volumes relative to I_h on medium and high pressures. An almost constant volume shift was shown between RPA+EXX and RPA+SCHF over the entire pressure range which is reflected in almost identical relative volume curves.

SCHF yields more contracted orbitals because electrons experience a $1/r$ potential at large distances from ions, whereas DFT potentials (EXX) fall off much too fast, essentially exponential. The contracted orbitals lead to less Pauli repulsion. SCHF volumes therefore are more contracted and the cohesive energy is increased as opposed to EXX calculations.

The symmetrical ice X showed a major discrepancy in volume and energy. Both, PBE and RPA, were not able to correctly handle the proton tunneling effects of double-well potential and so a slightly distorted configuration was chosen.

Bibliography

- Muhtar Ahart, Maddury Somayazulu, Stephen A Gramsch, Reinhard Boehler, Ho-kwang Mao, and Russell J Hemley. Brillouin scattering of H₂O ice to megabar pressures. *The Journal of Chemical Physics*, 134(12):124517–124517–6, March 2011. ISSN 00219606. doi: doi:10.1063/1.3557795. URL http://jcp.aip.org/resource/1/jcpsa6/v134/i12/p124517_s1.
- K. Aoki, H. Yamawaki, M. Sakashita, and H. Fujihisa. Infrared absorption study of the hydrogen-bond symmetrization in ice to 110 GPa. *Physical Review B*, 54(22):15673–15677, December 1996. doi: 10.1103/PhysRevB.54.15673. URL <http://link.aps.org/doi/10.1103/PhysRevB.54.15673>.
- J. L. Aragones, E. G. Noya, J. L. F. Abascal, and C. Vega. Properties of ices at 0 K: A test of water models. *The Journal of Chemical Physics*, 127(15):154518, 2007. ISSN 00219606. doi: 10.1063/1.2774986. URL <http://link.aip.org/link/JCPSA6/v127/i15/p154518/s1&Agg=doi>.
- Neil W Ashcroft and N. David Mermin. *Solid state physics*. Holt, Rinehart and Winston, New York, 1976. ISBN 0030839939 9780030839931 0030493463 9780030493461.
- Andras Baranyai, Albert Bartok, and Ariel A. Chialvo. Computer simulation of the 13 crystalline phases of ice. *The Journal of Chemical Physics*, 123(5):054502, 2005. ISSN 00219606. doi: 10.1063/1.1989313. URL <http://link.aip.org/link/JCPSA6/v123/i5/p054502/s1&Agg=doi>.
- Stefano Baroni, Stefano de Gironcoli, and Andrea Dal Corso. Phonons and related crystal properties from density-functional perturbation theory. *Reviews of Modern Physics*, 73(2):515–562, July 2001. ISSN 0034-6861, 1539-0756. doi: 10.1103/RevModPhys.73.515. URL <http://link.aps.org/doi/10.1103/RevModPhys.73.515>.
- H. J. C. Berendsen, J. R. Grigera, and T. P. Straatsma. The missing term in effective pair potentials. *The Journal of Physical Chemistry*, 91(24):6269–6271, November 1987. ISSN 0022-3654, 1541-5740. doi: 10.1021/j100308a038. URL <http://pubs.acs.org/doi/abs/10.1021/j100308a038>.
- J. E. Bertie. Optical spectra of orientationally disordered crystals. II. infrared spectrum of ice Ih and ice Ic from 360 to 50 cm⁻¹. *The Journal of Chemical Physics*, 46(4):1271, 1967. ISSN 00219606. doi: 10.1063/1.1840845. URL <http://link.aip.org/link/?JCP/46/1271/1&Agg=doi>.

- John E. Bertie and Stephen M. Jacobs. Far-infrared absorption by ices ih and ic at 4.3 k and the powder diffraction pattern of ice ic. *The Journal of Chemical Physics*, 67(6):2445, 1977. ISSN 00219606. doi: 10.1063/1.435218. URL <http://link.aip.org/link/JCPSA6/v67/i6/p2445/s1&Agg=doi>.
- J. M. Besson, M. Kobayashi, T. Nakai, S. Endo, and Ph. Pruzan. Pressure dependence of raman linewidths in ices VII and VIII. *Physical Review B*, 55(17): 11191–11201, May 1997. ISSN 0163-1829, 1095-3795. doi: 10.1103/PhysRevB.55.11191. URL <http://link.aps.org/doi/10.1103/PhysRevB.55.11191>.
- T Björkman, A Gulans, A V Krasheninnikov, and R M Nieminen. Are we van der waals ready? *Journal of Physics: Condensed Matter*, 24(42):424218, October 2012. ISSN 0953-8984, 1361-648X. doi: 10.1088/0953-8984/24/42/424218. URL <http://stacks.iop.org/0953-8984/24/i=42/a=424218?key=crossref.bb38f55062bb4151a80e804f5a0f950f>.
- P. E. Blöchl. Projector augmented-wave method. *Physical Review B*, 50(24):17953–17979, December 1994. ISSN 0163-1829, 1095-3795. doi: 10.1103/PhysRevB.50.17953. URL <http://link.aps.org/doi/10.1103/PhysRevB.50.17953>.
- Max Born. *Dynamical theory of crystal lattices*. Oxford classic texts in the physical sciences. Clarendon Press ; Oxford University Press, Oxford : New York, 1988. ISBN 0198503695.
- Klaus Capelle. A bird’s-eye view of density-functional theory, November 2006. URL <http://arxiv.org/abs/cond-mat/0211443v5>.
- Martin Chaplin. Water phase diagram, 2012. URL <http://www.lsbu.ac.uk/water/phase.html>.
- Martin Chaplin. Hydrogen bonding in water, 2013. URL <http://www.lsbu.ac.uk/water/hbond.html>.
- Birkbeck College. High-resolution space group diagrams and tables, 1999. URL <http://img.chem.ucl.ac.uk/sgp/large/sgp.htm>.
- Ernest R. Davidson and Keiji Morokuma. A proposed antiferroelectric structure for proton ordered ice ih. *The Journal of Chemical Physics*, 81(8):3741, 1984. ISSN 00219606. doi: 10.1063/1.448101. URL <http://link.aip.org/link/JCPSA6/v81/i8/p3741/s1&Agg=doi>.
- Michael de Podesta. *physicsofmatter*, 2013. URL <http://www.physicsofmatter.com/NotTheBook/Talks/Ice/Ice.html>.
- John Dobson. How reliable is the RPA for van der waals (dispersion) interactions?, 2010. URL https://wiki.lct.jussieu.fr/workshop/images/6/64/Dobson_paris_2010.pdf.
- David S. Eisenberg. *The structure and properties of water*. Oxford classic texts in the physical sciences. Clarendon Press ; Oxford University Press, Oxford : New York, 2005. ISBN 9780198570264.
- C Fiolhais, F Nogueira, and M Marques. *A Primer in density functional theory*. Springer, Berlin [etc.], 2003. ISBN 3540030832 9783540030836.

- Richard Fitzpatrick. Quantum mechanics: An intermediate level course, December 2006. URL <http://farside.ph.utexas.edu/teaching/qmech/lectures/lectures.html>.
- A. D. Fortes, I. G. Wood, M. Alfredsson, L. Vočadlo, and K. S. Knight. The incompressibility and thermal expansivity of d 2 o ice II determined by powder neutron diffraction. *Journal of Applied Crystallography*, 38(4):612–618, July 2005. ISSN 0021-8898. doi: 10.1107/S0021889805014226. URL <http://scripts.iucr.org/cgi-bin/paper?aj5041>.
- Hiroshi Fukazawa, Akinori Hoshikawa, Hiroki Yamauchi, Yasuo Yamaguchi, and Yoshinobu Ishii. Formation and growth of ice XI: a powder neutron diffraction study. *Journal of Crystal Growth*, 282(1-2):251–259, August 2005. ISSN 00220248. doi: 10.1016/j.jcrysgro.2005.04.105. URL <http://linkinghub.elsevier.com/retrieve/pii/S0022024805005828>.
- P. H. Gammon, H. Kiefte, and M. J. Clouter. Elastic constants of ice samples by brillouin spectroscopy. *J. Phys. Chem.*, 87(21):4025–4029, 1983. ISSN 0022-3654. doi: 10.1021/j100244a004. URL <http://dx.doi.org/10.1021/j100244a004>.
- Philipp Geiger. E-mail correspondence ”Re: ice configurationen”, December 2011.
- J. A. Ghormley. Enthalpy changes and heat-capacity changes in the transformations from high-surface-area amorphous ice to stable hexagonal ice. *The Journal of Chemical Physics*, 48(1):503, 1968. ISSN 00219606. doi: 10.1063/1.1667954. URL <http://link.aip.org/link/?JCP/48/503/1&Agg=doi>.
- Ph. Ghosez, J.-P. Michenaud, and X. Gonze. Dynamical atomic charges: The case of ABO₃ compounds. *Physical Review B*, 58(10):6224–6240, 1998. doi: 10.1103/PhysRevB.58.6224. URL <http://link.aps.org/doi/10.1103/PhysRevB.58.6224>.
- Paolo Giannozzi and Stefano Baroni. Vibrational and dielectric properties of c60 from density-functional perturbation theory. *The Journal of Chemical Physics*, 100(11):8537, 1994. ISSN 00219606. doi: 10.1063/1.466753. URL <http://link.aip.org/link/JCPA6/v100/i11/p8537/s1&Agg=doi>.
- A. F. Goncharov, V. V. Struzhkin, M. S. Somayazulu, R. J. Hemley, and H. K. Mao. Compression of ice to 210 gigapascals: Infrared evidence for a symmetric hydrogen-bonded phase. *Science*, 273(5272):218–220, July 1996. ISSN 0036-8075, 1095-9203. doi: 10.1126/science.273.5272.218. URL <http://www.sciencemag.org/cgi/doi/10.1126/science.273.5272.218>.
- D. R. Hamann. H₂O hydrogen bonding in density-functional theory. *Physical Review B*, 55(16):R10157–R10160, April 1997. doi: 10.1103/PhysRevB.55.R10157. URL <http://link.aps.org/doi/10.1103/PhysRevB.55.R10157>.
- Y. Paul Handa, D. D. Klug, and Edward Whalley. Difference in energy between cubic and hexagonal ice. *The Journal of Chemical Physics*, 84(12):7009, 1986a. ISSN 00219606. doi: 10.1063/1.450622. URL <http://link.aip.org/link/JCPA6/v84/i12/p7009/s1&Agg=doi>.

- Y. Paul Handa, Osamu Mishima, and Edward Whalley. High-density amorphous ice. III. thermal properties. *The Journal of Chemical Physics*, 84(5):2766, 1986b. ISSN 00219606. doi: 10.1063/1.450301. URL <http://link.aip.org/link/JCPSA6/v84/i5/p2766/s1&Agg=doi>.
- Y. Paul Handa, D. D. Klug, and Edward Whalley. Energies of the phases of ice at low temperature and pressure relative to ice Ih. *Canadian Journal of Chemistry*, 66(4):919–924, April 1988. ISSN 0008-4042, 1480-3291. doi: 10.1139/v88-156. URL <http://www.nrcresearchpress.com/doi/abs/10.1139/v88-156>.
- Judith Harl. *The linear response function in density functional theory*. PhD thesis, Universität Wien, 2008. URL <http://othes.univie.ac.at/2622/>.
- N.M. Harrison. An introduction to density functional theory, 2002. URL http://www.ch.ic.ac.uk/harrison/Teaching/DFT_NATO.pdf.
- R. J. Hemley, A. P. Jephcoat, H. K. Mao, C. S. Zha, L. W. Finger, and D. E. Cox. Static compression of H₂O-ice to 128 GPa (1.28 mbar). , *Published online: 31 December 1987*; | doi:10.1038/330737a0, 330(6150):737–740, December 1987. doi: 10.1038/330737a0. URL <http://www.nature.com/nature/journal/v330/n6150/abs/330737a0.html>.
- K. R. Hirsch and W. B. Holzapfel. Effect of high pressure on the raman spectra of ice VIII and evidence for ice x. *The Journal of Chemical Physics*, 84(5):2771, 1986. ISSN 00219606. doi: 10.1063/1.450302. URL <http://link.aip.org/link/JCPSA6/v84/i5/p2771/s1&Agg=doi>.
- Tomas K. Hirsch and Lars Ojamäe. Quantum-chemical and force-field investigations of ice Ih: Computation of proton-ordered structures and prediction of their lattice energies. *J. Phys. Chem. B*, 108(40):15856–15864, 2004. ISSN 1520-6106. doi: 10.1021/jp048434u. URL <http://dx.doi.org/10.1021/jp048434u>.
- Peter Victor Hobbs. *Ice physics*. Oxford classic texts in the physical sciences. Oxford University Press, New York, 1974. ISBN 9780199587711.
- P. Hohenberg and W. Kohn. Inhomogeneous electron gas. *Physical Review*, 136(3B):B864–B871, November 1964. doi: 10.1103/PhysRev.136.B864. URL <http://link.aps.org/doi/10.1103/PhysRev.136.B864>.
- Rachel Howe and R. W. Whitworth. A determination of the crystal structure of ice XI. *The Journal of Chemical Physics*, 90(8):4450, 1989. ISSN 00219606. doi: 10.1063/1.456630. URL <http://link.aip.org/link/JCPSA6/v90/i8/p4450/s1&Agg=doi>.
- S. M. Jackson, V. M. Nield, R. W. Whitworth, M. Oguro, and C. C. Wilson. Single-crystal neutron diffraction studies of the structure of ice XI. *The Journal of Physical Chemistry B*, 101(32):6142–6145, August 1997. ISSN 1520-6106, 1520-5207. doi: 10.1021/jp9632551. URL <http://pubs.acs.org/doi/abs/10.1021/jp9632551>.
- G. P. Johari. An interpretation for the thermodynamic features of ice Ih - ice XI transformation. *The Journal of Chemical Physics*, 109(21):9543, 1998. ISSN 00219606. doi: 10.1063/1.477616. URL <http://link.aip.org/link/JCPSA6/v109/i21/p9543/s1&Agg=doi>.

- James D. Jorgensen, R. A. Beyerlein, Noboru Watanabe, and T. G. Worlton. Structure of D₂O ice VIII from in situ powder neutron diffraction. *The Journal of Chemical Physics*, 81(7):3211, 1984. ISSN 00219606. doi: 10.1063/1.448027. URL <http://link.aip.org/link/JCPSA6/v81/i7/p3211/s1&Agg=doi>.
- B. Kamb. Ice. II. a proton-ordered form of ice. *Acta Crystallographica*, 17(11):1437–1449, November 1964a. ISSN 0365110X. doi: 10.1107/S0365110X64003553. URL <http://scripts.iucr.org/cgi-bin/paper?S0365110X64003553>.
- B. Kamb. Ice VII, the densest form of ice. *Proceedings of the National Academy of Sciences*, 52(6):1433–1439, December 1964b. ISSN 0027-8424, 1091-6490. doi: 10.1073/pnas.52.6.1433. URL <http://www.pnas.org/cgi/doi/10.1073/pnas.52.6.1433>.
- Jiří Klimeš, David R Bowler, and Angelos Michaelides. Chemical accuracy for the van der waals density functional. *Journal of Physics: Condensed Matter*, 22(2):022201, January 2010. ISSN 0953-8984, 1361-648X. doi: 10.1088/0953-8984/22/2/022201. URL <http://stacks.iop.org/0953-8984/22/i=2/a=022201?key=crossref.0bf365af33d14feb5718d41b4bc4b5d9>.
- Chris Knight and Sherwin J. Singer. Prediction of a phase transition to a hydrogen bond ordered form of ice VI. *The Journal of Physical Chemistry B*, 109(44):21040–21046, November 2005. ISSN 1520-6106, 1520-5207. doi: 10.1021/jp0540609. URL <http://pubs.acs.org/doi/abs/10.1021/jp0540609>.
- Chris Knight and Sherwin J Singer. A reexamination of the ice III/IX hydrogen bond ordering phase transition. *The Journal of Chemical Physics*, 125(6):064506–064506–10, August 2006. ISSN 00219606. doi: doi:10.1063/1.2209230. URL http://jcp.aip.org/resource/1/jcpsa6/v125/i6/p064506_s1.
- Chris Knight and Sherwin J. Singer. Hydrogen bond ordering in ice v and the transition to ice XIII. *The Journal of Chemical Physics*, 129(16):164513, 2008. ISSN 00219606. doi: 10.1063/1.2991297. URL <http://link.aip.org/link/JCPSA6/v129/i16/p164513/s1&Agg=doi>.
- W. Kohn and L. J. Sham. Self-consistent equations including exchange and correlation effects. *Physical Review*, 140(4A):A1133–A1138, November 1965. ISSN 0031-899X, 1536-6065. doi: 10.1103/PhysRev.140.A1133. URL <http://link.aps.org/doi/10.1103/PhysRev.140.A1133>.
- G. Kresse. From ultrasoft pseudopotentials to the projector augmented-wave method. *Physical Review B*, 59(3):1758–1775, January 1999. ISSN 1098-0121, 1095-3795. doi: 10.1103/PhysRevB.59.1758. URL <http://link.aps.org/doi/10.1103/PhysRevB.59.1758>.
- G. Kresse and J. Furthmüller. Efficiency of ab-initio total energy calculations for metals and semiconductors using a plane-wave basis set. *Computational Materials Science*, 6(1):15–50, July 1996. ISSN 09270256. doi: 10.1016/0927-0256(96)00008-0. URL <http://linkinghub.elsevier.com/retrieve/pii/0927025696000080>.

- G. Kresse and J. Hafner. Ab initio molecular dynamics for open-shell transition metals. *Physical Review B*, 48(17):13115–13118, November 1993. ISSN 0163-1829, 1095-3795. doi: 10.1103/PhysRevB.48.13115. URL <http://link.aps.org/doi/10.1103/PhysRevB.48.13115>.
- W. F Kuhs, J. L Finney, C. Vettier, and D. V Bliss. Structure and hydrogen ordering in ices VI, VII, and VIII by neutron powder diffraction. *The Journal of Chemical Physics*, 81(8):3612–3623, October 1984. ISSN 00219606. doi: doi:10.1063/1.448109. URL http://jcp.aip.org/resource/1/jcpsa6/v81/i8/p3612_s1.
- Jer-Lai Kuo and Werner F. Kuhs. A first principles study on the structure of ice-VI: static distortion, molecular geometry, and proton ordering. *The Journal of Physical Chemistry B*, 110(8):3697–3703, March 2006. ISSN 1520-6106, 1520-5207. doi: 10.1021/jp055260n. URL <http://pubs.acs.org/doi/abs/10.1021/jp055260n>.
- M. S. Kushwaha. The bond-bending force model (BBFM) for phonons in beta-SiC. *physica status solidi (b)*, 111(1):337–340, May 1982. ISSN 03701972, 15213951. doi: 10.1002/pssb.2221110138. URL <http://doi.wiley.com/10.1002/pssb.2221110138>.
- Sam J La Placa, Walter C Hamilton, Barclay Kamb, and Anand Prakash. On a nearly proton-ordered structure for ice IX. *The Journal of Chemical Physics*, 58(2):567–580, January 1973. ISSN 00219606. doi: doi:10.1063/1.1679238. URL http://jcp.aip.org/resource/1/jcpsa6/v58/i2/p567_s1.
- A. J Leadbetter, R. C Ward, J. W Clark, P. A Tucker, T. Matsuo, and H. Suga. The equilibrium low-temperature structure of ice Ih. *The Journal of Chemical Physics*, 82(1):424–428, January 1985. ISSN 00219606. doi: doi:10.1063/1.448763. URL http://jcp.aip.org/resource/1/jcpsa6/v82/i1/p424_s1.
- Kyuhoo Lee, Éamonn D. Murray, Lingzhu Kong, Bengt I. Lundqvist, and David C. Langreth. Higher-accuracy van der waals density functional. *Physical Review B*, 82(8), August 2010. ISSN 1098-0121, 1550-235X. doi: 10.1103/PhysRevB.82.081101. URL <http://link.aps.org/doi/10.1103/PhysRevB.82.081101>.
- M. Levy. Universal variational functionals of electron densities, first-order density matrices, and natural spin-orbitals and solution of the v-representability problem. *Proceedings of the National Academy of Sciences*, 76(12):6062–6065, December 1979. ISSN 0027-8424, 1091-6490. doi: 10.1073/pnas.76.12.6062. URL <http://www.pnas.org/cgi/doi/10.1073/pnas.76.12.6062>.
- J.-C. Li, V.M. Nield, and S.M. Jackson. Spectroscopic measurements of ice XI. *Chemical Physics Letters*, 241(4):290–294, July 1995. ISSN 00092614. doi: 10.1016/0009-2614(95)00660-V. URL <http://linkinghub.elsevier.com/retrieve/pii/000926149500660V>.
- Christina M. B. Line and R. W. Whitworth. A high resolution neutron powder diffraction study of D2O ice XI. *The Journal of Chemical Physics*, 104:10008, 1996. ISSN 00219606. doi: 10.1063/1.471745. URL <http://link.aip.org/link/JCPSA6/v104/i24/p10008/s1&Agg=doi>.

- C. Lobban, J. L. Finney, and W. F. Kuhs. The p–T dependency of the ice II crystal structure and the effect of helium inclusion. *The Journal of Chemical Physics*, 117(8):3928–3934, August 2002. ISSN 00219606. doi: doi:10.1063/1.1495837. URL http://jcp.aip.org/resource/1/jcpsa6/v117/i8/p3928_s1.
- J. D. Londono, W. F. Kuhs, and J. L. Finney. Neutron diffraction studies of ices III and IX on under-pressure and recovered samples. *The Journal of Chemical Physics*, 98(6):4878, 1993. ISSN 00219606. doi: 10.1063/1.464942. URL <http://link.aip.org/link/JCPSA6/v98/i6/p4878/s1&Agg=doi>.
- P. Loubeyre, R. LeToullec, E. Wolanin, M. Hanfland, and D. Husermann. Modulated phases and proton centring in ice observed by x-ray diffraction up to 170 GPa. *Nature*, 1999. doi: 10.1038/17300. URL <http://www.nature.com/nature/journal/v397/n6719/abs/397503a0.html>.
- Richard M. Martin. *Electronic structure: basic theory and practical methods*. Cambridge University Press, Cambridge, UK ; New York, 2004. ISBN 0521782856.
- Maria Martin-Conde, Luis G. MacDowell, and Carlos Vega. Computer simulation of two new solid phases of water: Ice XIII and ice XIV. *The Journal of Chemical Physics*, 125(11):116101, 2006. ISSN 00219606. doi: 10.1063/1.2354150. URL <http://link.aip.org/link/JCPSA6/v125/i11/p116101/s1&Agg=doi>.
- Michael Maskos. Intermolekulare kräfte, 2009. URL www.uni-mainz.de/FB/Chemie/AK-Maskos/Dateien/PCIII-13.pdf. Johannes Gutenberg-Universität Mainz.
- Benjamin J. Murray. Enhanced formation of cubic ice in aqueous organic acid droplets. *Environmental Research Letters*, 3(2):025008, April 2008. ISSN 1748-9326. doi: 10.1088/1748-9326/3/2/025008. URL <http://stacks.iop.org/1748-9326/3/i=2/a=025008?key=crossref.6a2925c63e836d8ae4c2d1d1e541ebf7>.
- Benjamin J. Murray and Allan K. Bertram. Formation and stability of cubic ice in water droplets. *Physical Chemistry Chemical Physics*, 8(1):186, 2006. ISSN 1463-9076, 1463-9084. doi: 10.1039/b513480c. URL <http://xlink.rsc.org/?DOI=b513480c>.
- Benjamin J. Murray, Daniel A. Knopf, and Allan K. Bertram. The formation of cubic ice under conditions relevant to earth’s atmosphere. *Nature*, 434(7030): 202–205, March 2005. ISSN 0028-0836, 1476-4679. doi: 10.1038/nature03403. URL <http://www.nature.com/doifinder/10.1038/nature03403>.
- Éamonn D. Murray and Giulia Galli. Dispersion interactions and vibrational effects in ice as a function of pressure: A first principles study. *Physical Review Letters*, 108(10):105502, March 2012. doi: 10.1103/PhysRevLett.108.105502. URL <http://link.aps.org/doi/10.1103/PhysRevLett.108.105502>.
- Hiroki Nada and Jan P. J. M. van der Eerden. An intermolecular potential model for the simulation of ice and water near the melting point: A six-site model of H₂O. *The Journal of Chemical Physics*, 118(16):7401, 2003. ISSN 00219606. doi: 10.1063/1.1562610. URL <http://link.aip.org/link/JCPSA6/v118/i16/p7401/s1&Agg=doi>.

- Miloslav Nic. van der waals forces. In Jiří Jiráť, Bedřich Kořata, Aubrey Jenkins, and Alan McNaught, editors, *IUPAC Compendium of Chemical Terminology*. IUPAC, Research Triangle Park, NC, 2.1.0 edition, 1994. ISBN 0-9678550-9-8. URL <http://goldbook.iupac.org/V06597.html>.
- C.G. Ning, B. Hajgat6, Y.R. Huang, S.F. Zhang, K. Liu, Z.H. Luo, S. Knippenberg, J.K. Deng, and M.S. Deleuze. High resolution electron momentum spectroscopy of the valence orbitals of water. *Chemical Physics*, 343(1):19–30, January 2008. ISSN 03010104. doi: 10.1016/j.chemphys.2007.09.030. URL <http://linkinghub.elsevier.com/retrieve/pii/S0301010407004259>.
- Charles E. Ophardt. Hydrogen bonding, 2003. URL <http://www.elmhurst.edu/~chm/vchembook/161Ahydrogenbond.html>. Charles E. Ophardt, PhD, Professor of Chemistry, Chemistry Department, Elmhurst College, Elmhurst, IL, USA.
- Ding Pan, Li-Min Liu, Gareth Tribello, Ben Slater, Angelos Michaelides, and Enge Wang. Surface energy and surface proton order of ice ih. *Physical Review Letters*, 101(15), October 2008. ISSN 0031-9007, 1079-7114. doi: 10.1103/PhysRevLett.101.155703. URL <http://link.aps.org/doi/10.1103/PhysRevLett.101.155703>.
- Ding Pan, Li-Min Liu, Gareth A Tribello, Ben Slater, Angelos Michaelides, and Enge Wang. Surface energy and surface proton order of the ice ih basal and prism surfaces. *Journal of Physics: Condensed Matter*, 22(7):074209, February 2010. ISSN 0953-8984, 1361-648X. doi: 10.1088/0953-8984/22/7/074209. URL <http://iopscience.iop.org/0953-8984/22/7/074209>.
- Linus Pauling. The structure and entropy of ice and of other crystals with some randomness of atomic arrangement. *Journal of the American Chemical Society*, 57(12):2680–2684, December 1935. ISSN 0002-7863. doi: 10.1021/ja01315a102. URL <http://dx.doi.org/10.1021/ja01315a102>.
- John P. Perdew, Kieron Burke, and Matthias Ernzerhof. Generalized gradient approximation made simple. *Physical Review Letters*, 77(18):3865–3868, October 1996. ISSN 0031-9007, 1079-7114. doi: 10.1103/PhysRevLett.77.3865. URL <http://link.aps.org/doi/10.1103/PhysRevLett.77.3865>.
- Victor Petrenko. *Physics of ice*. Oxford University Press, Oxford, 1999. ISBN 9780198518952.
- Cesare Pisani, Silvia Casassa, and Piero Ugliengo. Proton-ordered ice structures at zero pressure. a quantum-mechanical investigation. *Chemical Physics Letters*, 253(3-4):201–208, May 1996. ISSN 00092614. doi: 10.1016/0009-2614(96)00228-X. URL <http://linkinghub.elsevier.com/retrieve/pii/000926149600228X>.
- A. Polian and M. Grimsditch. New high-pressure phase of h₂O: Ice x. *Physical Review Letters*, 52(15):1312–1314, April 1984. doi: 10.1103/PhysRevLett.52.1312. URL <http://link.aps.org/doi/10.1103/PhysRevLett.52.1312>.
- G. Profeta and S. Scandolo. Far-infrared spectrum of ice ih: A first-principles study. *Physical Review B*, 84(2), July 2011. ISSN 1098-0121, 1550-235X. doi:

- 10.1103/PhysRevB.84.024103. URL <http://link.aps.org/doi/10.1103/PhysRevB.84.024103>.
- Ph. Pruzan, J. C. Chervin, and B. Canny. Stability domain of the ice VIII proton-ordered phase at very high pressure and low temperature. *The Journal of Chemical Physics*, 99(12):9842, 1993. ISSN 00219606. doi: 10.1063/1.465467. URL <http://link.aip.org/link/JCPSA6/v99/i12/p9842/s1&Agg=doi>.
- Zamaan Raza, Dario Alfè, Christoph G. Salzmann, Jiří Klimeš, Angelos Michaelides, and Ben Slater. Proton ordering in cubic ice and hexagonal ice; a potential new ice phase—XIc. *Physical Chemistry Chemical Physics*, 13(44):19788, 2011. ISSN 1463-9076, 1463-9084. doi: 10.1039/c1cp22506e. URL <http://xlink.rsc.org/?DOI=c1cp22506e>.
- Xinguo Ren, Patrick Rinke, Gustavo E. Scuseria, and Matthias Scheffler. Renormalized second-order perturbation theory for the electron correlation energy: Concept, implementation, and benchmarks. *Physical Review B*, 88(3), July 2013. ISSN 1098-0121, 1550-235X. doi: 10.1103/PhysRevB.88.035120. URL <http://link.aps.org/doi/10.1103/PhysRevB.88.035120>.
- Steven W. Rick. Simulations of proton order and disorder in ice Ih. *The Journal of Chemical Physics*, 122(9):094504, 2005. ISSN 00219606. doi: 10.1063/1.1853351. URL <http://link.aip.org/link/JCPSA6/v122/i9/p094504/s1&Agg=doi>.
- K. Röttger, A. Endriss, Jörg Ihringer, S. Doyle, and W. F. Kuhs. Lattice constants and thermal expansion of H₂O and D₂O ice Ih between 10 and 265K. addendum. *Acta Crystallographica Section B Structural Science*, 68(1):91–91, January 2012. ISSN 0108-7681. doi: 10.1107/S0108768111046908.
- C. G. Salzmann. The preparation and structures of hydrogen ordered phases of ice. *Science*, 311(5768):1758–1761, March 2006. ISSN 0036-8075. doi: 10.1126/science.1123896. URL <http://www.sciencemag.org/cgi/doi/10.1126/science.1123896>.
- Christoph Salzmann, Paolo Radaelli, Erwin Mayer, and John Finney. Ice XV: a new thermodynamically stable phase of ice. *Physical Review Letters*, 103(10), September 2009. ISSN 0031-9007. doi: 10.1103/PhysRevLett.103.105701. URL <http://link.aps.org/doi/10.1103/PhysRevLett.103.105701>.
- Christoph G. Salzmann, Andreas Hallbrucker, John L. Finney, and Erwin Mayer. Raman spectroscopic study of hydrogen ordered ice XIII and of its reversible phase transition to disordered ice V. *Physical Chemistry Chemical Physics*, 8(26):3088, 2006. ISSN 1463-9076, 1463-9084. doi: 10.1039/b604360g. URL <http://xlink.rsc.org/?DOI=b604360g>.
- Biswajit Santra. E-mail correspondence 'Ice', April 2011.
- Biswajit Santra, Jiří Klimeš, Dario Alfè, Alexandre Tkatchenko, Ben Slater, Angelos Michaelides, Roberto Car, and Matthias Scheffler. Hydrogen bonds and van der Waals forces in ice at ambient and high pressures. *Physical Review Letters*, 107(18):185701, October 2011. doi: 10.1103/PhysRevLett.107.185701. URL <http://link.aps.org/doi/10.1103/PhysRevLett.107.185701>.

- Biswajit Santra, Jiří Klimeš, Alexandre Tkatchenko, Dario Alfè, Ben Slater, Angelos Michaelides, Roberto Car, and Matthias Scheffler. On the accuracy of van der waals inclusive density-functional theory exchange-correlation functionals for ice at ambient and high pressures. July 2013. URL <http://arxiv-web3.library.cornell.edu/abs/1307.3339>.
- Maddury Somayazulu, Jinfu Shu, Chang-sheng Zha, Alexander F Goncharov, Oliver Tschauner, Ho-kwang Mao, and Russell J Hemley. In situ high-pressure x-ray diffraction study of H₂O ice VII. *The Journal of Chemical Physics*, 128(6): 064510–064510–10, February 2008. ISSN 00219606. doi: doi:10.1063/1.2813890. URL http://jcp.aip.org/resource/1/jcpsa6/v128/i6/p064510_s1.
- R. Sternheimer. Effect of the atomic core on the nuclear quadrupole coupling. *Physical Review*, 95(3):736–750, August 1954. ISSN 0031-899X, 1536-6065. doi: 10.1103/PhysRev.95.736. URL <http://link.aps.org/doi/10.1103/PhysRev.95.736>.
- R. Sternheimer and H. Foley. Nuclear quadrupole coupling in the li₂ molecule. *Physical Review*, 92(6):1460–1468, December 1953. ISSN 0031-899X, 1536-6065. doi: 10.1103/PhysRev.92.1460. URL <http://link.aps.org/doi/10.1103/PhysRev.92.1460>.
- E. Sugimura, T. Komabayashi, K. Hirose, N. Sata, Y. Ohishi, and L. S. Dubrovinsky. Simultaneous high-pressure and -temperature volume measurements of H₂O ice and the phase transition of ice VII. *AGU Fall Meeting Abstracts*, 21: 1219, December 2009. URL <http://adsabs.harvard.edu/abs/2009AGUFM.P21B1219S>.
- J. M Thijssen. *Computational physics*. Cambridge University Press, Cambridge, UK; New York, 1999. ISBN 0521833469 9780521833462 0521541069 9780521541060.
- Paul Robert Tulip. Dielectric and lattice dynamical properties of molecular crystals via density functional perturbation theory: Implementation within a first principles code, 2004. URL http://cmt.dur.ac.uk/sjc/thesis_prt/node39.html.
- Carlos Vega, Carl McBride, Eduardo Sanz, and Jose L. F. Abascal. Radial distribution functions and densities for the SPC/E, TIP4P and TIP5P models for liquid water and ices ih, ic, II, III, IV, v, VI, VII, VIII, IX, XI and XII. *Physical Chemistry Chemical Physics*, 7(7):1450, 2005. ISSN 1463-9076. doi: 10.1039/b418934e. URL <http://xlink.rsc.org/?DOI=b418934e>.
- Stephen G. Warren. Optical constants of ice from the ultraviolet to the microwave. *Applied Optics*, 23(8):1206, April 1984. ISSN 0003-6935, 1539-4522. doi: 10.1364/AO.23.001206. URL <http://www.opticsinfobase.org/abstract.cfm?URI=ao-23-8-1206>.
- E. Whalley. Energies of the phases of ice at zero temperature and pressure. *The Journal of Chemical Physics*, 81(9):4087–4092, November 1984. ISSN 00219606. doi: doi:10.1063/1.448153. URL http://jcp.aip.org/resource/1/jcpsa6/v81/i9/p4087_s1.

- E. Whalley, J. B. R Heath, and D. W Davidson. Ice IX: an antiferroelectric phase related to ice III. *The Journal of Chemical Physics*, 48(5):2362–2370, March 1968. ISSN 00219606. doi: doi:10.1063/1.1669438. URL http://jcp.aip.org/resource/1/jcpsa6/v48/i5/p2362_s1.
- Wikipedia. Intermolecular force, May 2013a. URL http://en.wikipedia.org/w/index.php?title=Intermolecular_force&oldid=557706438. Page Version ID: 557706438.
- Wikipedia. London dispersion force, May 2013b. URL http://en.wikipedia.org/w/index.php?title=London_dispersion_force&oldid=557110207. Page Version ID: 557110207.
- Wikipedia. Van der waals force, June 2013c. URL http://en.wikipedia.org/w/index.php?title=Van_der_Waals_force&oldid=548516565. Page Version ID: 548516565.
- O. Yamamuro, M. Oguni, T. Matsuo, and H. Suga. Heat capacity and glass transition of pure and doped cubic ices†. *Journal of Physics and Chemistry of Solids*, 48(10):935–942, January 1987. ISSN 00223697. doi: 10.1016/0022-3697(87)90130-2. URL <http://linkinghub.elsevier.com/retrieve/pii/0022369787901302>.
- Yukihiro Yoshimura, Sarah T Stewart, Maddury Somayazulu, Ho-kwang Mao, and Russell J Hemley. High-pressure x-ray diffraction and raman spectroscopy of ice VIII. *The Journal of Chemical Physics*, 124(2):024502–024502–7, January 2006. ISSN 00219606. doi: doi:10.1063/1.2140277. URL http://jcp.aip.org/resource/1/jcpsa6/v124/i2/p024502_s1.

Abstract

An accurate calculation of energy differences and lattice constants of water ice phases with *ab initio* methods is difficult, most notably the description of the hydrogen bonds is a major challenge to the theory.

In the hydrogen bond, static, classical dipole-dipole interactions, as well as dynamic dipole-dipole interactions, so-called van der Waals (vdW) interactions, play a major role. Classical density functional theory (DFT) such as the Perdew-Burke-Ernzerhof (PBE) functional overestimates the bond strength at low densities and underestimates the bond strength at high densities. It follows that neither energy differences nor lattice constants are very accurate. Taking into account corrections to the van der Waals forces in density functional theory results in a better description of the energy differences between the various phases, however, the equilibrium volumes are now generally much too small. This indicates that the Pauli repulsion is somewhat underestimated in density functional theory.

Right now only Diffusion Monte Carlo and Moeller-Plesset perturbation theory yield an accurate description for all phases. We seek a theory that is comparatively cheap and in the future also applicable to water on surfaces, an area that is currently extensively explored in theory and experiments.

One possible choice for the correlation energy is the random phase approximation (RPA), which has a very reasonable balance between computational cost and accuracy. We want to see whether it yields a good description of low and high density structures using this unified approach.

Using the Vienna Ab initio Simulation Package (VASP), ground state energies and volumes for various water ice phases have been calculated using DFT-PBE as well as RPA. The RPA correlation energy was combined with both, the exact-exchange energy from DFT orbitals and an exchange energy from self-consistent HF calculations. Bulk moduli and their first pressure derivatives have been calculated using a 3rd order Birch-Murnaghan equation of state.

We find that RPA yields reasonable results regarding energy and lattice parameters over the entire pressure range. Although PBE performs reasonably well at low-pressure phases, it underestimates binding energies already at mid-pressure phases due to missing vdW interactions. PBE volumes are underestimated at medium and high pressures.

Finally, infrared intensities for the cubic and hexagonal phases were obtained from linear response theory.

Zusammenfassung

Die genaue Berechnung der Energiedifferenz und der Gitterkonstanten von verschiedenen Eisphasen ist mit *ab initio* Methoden schwierig, wobei vor allem die Beschreibung der Wasserstoffbrückenbindungen eine große Herausforderung an die Theorie darstellt.

In der Wasserstoffbrücke spielen sowohl elektrostatische, klassische Dipol-Dipol Wechselwirkungen, als auch dynamische Dipol-Dipol Wechselwirkungen, sogenannten Van-der-Waals (VdW) Wechselwirkungen, eine große Rolle. Klassische Dichtefunktionaltheorie (DFT), wie zum Beispiel das Perdew-Burke-Ernzerhof (PBE) Funktional, überschätzt die Bindungsstärke bei kleinen Dichten und unterschätzt die Bindungsstärke bei großen Dichten. Das führt dazu, dass weder Energiedifferenzen noch Gitterkonstanten besonders genau sind. Wenn man Korrekturen für die Van-der-Waals-Kräfte in der Dichtefunktionaltheorie berücksichtigt, erzielt man eine bessere Beschreibung der Energiedifferenzen zwischen den einzelnen Phasen, allerdings sind die Gleichgewichts-Volumina nun allgemein deutlich zu klein. Dies weist darauf hin, dass die Pauli-Abstoßung in der Dichtefunktionaltheorie etwas unterschätzt wird.

Eine hochgenaue Beschreibungen für alle Phasen liefern derzeit nur Quanten-Monte-Carlo-Methoden (*Diffusion Monte Carlo*, DMC) und die aus der Quantenchemie bekannte *Moeller-Plesset-Störungstheorie* (MP2). Beide sind allerdings mit erheblichem Rechenaufwand verbunden oder für Festkörper im Moment nicht praktikabel (MP2). Wir suchen eine Methode, die vergleichsweise "billig" und in Zukunft auch für Wasser auf Oberflächen anwendbar ist - ein Bereich, der derzeit theoretisch und in Experimenten ausführlich untersucht wird.

Eine mögliche Wahl ist die *random phase approximation* (RPA) für die Korrelationsenergie, die eine vernünftige Balance zwischen Rechenaufwand und Genauigkeit ermöglicht. In dieser Arbeit wird untersucht, ob damit eine gute Beschreibung von Eisstrukturen im Nieder- und Hochdruckbereich möglich ist.

Unter Zuhilfenahme des *ab initio* Pakets *Vienna Ab initio Simulation Package* (VASP) wurden Grundzustandsenergien und -volumina für verschiedene Wasser-Eis-Phasen berechnet, wobei DFT-PBE sowie RPA verwendet wurden. Die RPA-Wechselwirkungsenergie wurde dabei sowohl mit der selbstkonsistent berechneten als auch mit der nicht-selbstkonsistenten Hartree-Fock-Austauschenergie der DFT-Orbitale kombiniert. Das Kompressionsmodul sowie die erste Ableitung nach dem Druck wurden mit Hilfe einer Birch-Murnaghan-Zustandsgleichung dritter Ordnung berechnet.

Wir zeigen, dass RPA vernünftige Resultate bezüglich Energie und Gitterkonstante sowohl bei niedrigen Drücken als auch bei Hochdruck-Phasen liefert. Obwohl PBE bei niedrigen Drücken relativ gute Ergebnisse liefert, unterschätzt es die Bindungsenergien bereits im mittleren Druckbereich wegen der fehlenden

Van-der-Waals-Wechselwirkungen. Die Volumen werden bei PBE-Berechnungen bei mittleren und hohen Drücken unterschätzt.

Weiters wurden die Infrarot-Intensitäten der kubischen und hexagonalen Phasen studiert.

Acknowledgements

I would like to thank Cesare Franchini as well as my supervisor Georg Kresse for ideas and suggestions for my work, the patiently answering of my questions and the detailed proofreading. I also thank Michael Pörtl for the trouble-free execution of the computer simulations.

Curriculum vitae

Markus Macher

Education

2011–(2013)	Master Studies in Physics at the University of Vienna
January 2011	Graduation with distinction, awarding the academic degree BSc.
2007–2011	Studies in Physics at the University of Vienna
1994–1999	Higher Branch for Technical Informatics, Federal Higher Technical Institute for Educating and Experimenting, Mödling, Austria

Employment

2001–2007	System Operator at Inode GmbH
2000–2001	Software Engineer at Bosch GmbH